Behaviour of two-way spanning walls subjected to out-of-plane loading by numerical analysis

Mohit Soni

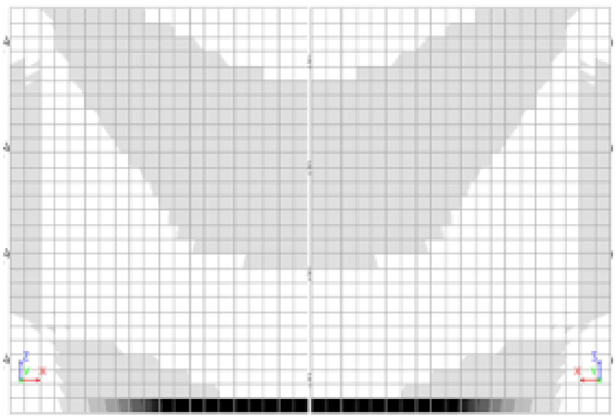

Four sides restrained wall

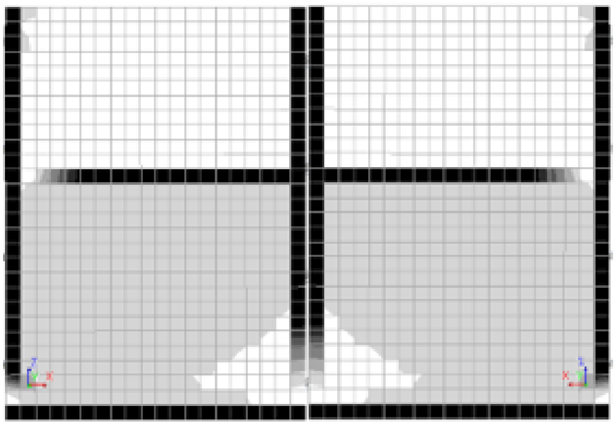

Three sides restrained wall

TU Delft

Behaviour of two-way spanning walls subjected to out-of-plane loading by numerical analysis

by

Mohit Soni

to obtain the degree of Master of Science
at the Delft University of Technology,
to be defended publicly on Thursday December 19, 2019 at 04:30 PM.

Student number:	4748026	
Project duration:	March, 2019 - December, 2019	
Thesis committee:	Prof. dr. ir. J. G. (Jan) Rots,	TU Delft
	Dr. R. (Rita) Esposito,	TU Delft
	Dr. ir. K. N. (Karel) van Dalen,	TU Delft
	Dr. ir. G. J. P. (Geert) Ravenshorst,	TU Delft

An electronic version of this thesis is available at `http://repository.tudelft.nl/`.

Summary

Unreinforced masonry (URM) buildings are vulnerable when subjected to out-of-plane dynamic loading, especially under as earthquakes. Within the masonry building, the wall spanning in the direction perpendicular to the seismic loading is the most critical component. Damage to these walls (out-of-plane failure) frequently leads to the partial or global collapse in the URM building structures, especially if the wall is a load-bearing wall. Boundary conditions and overburden load drastically influence the response of out-of-plane loaded walls. Two-way spanning walls that are restrained on three or four sides show a larger force capacity compares to one-way spanning walls, which are only restrained at top and bottom. Nevertheless, the studies on the behavior of two-way spanning walls are limited.

This thesis aims to understand the two-way bending behavior of unreinforced masonry walls subjected to out-of-plane loading employing numerical analysis. A three-dimensional model using a shell element is adopted. Cracking is modeled with a continuum damage approach by comparing the isotropic model, namely the rotating smeared cracking approach (TSRC), and an orthotropic model, namely the engineering masonry model (EMM). The effect of the top boundary condition on the response of the two-way spanning walls is examined by considering case studies: four sides restrained wall with overburden load, and three sides restrained wall without overburden load. Both the walls are vertically connected with the pier (or return wall) with an alternate row of headers providing full moment restraint. The description concerning the seismic behavior of the two-way spanning wall made based upon the analysis carried out incorporating different loadings types like the uniform, mode proportional loading, time history, and cyclic loading.

The orthotropic material model is better in evaluating the response of the two-way spanning wall as compared to the isotropic material model if the proper support condition is specified. The difference in response using either material model is visible at the onset of cracking. The response of the two-way spanning wall under monotonic increasing load using EMM demonstrates walls have a displacement capacity to sustaining a relatively constant load, whereas the TSRC fails to capture this behavior. Due to high non-linearity because of cracking in the elements, the solution becomes non-convergent, and a solid statement regarding the ultimate displacement capacity of the wall can not be made. However, based on the results from static analysis using EMM, a two-way spanning wall have sufficient displacement capacity well over the wall thickness. The displacement capacity signifies the wall can deform in the out-of-plane direction without failure and is beneficial, especially during an earthquake event.

In two-way spanning walls, both the peak load and initial stiffness of the walls is enhanced by higher pre-compression and top lateral support (Figure 1). It is found both experimentally and numerically, as pre-compression increases flexural and shear resistance capacity of the wall to resist the out-of-plane load. Furthermore, in the wall restrained on three sides, the crack pattern is initiated at the main-wall and pier connection, representing the head-joint cracking, leading to changing the behavior from two-way to one-way. While in the wall restrained on four sides, the cracking is initiated at the top and bottom support, therefore the wall can sustain the load both via horizontal bending along the vertical edge. Furthermore, the influence of top rotation fixity on the crack pattern in four sides restrained wall demonstrates the change in crack pattern without significant difference in the force-displacement plot. Therefore, it is vital to know the proper boundary condition in the wall to help in identifying the weakest link and suggest the necessary strengthening location.

To predict the dynamic behavior of the two-way spanning wall by alternative load application is studies using static, non-linear time history, and cyclic analysis. The analysis of the wall with uniform monotonic increasing load fails to capture the post-crack behavior. Whereas, under the application of mode-proportional loading and using the material properties as stated in the case study, the initial stiffness and peak load is significantly lower, because of the applied load pattern (Figure 1). Therefore, the material properties are calibrated to match the initial stiffness and peak load but fail to provide information regarding peak load and ultimate displacement capacity. Using the original material properties, the outcome of the non-linear time history (NLTH) gives reasonable prediction in response up to the pre-crack run as compared to the case study. The four sides restrained wall shows very stiff response with very few cracks initiations to dissipate energy in

the wall while rapid degradation in the three sides restrained wall is found, which attributed to the brittle response with wall top reaching the larger out-of-plane displacement. Due to non-linearity (follows from cracking), irrespective of the material model, the outcomes of NLTH analysis fails to capture the crack and post-crack behavior. Therefore, the material model needs improvement in tension and cohesion softening to better account for non-linearity in the time-history analysis. Due to the limitation of the NLTH analysis, cyclic analysis with increasing magnitude of load cycles was carried out to replicate the dynamic response. The outcomes give a fair indication of material degradation (based on energy dissipation) and crack formation but fail to capture the displacement capacity. Furthermore, the contribution of mode-II fracture energy in the overall energy degradation is significant for three sides restrained wall but not in four sides restrained wall. Due to top support, and increased shear strength capacity of the wall due to pre-compression load. Analyzing the two-way spanning wall under different loading shows the asymmetric response in the positive (toward pier) and negative (away from pier) displacement directions (with a 36% difference in force capacity). This asymmetry is arisen due to the presence of the return wall at the vertical junction.

Finally, the combination of static (with uniform load) and cyclic analysis provides a reliable indication of wall force degradation of the two-way spanning wall. It can be used as a substitute for NLTH analysis. However, no solid statement regarding displacement capacity can be made based on the non-convergence in the numerical analysis. Furthermore, the crack pattern observes under different loading shows the damage is primarily influenced by boundary conditions rather than the type of loading. Based on the outcome of the thesis work, further studies are needed to improve the convergent behavior of the numerical analyses to gain information on the displacement capacity of two-way spanning walls subject to out-of-plane loading. Additionally, it becomes interesting to explore the use of micro-modeling to understand the crack propagation in the masonry wall, and to exploring different anisotropic model such as the Rankine-Hill model, or to explore the implementation of strain rate dependent constitutive model (mainly used for impact loading) to understand the dynamic behavior in NLTH analysis.

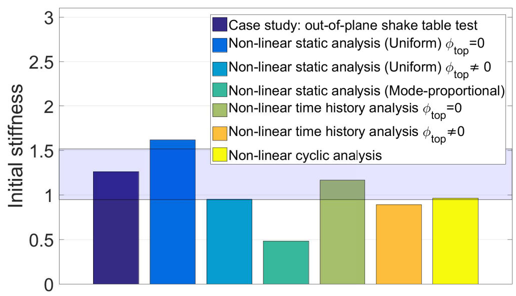

(a) Four sides restrained wall: Initial stiffness.

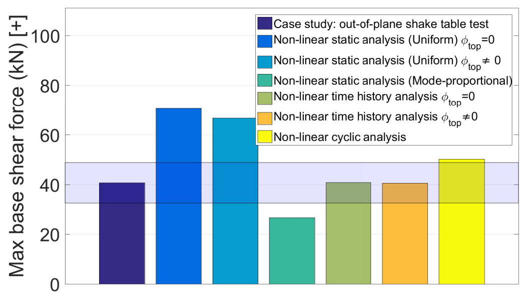

(b) Four sides restrained wall: Maximum base shear force.

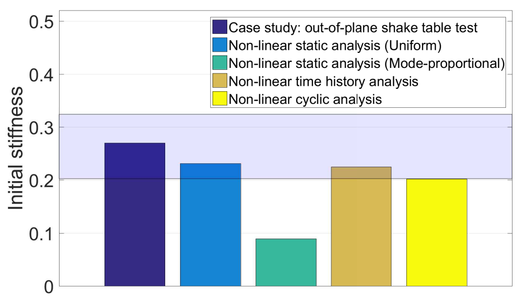

(c) Three sides restrained wall: Initial stiffness.

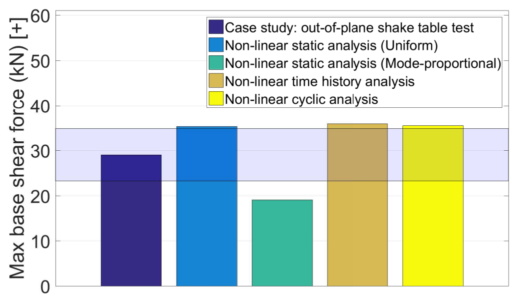

(d) Three sides restrained wall: Maximum base shear force.

Figure 1: Response of two-way spanning wall under different loading in terms of initial stiffness and maximum base shear force using orthotropic material model. Band of 20% difference to that of experiment.

"To Maa, and Papa"

Contents

List of Figures

List of Tables

1

Introduction

1.1. Background of study

The province of Groningen is the 7th largest province of the Netherlands, covering $2,968 km^2$ of area. The capital city Groningen is traditionally the oldest and biggest city around which the province has been named after. The history of the region has been traced back when the Roman camp was established in the region around 48 CE. Thirteenth to the Fifteenth century endured the most influential period of the region, most notably being the administration work of the province of Friesland was administered by Groningen. Moreover, it became an important trade centre and construction of tallest steeple structure of Europe; the Martini tower (Figure 1.1) completed [**?** **?**]. In 1959, the natural gas field was discovered near Slochteren, shown in Figure 1.2. For 60 years, more than 1700 billion cubic meters of natural gas has been extracted.

Figure 1.1: Groningen market square Province of Groningen.
Source: **?**]

Figure 1.2: Testing the Groningen discovered well, Slochteren 1, 1959
Source: **?**]

The natural-gas extraction began in 1963 by the Nederlandse Aardolie Maatschappij BV (NAM), a joint venture between Royal Dutch Shell and ExxonMobil. The extraction of fossil fuel over the years has promoted the ground settlement. These phenomena have developed a zone of differential settlement in the neighboring soil bed. These caused gradual accumulations of elastic stresses under the ground, similar to the stretching of a rubber band. When the accumulated stresses reach the limit rubber-band, break. In the same way, stored energy in the soil is released, which travels in the form of vibration that causes shaking at the ground surface. In geology, this phenomenon is termed as elastic rebound theory was first proposed by Henry Fielding Reid based on his observation of the displaced ground surface after the 1906 San Francisco earthquake [**?**]

The earthquake in Groningen province comes under the category of a shallow sub-surface earthquake (depth ≤ 70km). The average hypocenter is typically measured at a depth of 3km based on the hypocenter location identification of p-wave arrivals reported by the Royal Netherlands Meteorological Institute (KNMI) in Groningen [?]. The first notable incident of the earthquake was reported in 1991, with a magnitude of ≤ 2.5. After 1991, both frequencies of occurrence and magnitude of earthquakes have increased appreciably. Figure 1.3 shows the history of earthquake incidence data as reported by the NAM feiten en cijfers data website [?]. In the years 2006 and 2012, the magnitude of the earthquake recorded on the Richter scale exceeded the 3.5 level mark. With a unit increase in level mark i.e., from levels 2 to 3, the wave amplitude generated becomes ten times, causing an increase in the ground shaking, which leads to an increase in lateral load on the masonry building.

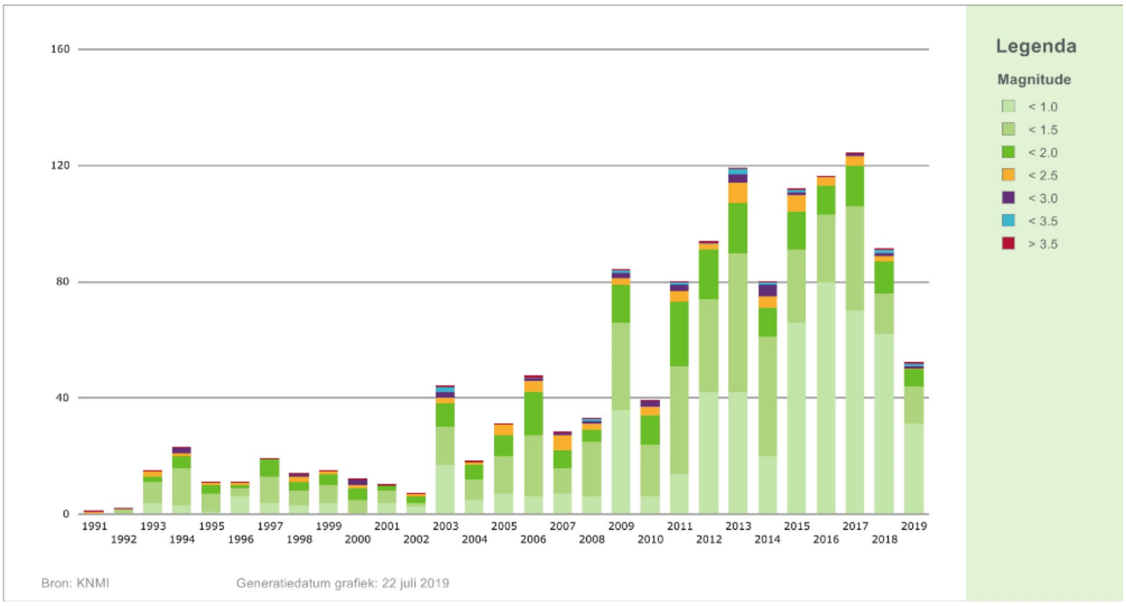

Figure 1.3: Number of earthquake in the Groningen gas field between the year 1991-2019.
Source: ?]

1.2. Research Objective

During an event of an earthquake wall within the masonry building, experiences load in different directions depending on the wall orientation. The loads are mainly classified into in-plane, and out-of-plane load, and the damage or failure associated with each are known as in-plane or out-of-plane damage or failure. Among these, out-of-plane damages in the masonry wall are first failure mode that should be prevented as it would lead to global or partial failure of the building, as observed in the past earthquakes [? ? ?], especially if the wall is a load-bearing wall. The out-of-plane walls are further classified into one-way spanning, and two-way spanning (with rigid/flexible diaphragms) walls based on support condition. In the past decades (between 1960-2010), significant studies were performed to understand the one-way bending capacity of the unreinforced masonry wall structures both under static and dynamic loading [? ?].

The seismic resistance capacity (mainly displacement capacity) of a two-way spanning wall is higher than the one-way spanning due to lateral confinement of the masonry walls. The confinement elements consist of roof/floor and the vertical wall connection that helps in preventing the brittle response and protect the wall from complete failure during major earthquakes [?]. Because of the higher capacity of a two-way spanning wall, research is limited to the quasi-static loading on a full-scale model using the air-bag tests [? ?]. Hence the two-way bending failure under dynamic loading is not fully understood and is often a discussion topic among the scientific community. Considering the above points, the objective of the thesis work is to be on the ***numerical modeling approach to understand the two-way bending behavior of the unreinforced masonry wall subjected to out-of-plane loading***.

The outcomes of the finite element analysis are calibrated with the experimental results of the full-scale specimens tested on the shake table at EUCENTRE [?]. The comparison between numerical and experimental results have been made in terms of load-vs-deflection curves, crack pattern, and the energy dissipation study.

1.2.1. *Research questions*
In order to accomplish the research objectives, the main research question of the research work is **how to predict seismic behavior of two -way spanning wall based on the application of different out-of-plane loadings?**. The main research question is further sub-divided into the sub-research questions as follows:

- To what extent the orthotropic and isotropic material models are capable of predicting the out-of-plane response of the unreinforced masonry wall (URM)?
- How the out-of-plane wall response varies with different top boundary conditions using shell element in the numerical analysis?
- Based on the application of the different types of loading, can the seismic behavior of URM walls be identified?

For the experimental benchmark, *"Experimental response of URM single leaf and cavity walls in out-of-plane two-way bending generated by seismic excitation"* by **?**] is chosen to validate the numerical results.

1.2.2. *Research method*
In order to answer the research questions the following approach is setup.

- *Understand the working principle behind the two different constitutive models by static & cyclic analysis and non-linear time history.*
  - Comparison between the engineering masonry model (EMM) and the total strain crack model (TSCM) should be carried out.
- The sensitivity to material parameters in the numerical response to calibrate with experimental outcomes.
  - The Input parameter should be changed to get the hysteretic behavior and crack pattern close to the experimental results.
- The influence of the boundary condition on the failure mechanisms under different loading conditions.
  - Changing the top boundary conditions in the specimen and validating the failure mechanism with the experimental results.

1.3. Report Overview
The report is divided into six chapters, chapter-2 contains the literature study, which is classified into two parts. Part-1 describes the fundamental of the masonry structures, and part-2 report the details of the modeling strategies available in the numerical analysis. The details of the experimental campaign on the unreinforced masonry wall subjected to out-of-plane dynamic loading are provided in chapter-3. These include specimen geometry, setup, loading, and results for different specimen configurations. Chapter-4 contains the details of the finite element modeling for masonry walls. The outcomes of the numerical analysis for different loadings are provided in chapter-5. Discussion of the results based on material models, boundary conditions and loading types, the conclusions of the thesis work are drawn, and future recommendations are given in the chapter-6. The global overview of the report is shown in Figure 1.4 with a link between the chapters.

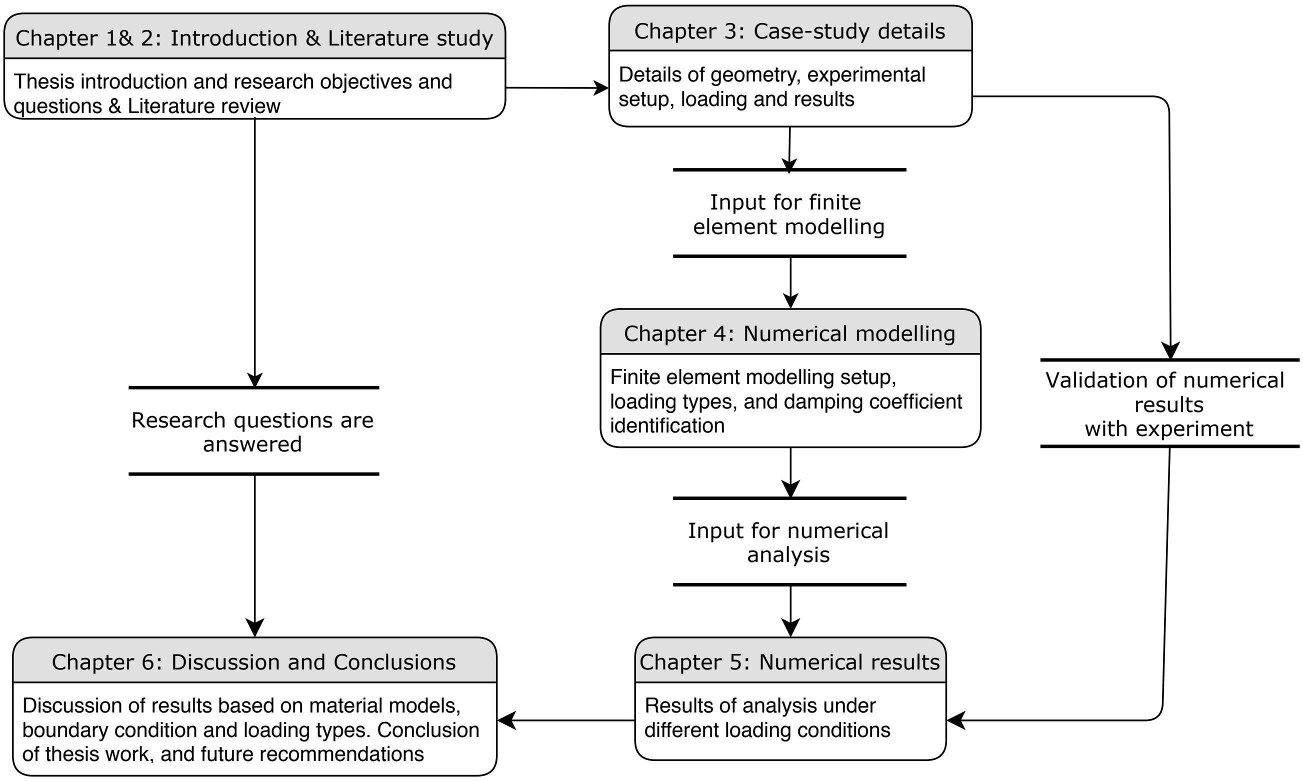

Figure 1.4: Structure of report

2

Literature Study

The complexity involves the out-of-plane behavior of unreinforced masonry (URM), especially during dynamic loading, makes it a popular discussion topic among the researchers. The URM wall response under out-of-plane dynamic loading significantly depends on the material variability and boundary conditions. The goal of this chapter is to provide detailed information on the studies done till now to understand the out-of-plane response URM walls. The following chapter is divided into two parts. The first part provides the fundamentals of the behavior of masonry structure. In this, the global response of URM walls subjected to in-plane and out-of-plane loading, experimental classification of out-of-plane wall subjected to different loading is detailed. Then material characterization of the masonry is presented. In the second part, the different numerical modeling strategies available in the literature for modeling continuous system into an equivalent model are described. Finally, the seismic analysis method to describe the dynamic behavior is reported.

2.1. Fundamentals of unreinforced masonry structures

Masonry is a universal term used for a structure constructed using block, which is joined together using mortar. Depending upon the availability of the materials locally, the block can be made up of stone, mud, brick, etc. The block is joint together using the mud or with cement mortar. When subjected to an external load, each component experience different load that is resisted by both brick and mortar together. Masonry structures are constructed for carrying the gravity load while they are weak in sustaining the lateral load, especially during an event of an earthquake. This insufficiency leads to the global or local failure in the wall that modifies the path of gravity load in the structure hence decrease the service life of the structure.

During the event of an earthquake, the URM building wall inevitably experiences a combination of in-plane and out-of-plane load. Because of different in-plane and out-of-plane stiffness of the wall, a different proportion of load is resisted by each component. The combined action of in-plane and out-of-plane resisting behavior in the URM building is termed as *box-type behavior*, as shown in Figure 2.1. In the box-type behaviour, the connection between the perpendicular walls and the wall-to-floor connection is important in resisting the lateral loads. Improving the wall-to-floor connection is an effective means of tying the wall to one single beam, which will help in improving the box-action behaviour of masonry structure as concluded by **?**]. URM structure without floor ties and weak connection between the perpendicular wall exhibit one-way failure behaviour (Figure 2.1a). Whereas, in two-way failures are shown in Figure 2.1b, and Figure 2.1c for three and four sides restraint wall respectively.

Blind test prediction of the out-of-plane response of the URM wall is carried out in 2017 by 25 researchers to predict the peak ground acceleration at the collapse of clay brick structure, as shown in Figure 2.2a. The $PGA_{average}$ predicted by the group underestimates the capacity of the structure by 2.5 times that of $PGA_{experiment}$, as found from the shake table test (Figure 2.2b). These outcomes concluded the need for improving knowledge of the two-way spanning out-of-plane URM walls.

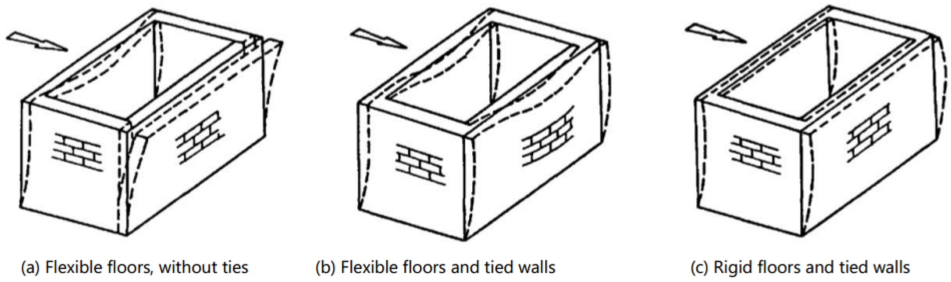

Figure 2.1: Box type behaviour of masonry under seismic excitation.
Source: **? ?**

(a) Specimen setup on the shake table.

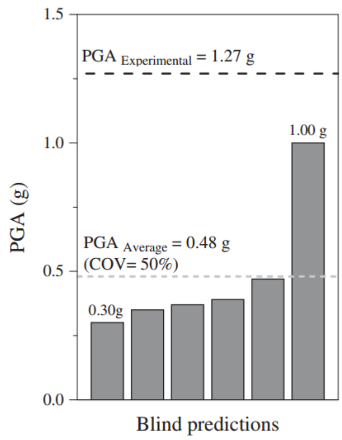

(b) Results of blind prediction

Figure 2.2: The blind prediction for peak ground acceleration at failure of brick structure. (a) Clay brick masonry specimen on the shake table; and (b)comparison of result with the experiment.
Source: **? ?** .

2.1.1. Global response of URM buildings

Global failure in the URM structure primarily depends on the direction of load action, geometry, boundary support conditions, and material properties. Depending on the direction of loading i.e., either along the span of the wall (in-plane loading) or perpendicular to the wall (out-of-plane loading), different internal resisting stresses are activated. The exceedance of these internal stresses to the permissible strength limit of the material likes compressive, tensile, and shear strength causes the partial or complete (global) failure in the masonry structures. Therefore, understanding the failure mechanisms involve due to in-plane and out-of-plane loading is vital to predicting the behavior of URM walls due to dynamic loading.

In-plane failure

The load acting in the span direction of the unreinforced masonry wall causes the *in-plane* failure. The in-plane failure mechanisms are mainly classified into three categorize, like rocking, shear sliding, and the diagonal shear, as shown in Figure 2.3. From the post-earthquake damage assessment study of the Santa Cruz, Loma Prieta, [**?**] shows that failure occurs in span direction of the wall reduces the load-bearing capacity but prevent the complete failure (Figure 2.4a). **? ?** investigated the unreinforced masonry behavior in in-plane cyclic-loading on different wall configurations with varying span and overburden pressure. The outcome of the experiment campaign concluded the significant effect of vertical compression and a shear ratio (α_v) on the in-plane failure of the URM walls. Where the in-plane shear ratio is calculated, as shown in Equation 2.1.

$$\alpha_v = \frac{M}{V \cdot H} = \frac{\text{Moment at the end}}{\text{Shear} \cdot \text{Height of panel}}. \tag{2.1}$$

The walls having a higher shear ratio are more likely to fail in flexure leading to slipping off the wall, i.e., creating horizontal crack along the wall span (Figure 2.4b) also known as *shear sliding failure*. Toe-crushing failure is observed in the walls with a high shear ratio resulting in excessive rotation around the corner leading to

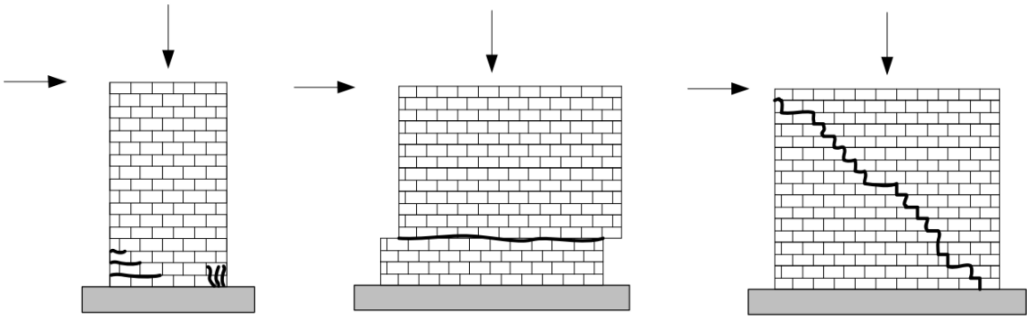

(a) Rocking (b) Shear Sliding (c) Diagonal Shear

Figure 2.3: In-plane load resistance of unreinforced masonry walls
Source: ? ?

rocking failure. Whereas the wall with lower shear ratio fails in shear, and the diagonal crack pattern is visible in the wall (Figure 2.4c). Since the experiment was not last till the ultimate failure of the masonry, therefore based on the experiment outcomes, the URM wall shows high in-plane displacement capacity, which is essential for the seismic evaluation of the structure.

(a) Post earthquake in-plane failure (b) Flexure failure (c) Shear failure

Figure 2.4: In-plane failure of URM. (a) shear failure is observed after Santa Cruz, Loma prieta earthquake ? ? ; In-plane failure of URM with high (b) and low shear(c) ratio ? ? .

Out-of-plane failure

The wall fails in the *out-of-plane* (OOP) direction when the load acting on the URM is in the direction perpendicular to the wall span. Most often, URM walls are not designed to carry any lateral load in the out-of-plane direction, but the wall is required to have sufficient capacity to avoid out-of-plane failure, especially when the wall is load-bearing. According to ? , the in-plane failure of the wall results in the reduction of lateral load-carrying capacity, but the out-of-plane failure of walls results in complete or partial failure in the structure. For seismic evaluation of the masonry structure, displacement-based design capacity has gained importance due to the limitation of the force-based design approach in finding the maximum displacement capacity before failure. In displacement-based design criteria, the failure in the wall occurs when it exceeds the ultimate displacement, not the ultimate force in the wall (?]). Beyond the ultimate load in the masonry wall, the internal resisting moment balances by the destabilizing moments; hence, the wall can deform further without complete failure. For one-way spanning, the wall destabilizes when the displacement reaches the wall thickness. Whereas a two-way spanning wall has an added benefit of support condition and has high displacement capacity reaching up to twice the wall thickness before failure (?]). The support condition of the URM wall has a significant influence on the failure (Crack) patterns. The out-of-plane failure mechanism is broadly divided into two categories based on the support conditions. i.e., one -way spanning and two-way spanning wall.

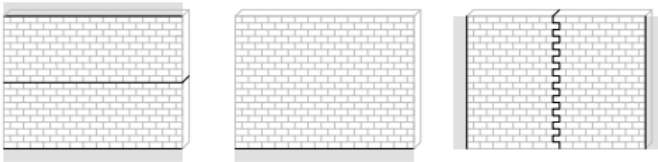

Figure 2.5: Boundary condition in one-way bending mechanism.
Source: ? ?

One way out-of-plane failure

The walls are classified as *one-way spanning* wall when the wall is supported at either two parallel edges or along one edge. One-way spanning wall undergoes uniaxial bending, and the crack pattern runs parallel to the support condition in either horizontal and vertical direction depending on span orientation shown in Figure 2.5. Because of the support conditions, internal resisting stresses are generated either by perpend joint flexure and bed joint torsion resisting horizontally applied moment (Figure 2.5a) or bed-joint flexure resisting vertical bending (Figure 2.6b). The above inference of boundary condition is further validated by the experimental shake table test on one way spanning wall as reported in ? ? and ? ? . Figure 2.7 shows the failure pattern along the horizontal line as observed in the masonry wall at the end of the dynamic test.

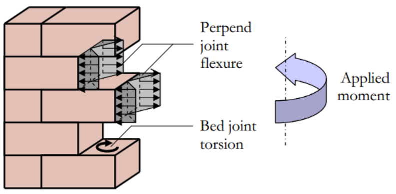

(a) Horizontal bending

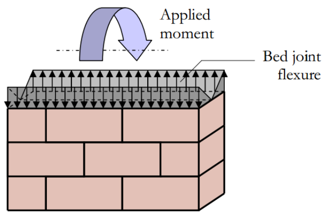

(b) Vertical bending

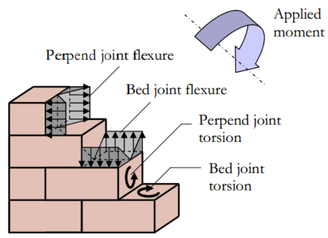

(c) Diagonal bending

Figure 2.6: Resistance component of the masonry when moment applied in different direction . (a) Horizontal bending; (b) Vertical bending; (c) Diagonal bending.
Source: ? ?

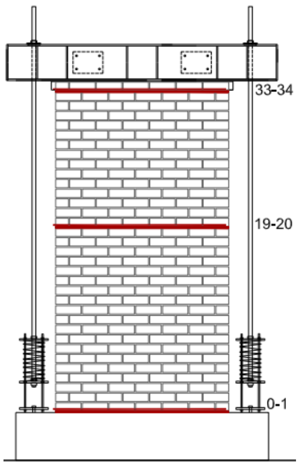

(a) Specimen crack location in one-way bending failure

(b) Snap-shot of specimen failure in one-way bending

Figure 2.7: One-way bending failure of URM subjected to shake table test
Source: ? ?

Two-way out-of-plane failure

Two-way spanning URM is distinguished primarily from one-way when the wall is supported on at least one vertical or one horizontal edge, as shown in Figure 2.8. More often, in the building structure, the main wall is

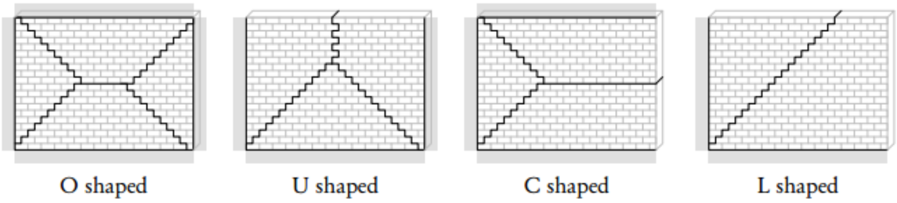

Figure 2.8: Boundary conditions for two-way out-of-plane failure mechanisms.
Source: **? ?**

supported vertically at the edge by the connecting wall called a return wall or pier in literature. In the present report, the word 'pier' will be used for these walls. These connections provide the full moment restraint to the main wall as a result of imposing the fixed support condition. The effect of this vertical restraint on the ultimate load (in out-of-plane) carrying capacity of the URM was reported by **?**]. At the end of the experimental test, the crack pattern along the junction of the main-wall and pier appeared. They are thus changing the behavior of the main wall from two-way to one-way. This cracking at the junction can be further attributed to the high in-plane stiffness of pier as compared to the stiffness in the out-of-plane direction. Figure 2.9a shows the wall set up for the initial push and cyclic test. While in Figure 2.9b shows the crack pattern at the end of the test from inside and outside, respectively.

(a) Photograph of wall setup

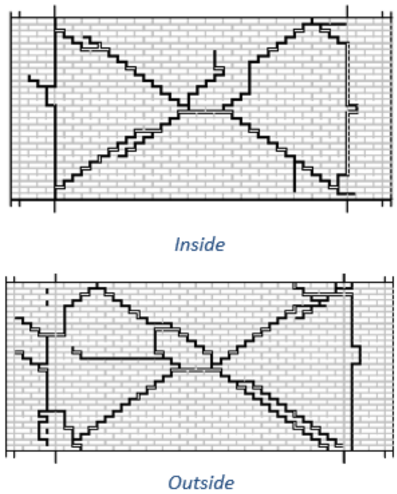

(b) Force-displacement plot.

Figure 2.9: The result of the cyclic test on two-way spanning hollow clay brick wall.
Source: **? ?** .

Furthermore, in the dynamic shake table test on the calcium silicate brick masonry wall with top restrained support with pre-compression load was reported by **?** in **?** . The crack pattern observed in the wall specimen shows the formation of a vertical crack along with the main-wall and pier connection before the collapse of the main wall in the dynamic shake table test. The crack pattern observed in the experiment is shown in Figure 2.10. The following research work has been used for validating the numerical results in this research work; for further details, the reader is advised to see chapter 3.

2.1.2. Experimental characterization of out-of-plane failure mechanisms

In this section, the experimental test conducted on the masonry structure subjected to different loading will be discussed. These loads generate a combination of stress in the masonry component, such as compression, tension, and shear (will be discussed subsection 2.1.3). The exceedance of the either one or in the combination of the stresses to their permissible limit results in failure at the component level (brick and mortar). The failure accumulates and leads to complete damage to the masonry structure. The capacity of the masonry wall to resist external loads primarily depends on the use of masonry walls in building structures and the type of load it experiences during its service life. The static load tests are performed to study the ultimate

(a) Specimen crack pattern at failure

(b) Picture of the specimen at the collapse

Figure 2.10: Two-way bending failure of URM subjected to shake table test.
Source: **?** **?** .

load capacity of the masonry structure to sustain external load without damage. Evaluating the masonry under static loading could be necessary for the structure experiencing heavy wind loads. Similarly, a dynamic test is of importance for the structure built in seismic active or dense traffic regions.

Static loading

In *static loading*, the wall is subjected to uniform load using the airbag system, primarily in the out-of-plane direction of the wall. The primary aim of the static loading test is to characterize URM walls for different slenderness ratio (height/thickness), varying the pre-compression level and effect of geometry (height and width) on the load capacity and failure mechanism on one-way (**?**]) and two-way (**?**])spanning URM wall. In a one-way spanning URM, the force-displacement behavior under the uniform loading can be idealized into a tri-linear curve, which is governed by three displacement parameters, namely Δ_1, Δ_2 and Δ_f as reported in **?**]. The ratio between the Δ_1/Δ_f and Δ_2/Δ_f depends on the material properties and degradation of the mortar joint at the pivot level. Later the effect of pre-compression on force-displacement behavior as studied by **?**] shows that the shape of the tri-linear curve changes its shape and depends on different pre-compression load (Figure 2.11).

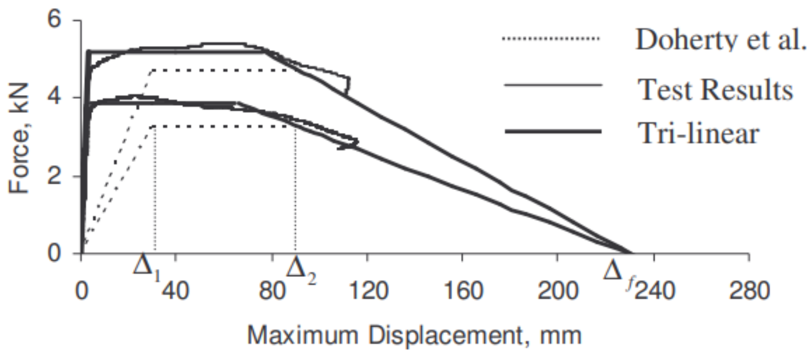

Figure 2.11: Force-displacement curve for varying pre-compression load. Higher pre-compression results in higher load capacity in out-of-plane direction.
Source: **?** **?**

In a two-way spanning wall, the support condition depicts the failure mechanism in the out-of-plane direction. Since each failure mechanism results in the different force-displacement curve, therefore, a general statement regarding a two-way spanning wall could not be made. Furthermore, no literature on testing a two-way spanning wall until failure is documented, therefore, based on the available results, as shown in Figure 2.12, the force-displacement relation can still be idealized using tri-linear shape. The effect of varying the pre-compression load on the monotonic static load test on the URM walls is shown in Figure 2.12b. Furthermore, the response shows that the wall has significant ductility while maintaining a constant load resistance.

Quasi-static

In the *quasi-static loading*, the displacement is applied over several cycles to investigate the performance of the structural systems. These cyclic loading patterns are applied at a slow rate in both positive and nega-

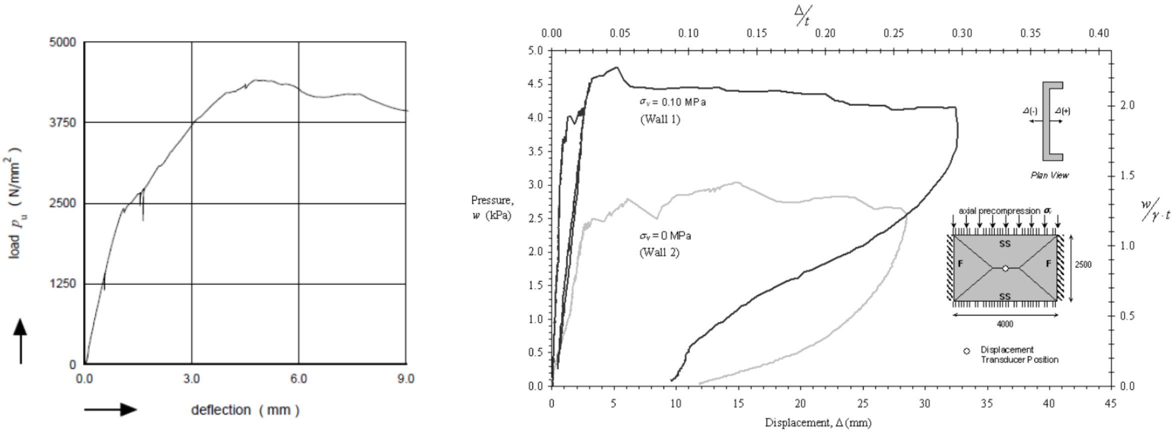

(a) Two-way spanning without return wall

(b) Two-way spanning wall connecting with return wall

Figure 2.12: Force-displacement behaviour of two-way spanning wall. (a) Vertical edge is not connected with return wall, Source: **?** **?** ; (b) The vertical edge is connected with return wall, Source: **?** [**?**]

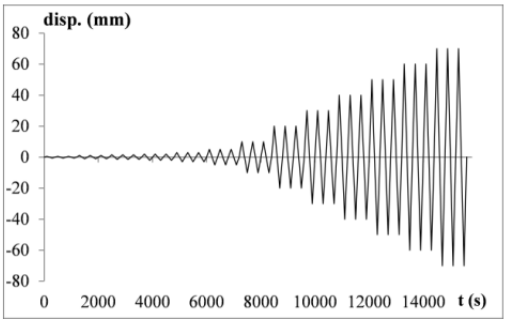

Figure 2.13: Details of complete loading scheme in quasi-static cycles in out-of-plane test.
Source: **?** **?**

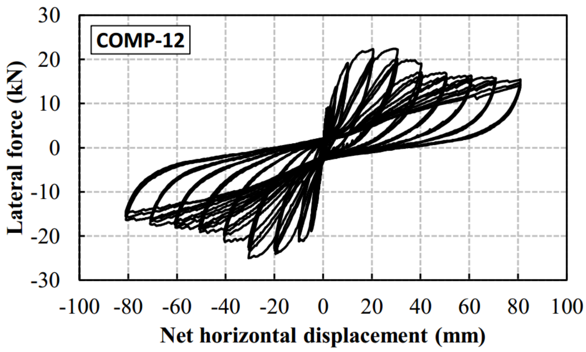

Figure 2.14: Lateral force vs the net horizontal displacement of COMP-12 wall.
Source: **?** **?**

tive displacement directions with increasing magnitude. As an example of one such load pattern, as shown in Figure 2.13. The purpose of this method of analysis is to study the hysteresis behavior under a predefined displacement pattern that can be used to quantify the structure's degradation and energy dissipation characteristics. The response of the two-way spanning wall, when subjected to cyclic-load in the out-of-plane direction, shows the degradation of stiffness and the load-carrying capacity with an increase in applied displacement magnitude ([**?**]). The quasi-static test on the specimen is used as a substitute for a dynamic test in which the degradation at each instance of loading can be captured effectively. This gives sufficient information about the weakest link in the structure. The quasi-static test has certain demerits. First, the large number of displacement cycles histories involved in the loading is more severe than the earthquake and monotonic loading, hence, it is considered as conservative for seismic assessment of the structure [**?**]. Second, the inertial effect neglected in the analysis; therefore, the real behavior of the URM structures under dynamic loading can not be fully captured.

Dynamic loading

In *dynamic loading*, the structure experience the load, which are random i.e., it does not have systematic pattern and varying in amplitude. Such a random load includes earthquakes, traffic vibration, wind load, etc. To understand the dynamic nature of the civil engineering structures is essential from both serviceability and ultimate strength point of view. In dynamic behavior, the total response is calculated, including the inertia force and the static equilibrium. The dynamic response of URM structures is conducted on a shake table test with an input signal from a recorded earthquake signal. This helps in recreating the actual dynamic loading condition on the structure by incorporating both inertial and viscous damping forces in the structure. During the earthquake, the failure mechanism in URM walls (in out-of-plane direction) is governed based on the exceedance of the ultimate displacement in the URM wall rather than the ultimate loading. Hence, it can be established that the wall has residual strength capacity, which will set the wall into motion without necessarily collapsing the wall. In the various post-earthquake assessments [**? ?**], the damage due to out-of-plane loading is the most commonly identified failure mechanism and is the primary cause of failure in the URM walls.

2.1.3. Material behaviour

The global failure in masonry is the result of an accumulation of failure at the local level, such as brick and mortar. Failure of either one of these component modifies the load-carrying mechanism in the masonry. The adhesion between the brick and mortar plays an important role in the uniformity of the masonry structure. The adhesion property is known as *bond strength* in masonry and is identified using the bond wrench test, according to EN 1052-5(2005). The bond between the brick and mortar is considered to be the weakest link, and many of the failure patterns either in the experiment or on-site are observed at this interface. Quasi-static test conducted by **?**] on perforated masonry specimen shows the failure pattern due to weak & strong bond strength (Figure 2.15). For strong bond strength, the crack goes through the brick, and for weak bond strength results in crack following the mortar-brick interface. **?**] performed the experimental study on flexural bond strength due to varying mortar composition. The author further emphasized the need for optimum moisture content in the brick unit at the time of casting to improve the bond strength. The failure observed due to strong bond strength is brittle in nature, while a weak bond leads to quasi-brittle failure i.e., having a residual resistance capacity after cracking.

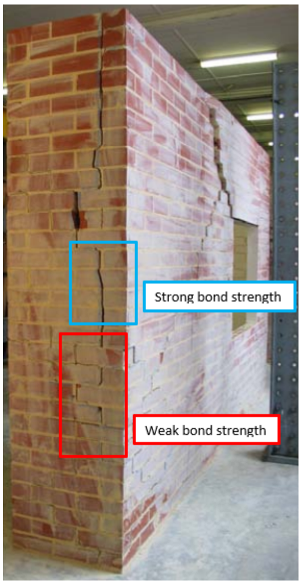

Figure 2.15: Crack pattern due to weak and strong bond strength in the masonry specimen tested under quasi static loading.
Source: **? ?**

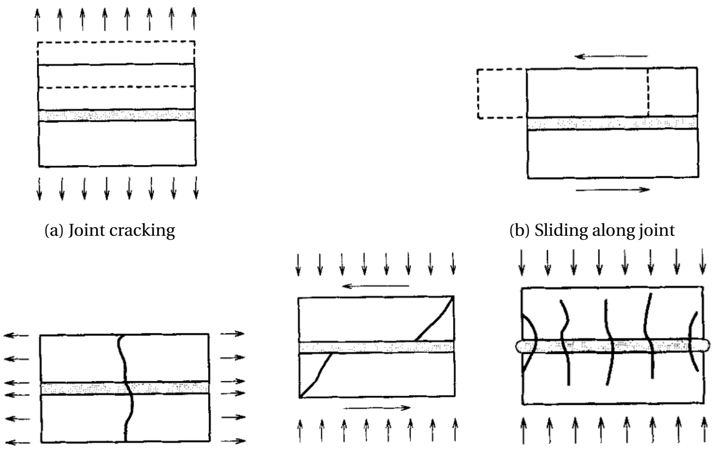

(a) Joint cracking

(b) Sliding along joint

(c) Cracking under direct tension

(d) Diagonal tension cracking

(e) Splitting of unit due to high compressive stresses

Figure 2.16: Basic failure mechanisms in masonry.
Source: **? ?**

In addition to the bond strength, the behavior of masonry structures in compression, tension, and shear is vital in defining the overall force and displacement capacity. Exceeding either one of the above strength values or in combination, will lead to one of the five underlying failure mechanisms, as shown in Figure 2.16. These fundamental failures at the component level are combined rapidly to form a global failure mechanism in masonry structures, as described previously. To understand the behavior of masonry structures, three material properties like compression, tension, and shear strength play a significant role in determining the internal resisting capacity.

Compression

In the context of building structures, masonry structures are designed primarily to carry gravity load; thus, remain in compression for most of there design life. The compressive behavior of masonry can be divided into two phases. Firstly, the elastic stage in which on the removal of load each element comes back to the

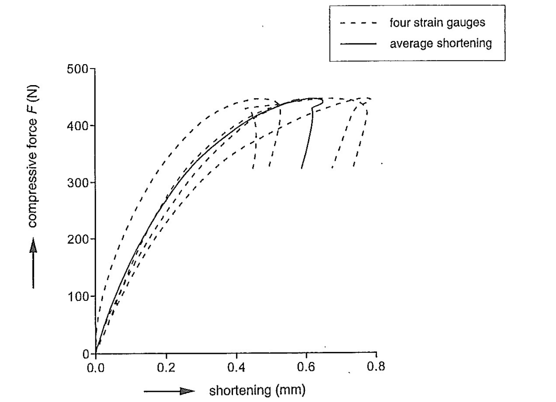

Figure 2.17: Force deformation relation of masonry prism.
Source: ? ?

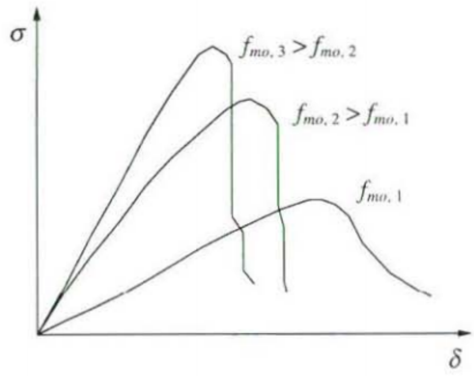

Figure 2.18: Uniaxial compressive behaviour of masonry due to different mortar compressive strength.
Source: ? ?

initial undeformed state. According to ?], masonry structure behaves as elastic before the formation of crack for 80 to 85% of the peak compressive load. Secondly, the inelastic stage in which minor crushing is seen (Figure 2.17) and permanent deformation in the material remains on the removal of compressive load. The study conducted by ?] using mortar of different compressive strength have investigated the effect on the uniaxial compressive behavior of masonry. Based on the findings, the higher strength mortar increases the compressive behavior of the masonry, but the post-peak behavior is brittlein nature, as evident from Figure 2.18. Under compression, failure due to splitting of the units (Figure 2.16e) occurred primarily because of different dilatancy behavior of mortar and brick.

Tension

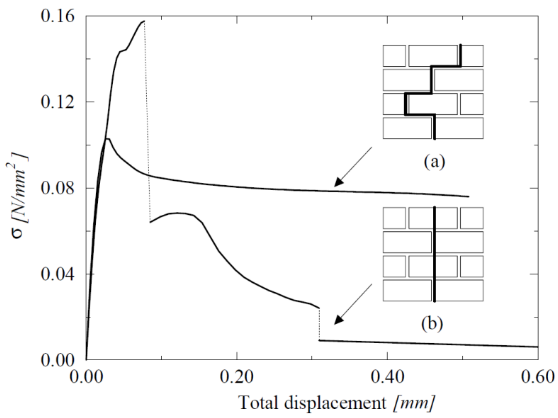

Figure 2.19: Stress vs displacement diagrams in tension (a) failure occur through head and bed joints forming stepped crack; (b) failure occurs through head joint and brick units
Source: ? ?

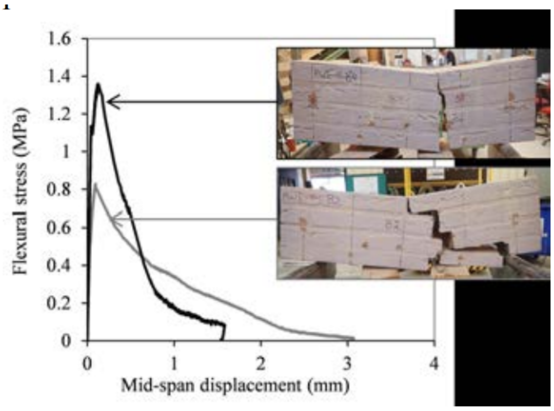

Figure 2.20: In-plane bending test: flexural stress-mid span displacement diagram.
Source :? ?

Like concrete, the tensile properties of the masonry can not be found based on the direct standard test because of high variability and difficulty in the standardization of test setup. Generally, the masonry structure is considered to be brittle when subjected to tensile load. An attempt to capture the direct tensile strength behavior in the direction parallel to the bed joint carried out in ?] shows the effect of weak bond strength on the failure pattern in the specimen (Figure 2.19). The tensile strength can be found indirectly from the results of a four-point bending test, both in-plane and out-of-plane (EN 1052-2) and using a bond wrench test (EN 1052-5). The in-plane and out-of-plane flexural test characterizing the material properties of the Dutch unreinforced masonry by ?] negates the common belief that masonry is brittle in nature. Furthermore, under flexure, masonry failure can be classified into quasi-brittle or brittle based upon the failure pattern. Besides, vertical crack that passes through brick has higher flexural strength capacity compared to diagonal crack but is less ductile (Figure 2.20). In the masonry structure, the tension strength exceedance in the direction perpendicular to the bed joint or the combination of compressive & shear causes either joint cracking (Figure 2.16a) or diagonal tension cracking (Figure 2.16d).

Shear

Shear behavior is one of the most important material properties of the masonry, which contributes significantly to resisting external in-plane loading. The in-plane sliding caused due to the exceedance of the shear strength reduces the internal contact area between the adjacent moving plates, and as a result, it decreases the load transfer path. While in out-of-plane loading, torsion (shear) in the bed joint is the internal resisting stress in the masonry. Therefore, the sliding of the plates not only reduces the torsion but also reduces the internal overlap, which leads to loss of flexural strength of the masonry. The observation of the experiment test performed on couplet and triplet specimens ([**?**],[**?**], [**?**], [**?**]) shows shear behaviour is primary influenced by the pre-compression and can be define based on the Coulomb friction failure criterion(Figure 2.22).

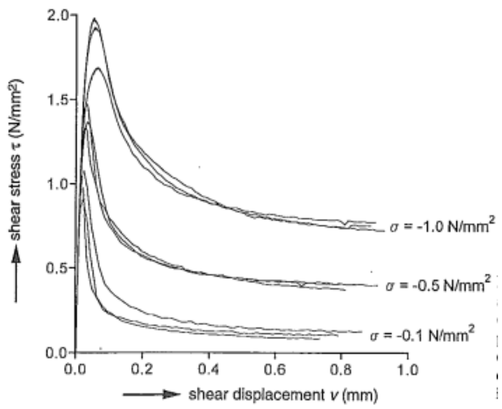

Figure 2.21: Stress vs displacement diagrams in tension (a) failure occur through head and bed joints forming stepped crack; (b) failure occurs through head joint and brick units Source: **? ?**

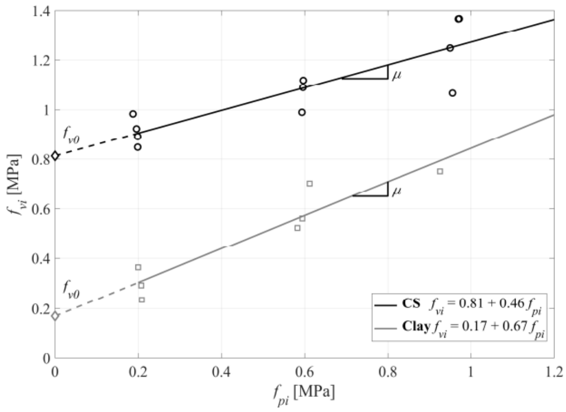

Figure 2.22: Coulomb's friction law representation of results of calcium silicate and clay triplet in direct shear. Source: **? ?**

2.2. Modelling strategies

In the last half-century, various modeling strategies have been developed to accurately simulate the behavior of masonry in the numerical analysis software. The basic workflow of any numerical analysis software includes pre-processing, processing, and post-processing stages (Figure 2.23a). In this section, various strategies developed in the pre-processing stage of the numerical analysis are detailed. *Pre-process* includes modeling of the physical structure (Figure 2.23b) into the finite element software (finite element model) so that all the necessary components such as load, support conditions can be given with necessary material parameters (Figure 2.23c). *Processing* stage includes the calculation part, where the software calculates the deformed shape, reaction, stresses, etc. to evaluate the strength of the structures. Finally, in *post-processing*, the results of the analysis are obtained in terms of deformed shape, strain plots, etc. (Figure 2.23d).

The various modeling strategies in the pre-processing stage includes discretization, material model, and analysis methods. Discretization includes the level of detailing that is required for effective modeling the structure so that required behavior can be captured. This includes micro-modeling, continuum modeling, macro-element modeling, and geometry-based modeling. For each level of discretization, associated material parameters are required for the proper definition of the constitutive law to simulate the masonry behavior.

Micro-modelling

In the *micro-modelling* (also known as block-based modeling strategies), each component, such as mortar, brick, and the interface connecting them are defined separately having different material properties. The material properties needed in these modeling strategies can be directly used from the lab test conducted on each component. These experimental tests can include a bond-strength test on couplet, shear strength

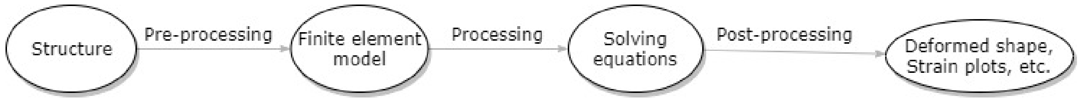

(a) Working flow-chart

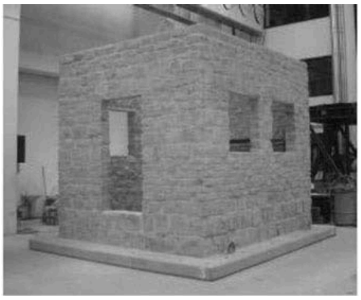

(b) Physical model of tested specimen.

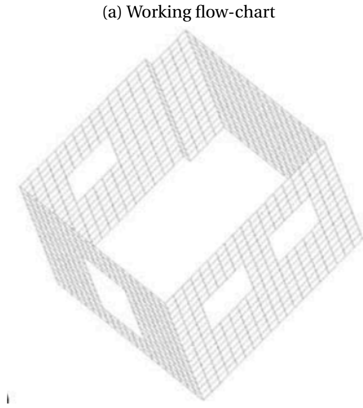

(c) Finite element discretization of the physical specimen

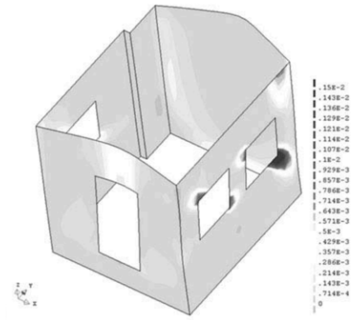

(d) Analysis result showing the principal strain plot.

Figure 2.23: Typical work-flow in the analysis of four wall building structure.
Source: **? ?**

test, etc. To avoid modeling at micro-level, simplified micro-modeling was suggested by **?**]. In simplified micro-modeling, all the non-linearity accounting due to mortar and mortar-brick interface are lumped into the interface element, and the brick size is increased to accommodate the mortar thickness, as shown in Figure 2.24. The benefit of micro-modeling is that the structure with complex geometry can be modeled, and

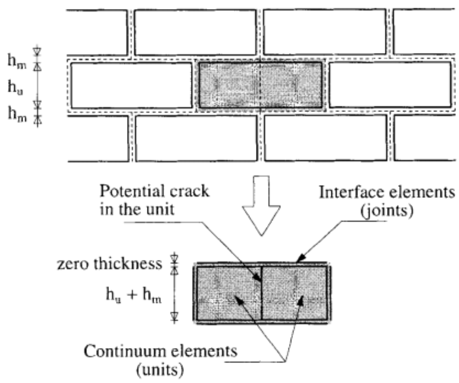

Figure 2.24: Simplified modelling strategies with zero-thickness interface. (h_u=unit thickness & h_m=mortar thickness)
Source:**? ?**

the result obtained does not require any demanding interpretations. The limitation of this model far exceeds the benefits as modeling each component is time-consuming as well; the analysis is in itself very demanding and needs very high computation power.

Continuum modelling

In *continuum modelling*, the brick and mortar are modeled as part of the same element. The definition of the constitutive law is the most essential and challenging part governing in continuum modeling. The constitutive law needed in this modeling strategy is homogenous over the element. This homogenization of the constitutive law can be derived based on direct approaches & multi-scale approaches. The important aspect of the mechanics of masonry is the definition of non-linearity in the constitutive law. Several models have been proposed in the past based on either fracture mechanics or plasticity theory for crack formation and propagation in concrete [**?**]. The limitation of this constitutive law is in their application to masonry structures. One such limitation is in considering masonry as isotropic material rather than orthotropic. The first application of the orthotropic plasticity model to represent the inelastic behavior of the orthotropic material is shown in Figure 2.25. The detailed description of the two constitutive laws used in the analysis of masonry will be discussed in chapter 4.

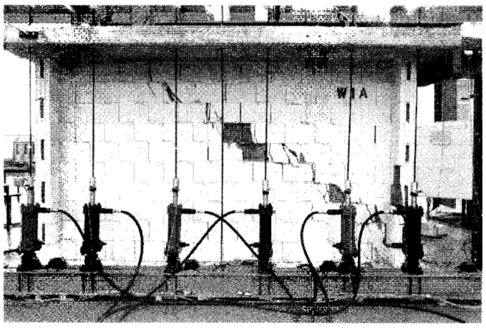

(a) Experimental failure patterns at ultimate stage

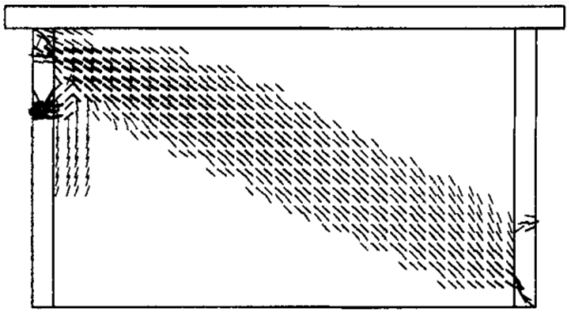

(b) Crack pattern from numerical modelling

Figure 2.25: Orthotropic plasticity model for masonry wall structure used in continuum modelling strategy.
Source : **? ?**

The benefit of defining the appropriate constitutive law in continuum modeling is in its independence of mesh element size. Therefore, mesh size could be larger than the brick size. As a result, the analysis could require less computational effort and do not require much time in setting up the model as done in the block-based model. Furthermore, analysis for different load applications such as static loading under in-plane and out-of-plane directions, quasi-static, and transient analysis could be carried out efficiently.

Macro-element modelling

In a macro-element modeling approach, the structure is idealized into panel-scale structural components, typically piers, spandrels, and rigid parts. The piers and spandrels are parts of deformable elements which are joined together with rigid parts. The non-linear response of the structure is concentrated on the deformable panels where damage could occur. Whereas, the rigid parts are not usually subjected to any damage [**?**]. An example, one idealization of the structure components into the deformable and rigid parts is shown in Figure 2.26. The primary focus of the macro-modeling approach is to understand the global seismic response of the masonry buildings. Prior identification of the structural components (spandrels and piers) based on the damage pattern of the real building structures is required. This definition could be challenging in case of irregular openings. However, macro-elements based modeling is a simplified approach for the analysis of masonry structures and requires little computational efforts, but present some drawbacks such as

- The activation of the failure mode due to out-of-plane response of masonry wall is prevented.
- Macro-element could not account for structural detailing such as connection between orthogonal walls.
- Priori definition of piers and spandrel could lead to definition of a mechanical system which does not represent true behaviour of masonry structure.

Geometry-based modelling

In this modeling approach, the structure is modeled as a rigid body. Geometry-based modeling gives fundamental information such as stability and collapse mechanisms based on a limit analysis-based solution (based on static or kinematic theorem). The static theorem is based on Heyman's rigid no-tension model [**?**] and used mainly for the assessment of the statical safety of masonry vaulted structures. However, for studying the seismic vulnerability of masonry buildings, the Kinematic theorem-based approach is used in the past decades. Due to the simplicity and effectiveness of the kinematic approach, it has been adopted into the Italian code [**?**]. The limitation of this modeling approach is the inability to provide post-peak and displacement capacity of the masonry structures, which is essential for an assessment of structural capacity under seismic loading.

Summarizing the different modeling strategies, the comparison based on relevant parameters that could help in identifying the efficient modeling strategies in understanding the dynamic behavior of the masonry are tabulated in Table 2.1.

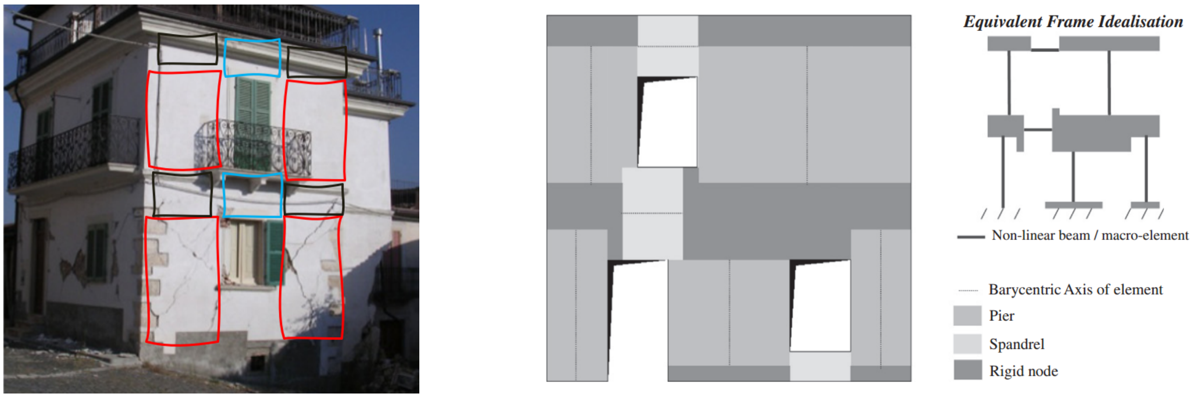

(a) In-plane damage from L'Aquila 2009 earthquake

(b) Equivalent frame idealization for irregularly distributed openings.

Figure 2.26: Equivalent beam based approach. (a) In-plane failure modes with damage concentration in piers (shown in red), spandrels (in blue), and rigid elements (in black); (b) The equivalent frame idealization for masonry structure based on the identification of piers and spandrels.
Source : **? ?**

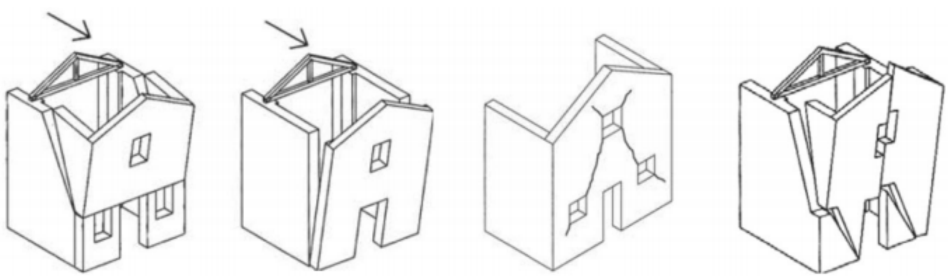

Figure 2.27: Examples of collapse mechanisms needed for the seismic assessment of the masonry structure in kinematic theorem based approach.
Source : **? ?**

	Block based model	Continuum model	Macro-element model	Geometry model
Discretization	Minor structural detailing	Mesh discretization	Panel scale	Structure model as rigid body
Material model	From small-scale experiments	From direct approach	Phenomenological or mechanically based material model	Static-theorem and kinematic-theorem
Computational cost	Huge	Large	Limited	Minor
Users	Academics and research consultancy	Academics and industry level	Academics and industry level	To investigate structural equilibrium and collapse
Failure modes	Clear and not required demanding interpretations	Clear and may require interpretation	Global seismic response	Suitable for complex failure mechanism
Limitation	-Approximated if actual bond behaviour is unknown. -Time consuming during assemblage and analysis.	Difficult to model complex structure	-Identification of piers and spandrel in complex structure. - Local failure mode associated with OOP response of masonry is not taken into account.	-Limited to identification of collapse multiplier and collapse mechanism. -No information about ultimate displacement and post-peak behaviour
	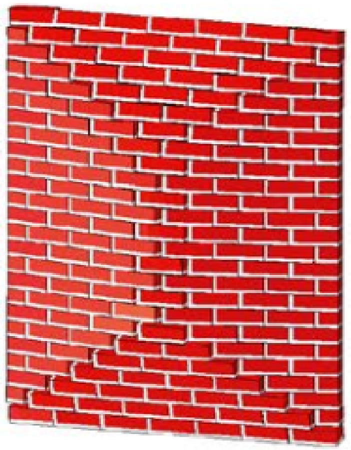	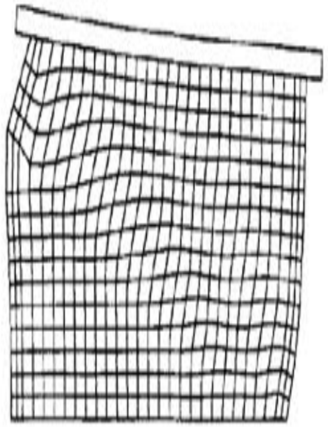	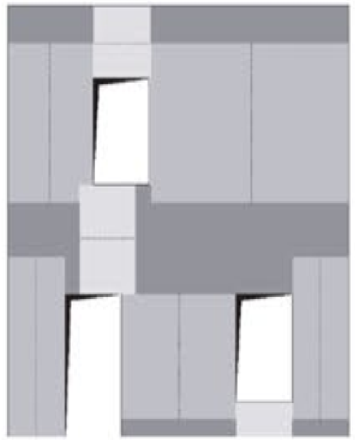	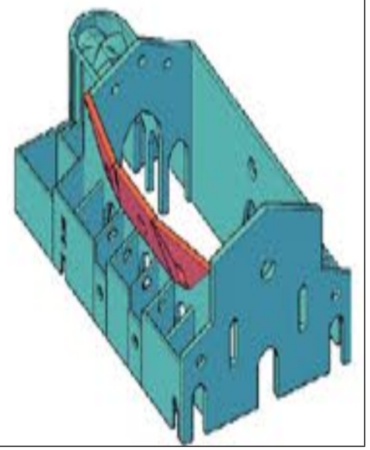

Table 2.1: Summary of modelling strategy for the computational analysis of URM.
Source:**? ?**

2.3. Seismic analysis methods

This section discusses the overview of the methods for the seismic analysis of structures in numerical analysis. This method includes a non-linear static and non-linear time history (NLTH) method. In the non-linear static analysis, two different load patterns are applied, such as uniform and based on the first mode-shape. While the NLTH is the non-linear dynamic method of analysis, which is dynamic load is taken into account by applying a ground motion signal directly to the structure. The starting point for non-linear static analysis (mode proportional load) and NLTH the method is the equation of motion, derived based on the conservation of impulse

$$\left(\sum F\right) dt = d(m\dot{u}) \tag{2.2}$$

Where, $\sum F$ is the resultant of the external and internal (from internal stresses) load, m is the mass and $\dot{u}$ is the velocity. In solid mechanics the mass at all instant remains same, therefore based on the conservation of mass, Equation 2.2 can be transformed into the equation of motion (**??**).

$$\sum F = m\ddot{u} \tag{2.3}$$

Where $m\ddot{u}$ is the inertial contribution, if it is negligibly small, the equation of motion reduces to the equilibrium equation $\sum F = 0$. The dynamic behavior of the non-loaded (no external load) structure gives insight into the characteristic behavior of the structure via the natural frequencies and eigenvectors (free vibration analysis). Furthermore, the response of a structure to any load is consists of a solution of the free vibration analysis plus the particular solution.

Free Vibration

In the free vibration, the set of coupled differential equation is solved given by Equation 2.4. The brief derivation of the equation of motion of the system with n degrees of freedom is given in Appendix A.

$$\mathbf{M}\ddot{\mathbf{x}}(t) + \mathbf{K}\mathbf{x}(t) = 0. \tag{2.4}$$

Here **M** is the mass matrix and **K** is the stiffness matrix, and **x** consists of all the degree of freedoms. The general solution of the above equation can be searched in the following form as given by Equation 2.5.

$$\mathbf{x}(t) = \sum_{i=1}^{2N} \tilde{\mathbf{X}}_i sin(\omega_i t + \phi_i) \tag{2.5}$$

Where, ω is the natural frequency, and ϕ is the phase angle. Substituting the general solution (Equation 2.5) into the equation of motion (Equation 2.4), this results in a homogeneous set of equations given as Equation 2.6.

$$(\omega_i^2 \mathbf{M} + \mathbf{K})\tilde{\mathbf{X}}_i = 0 \tag{2.6}$$

This homogeneous set of n algebraic equation is called "the generalised eigenvalue problem" [**?**], in which ω^2 is called the eigenvalue and $\tilde{\mathbf{X}}_\mathbf{i}$ contains an associated eigenvector. For $\tilde{\mathbf{X}}_\mathbf{i} = 0$ gives the zero vector, which is trivial solution, as it represent the state of static equilibrium. While, the non-trivial solution can be found if the determinant of the matrix of coefficients is equal to zero.

$$det(\omega_i^2 \mathbf{M} + \mathbf{K}) = 0. \tag{2.7}$$

This gives the polynomial equation of degree n in ω^2, which is called the characteristic polynomial. The eigenvectors associated with the n natural frequencies ω_1, ω_2,...,ω_n are called the principal modes of vibration. For the system with n degrees of freedom have n principal modes of vibration hence free vibration is the summation of all possible eigenmodes as given as Equation 2.8.

$$\mathbf{x}(t) = \sum_{i=1}^{N} \tilde{X}_i A_i sin(\omega_i t + \phi_i). \tag{2.8}$$

The constants of the above solution such as A_1, A_2, ..., A_N and ϕ_1, ϕ_2, ...ϕ_N can be found from the initial conditions i.e. x(0) and $\dot{x}(0)$.

Non-linear time history analysis

In the dynamic loading, inertial forces account for the significant portion of the loads that are applied to the structure. This inclusion of inertial force is not considered in the static analysis, which overestimates the structural capacity to resist external loads. The static method of analysis used for approximating the dynamic behavior of a structure, such as a pushover method of analysis, is limited in their application. The pushover method of analysis gives a good prediction for the structure when a fundamental mode of vibration is the dominant mode. Furthermore, pushover analysis does not account for the change in the mode of the structure due to the occurrence of the failure in the structure.

To overcome these limitations, Non-Linear Time History (NLTH) analysis is used to describe the dynamic behavior of the structure entirely. In this method, the structure is directly subjected to actual earthquake records to investigate dynamic effects. NLTH analysis takes into account the inertial effect and hence represents the actual dynamic behavior of the structure. The analysis is computationally heavy i.e., it takes a long time for completion and requires large disk space to save the result. That is why it is not very popular among engineers and mainly used in academics. Apart from the above limitation, these methods accurately provide the behavior of the structures when subjected to earthquake motion. The problem is discretized not only in a spatial domain but also in the time domain to arrive at a full discretized set of equations. The time discretization for a linear and non-linear set of equations (Equation 2.9) is reported below.

$$\mathbf{M}\mathbf{x}(\ddot{\mathbf{t}}) + \mathbf{C}\mathbf{x}(\dot{\mathbf{t}}) + \mathbf{f}_{int}(\mathbf{x}, \dot{\mathbf{x}}, \epsilon, \sigma, t, ...) = \mathbf{f}_{ext}(t). \tag{2.9}$$

Where,

- **M**= Mass matrix of the system.
- $\mathbf{f}_{int}$= **Kx**(t) for linear situation, for geometrical and physical non-linear analysis it is depend on the actual stress distribution satisfying all non-linear conditions.
- **C**= Damping matrix of the system based on the Rayleigh damping and given as = $\alpha\mathbf{M}+\beta\mathbf{K}$.
- α= mass coefficient; β=stiffness coefficient.
- **x**= degree of freedom of the system.
- $\dot{\mathbf{x}}= \dfrac{d\mathbf{a}}{dt}$.
- $\ddot{\mathbf{x}}=\dfrac{d\ddot{\mathbf{a}}}{dt}$.

The above system of equation are solved using time stepping algorithms i.e. given the values of parameters ($\mathbf{a}$,$\dot{\mathbf{a}}$, $\ddot{\mathbf{a}}$) at time t_n, the values at time step $t_{n+1}(=t_n + \Delta t)$ can be calculated based on the algebraic formulas. Time stepping schemes are distinguished based on explicit and implicit method.

Explicit integration

In the explicit time integration method, information of the system at n^{th} (also $(n-1)^{th}$) step are used to compute the information at $(n+1)^{th}$ step. These scheme generally required low computation effort because of the need to solve algebraic equation. Central difference method, Runge-Kutta methods are some of the explicit time integration schemes.

Implicit integration

In this scheme, not only the information at the previous step i.e., n and n-1, are used but also rely on the $(n+1)^{th}$ step in computing the information. This method of solution generally required high computational effort. Newmark method, Hilber-Huges-Taylor(HHT), Euler backward, and Trapezium are some of the widespread integration schemes that are primarily used in finite element packages.

The choice of time integration scheme largely depends on the stability and accuracy of the method. Usually, explicit time integration has a high degree of accuracy (of order O(Δt^4)) for the Runge-Kutta method), but this scheme is not stable. *Stability* here refers to the range of time step for which equation can be solved with error within the limit and do not grow with step. The implicit schemes have a degree of accuracy of order two generally ($O(\Delta t^2)$ for Newmark, $O(\Delta t)$ for Euler backward), but the scheme is stable. Furthermore, in the explicit time integration scheme, the numerical solution drifts from the equilibrium path for large time steps and non-linear behavior [**?**]. In the implicit scheme based on the parameter chosen, the accuracy of the solution can be controlled. For example, in Newmark method is unconditionally stable if parameters β and γ, which define the nature and properties of the algorithm.

$$2\beta \geq \gamma \geq \frac{1}{2} \tag{2.10}$$

For $\gamma = \frac{1}{2}$, Newmark scheme is second-order accurate. Therefore, to get the solution which is both accurate and stable, implicit time integration scheme such as Newmark time integration will be a legitimate choice for non-linear history analysis.

2.4. Conclusions

In conclusion, the chapter provides the foundation that will be sufficient in evaluating the performance of the numerical analysis carried out in this thesis work. This chapter divided into two parts, first describing the global response of the URM walls under the action of in-plane and out-of-plane loading ()for one-way and two-way spanning walls). The two-way spanning wall with out-of-plane loading can sustain a higher lateral load with large displacement capacity without complete failure. Then the behavior of masonry under different lateral loading conditions is presented. Studying the behavior under different loading is based on the use of masonry in the building structures and the type of loads it experiences during its service life. The importance of different material properties is elaborated for compression, tension, and shear, for the out-of-plane loading tension and shear are the primary internal resisting stress component that is governing in resisting the external load in the URM walls.

The second part focused on the modeling strategies available and chose the most suitable and relevant for the numerical analysis in the current study. First of all, the choice of level of detailing that would be necessary for the study out of the already available is made by evaluating based on their applications, modes of failure identification, and limitations. Following this, the description of seismic analysis methods for evaluating the dynamic behavior of the structure is presented with different time discretization techniques.

3

Case study: out-of-plane shake table tests on two-way spanning calcium silicate walls

Introduction

The following chapter comprises the detail description of the experimental setup used in the testing campaign for unreinforced masonry (URM) walls at EUCENTRE. The experiment aimed to study the two-way bending behavior of unreinforced masonry structures subjected to out-of-plane seismic excitation. In the experimental campaign, five specimens with usual met boundary conditions applied overburden pressure and presence/absence of openings was tested. The incremental input motion applied to all the specimens until the ultimate collapse. All the specimens tested the sustained acceleration of 1 g without any damage but instead showed a brittle response after damage. Furthermore, the acceleration capacity of the specimen restrained on all four edges was high compared to the wall free on top. Specimen with calcium silicate brick exhibited brittle response achieving peak load at a very low-level of displacement. On the other hand, clay masonry specimen sustained high load with a large displacement capacity and high residual strength.

The following chapter provides an extensive description of experimental setups like wall support conditions, test setup, material properties, and loading scheme. The specific details presented will be required for numerical modeling. Furthermore, the experiment outcomes in terms of deformed shape, failure mechanisms, and force-displacement hysteretic curves will be used as a benchmark to validate the numerical model results.

3.1. Specimen geometry and boundary conditions

The experimental test campaign comprises of five different sets of a full-scale wall (Table 3.1). Each specimen had a U-shaped plan, consisting of a 1m long return wall (or pier), which provide the vertical restrains at the edge of the OOP panel (main wall) of length (l_{OOP} =) 4m. Three out of five specimens were made of single leaf calcium silicate (CS) brick measuring 212 x 102 x 71mm (one with eccentric opening), while the fourth wall was made of single leaf clay brick measuring 208 x 98 x 50mm. The fifth wall was a cavity wall with an L-shaped wire connecting out and inner leaf, which was constructed using clay and CS bricks, respectively. The masonry wall with CS had 34, while clay brick specimen had 46 layers. Each layer was joint using 10mm mortar joined, totaling the height of (h_{OOP} =) 2.75m and 2.76m for the CS and clay bricks specimens. The main wall and pier were connected with an alternate row of header joints, providing full moment restrain at the vertical edge.

The bottom section of all the specimens was connected to the foundation with mortar bed-joint achieving the fixed support condition at the bottom. To get the fixed support condition at the top of the main-wall

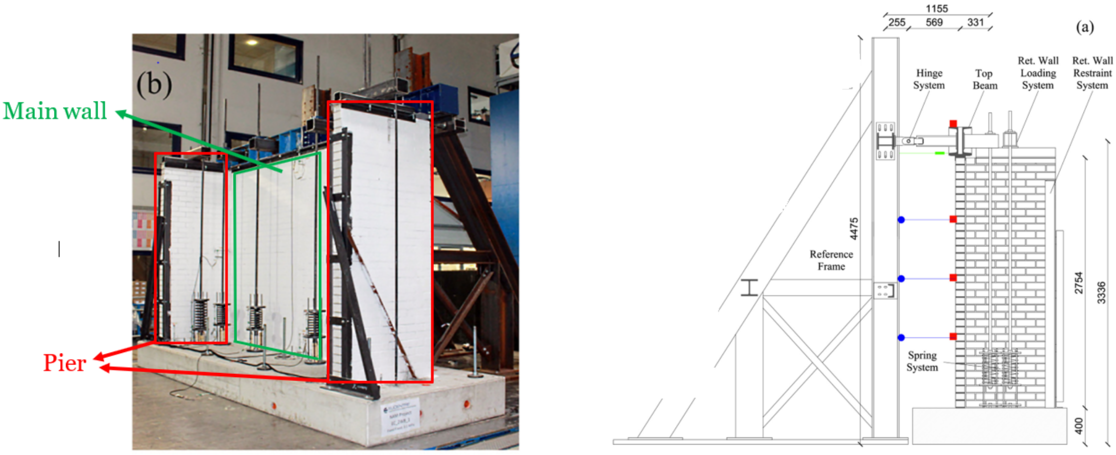

(a) Physical model

(b) Geometry of test setup

Figure 3.1: Experimental setup of the test specimen. (a) Testing layout of CS-010/005-RR; (b) Geometry of the test setup showing the rigid frame and pre-compression loading system.

in specimen CS-010-RR, the gap between the beam and bricks was filled with high strength mortar. Furthermore, the uppermost layer of brick was clamped with the L-shaped steel profiles (Figure 3.2a). Whereas the main wall was free without any horizontal restrains by lifting the top beam (Figure 3.2b) for all the other specimens. The top beam of the return wall was connected with the steel frame (reference frame) to allow the transmission of the base acceleration at the upper part of the return wall, irrespective of the top support condition in the main wall (Figure 3.2c). In the out-of-plane direction of the return wall, the steel columns were attached at the vertical end of the return wall (Ret wall restraint system.) shown in Figure 3.1b. In the Table 3.1, dimensions, mass, pre-compression on main wall & pier, the horizontal support condition at the top & bottom of the main wall are provided. Based on the brick type, boundary condition, and pre-compression, the short nomenclature is adopted. "CS (or)" referred for calcium silicate (or clay) brick, "010 (or 000)" for pre-compression load, and "RR (or RF)" for the bottom and top support condition. The same specimen name will be used throughout the report.

Specimen	l_{OOP} (m)	h_{OOP} (m)	M(kg)	σ_v(MPa) OOP wall	σ_v(MPa) RET wall	Horizontal restrain bottom / top	
CS-010-RR	3.98	2.75	2056	0.10	0.10	Fixed(R) Fixed(R)	
CS-005-RR	3.98	2.75	2056	0.05	0.05	Fixed(R) Fixed(R)	
CS-000-RF	3.98	2.75	2056	-	0.05	Fixed(R) Free(F)	
CSW-000-RF	3.98	2.75	1530	-	0.05	Fixed(R) Free(F)	
CL-00-RF	4.02	2.76	2178		0.05	Fixed(R) Free(F)	
CAV-000-RF CS Clay	3.98 4.39	2.75 2.76	2056 2375	- -	0.05 0.05	Fixed(R) Free(F) Fixed(R) Free(F)	

Table 3.1: Details of boundary conditions and overburden pressures on different specimens.
Source: **?**]

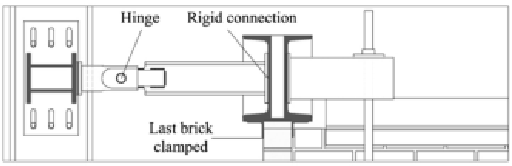

(a) Connection between top beam and frame for CS-010/005-RR

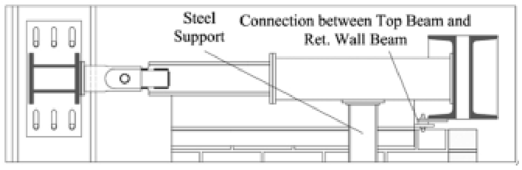

(b) Connection between top beam and Pier/return wall

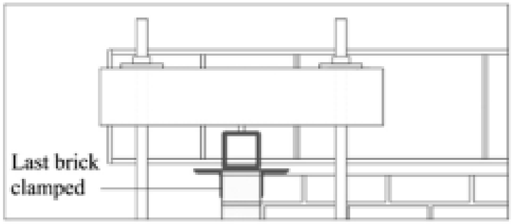

(c) Connection between top beam and frame for CS-000-RF

Figure 3.2: Boundary conditions at the top of the specimens.

3.2. Experimental Setup

The pre-compression load on the return wall was applied in all the specimens by pulling down using the spring and making sure the pre-compression does not exceed 5% at the collapse of the masonry wall. For the test specimen CS-010-RR, at the starting of the test procedure pre-compression load of (σ_v =), 0.10 MPa was applied on both the main wall (σ_v OOP wall) and the pier (σ_v RET wall). The response observed under the applied pre-compression was stiff during the dynamic loading. Therefore, to prevent failure at the unrealistic ground acceleration, the pre-compression was reduced to 0.05 MPa on both the main-wall and pier. The pre-compression of 0.05 MPa was applied to the return wall in the specimens with no pre-compression and restrain at the top of the main wall. The specimens were cemented to the reinforced concrete foundation using mortar. The foundation was made to rest by bolting it on the shake-table. The top beam on the specimen was connected to the steel frame via the horizontal beam. The base of the steel frame is rigidly connected to the shake-table to make sure the input base excitation is transferred to the top of the specimens without delay and amplification. For the acquisition of data, instrument like potentiometer and accelerometers, which measures the relative displacements on the specimen with respect to a steel frame and to record the acceleration respectively. Besides, a 3D optical acquisition system was used to capture the deformed shape of the specimens at different instances of time during the testing.

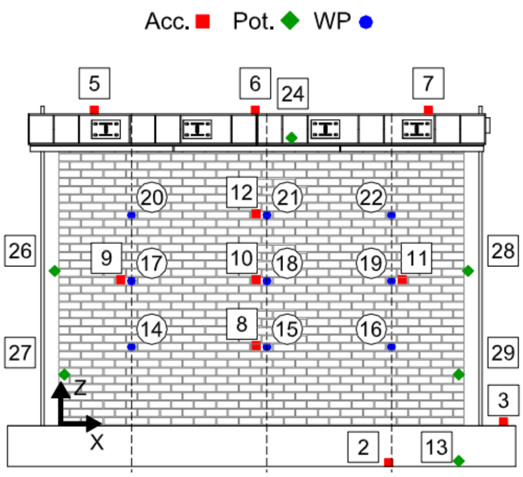

(a) CS-010-RR and CS-005-RR

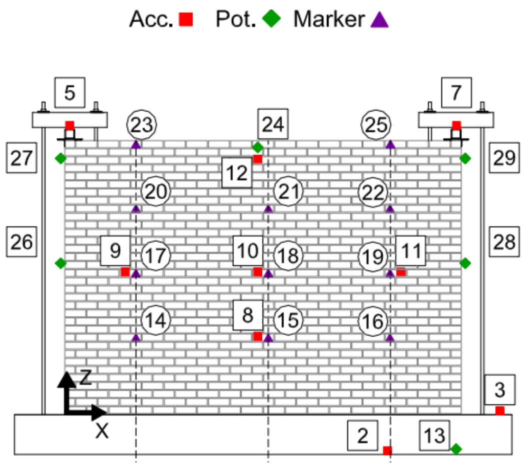

(b) CS-000-RF

Figure 3.3: Location of instrument and data acquisition point in the specimens, Acc: Accelerometer, Pot: Potentiometer, and WP: Wire Potentiometer (a)CS-010-RR and CS-005-RR, and (b)CS-000-RF.

3.3. Material Properties

The detailed test on the materials to identify the mechanical properties of both components (units & mortar) and as a composite was performed. European standards followed in determination of the mechanical properties are tabulated in Table 3.2. The material characterization of the masonry specimen with calcium silicate brick that will be necessary as an input parameter during numerical modeling is given in Table 3.3

EURO CODE	Purpose
EN 1015-11 (1999)	flexural (f_t) and compressive strength (f_c) of the mortar.
EN 77201(2011) & NEN 6790 (2005)	flexural tensile strength (f_{bt}) of units in two laying planes.
EN 1052-1 (1998)	Masonry wallet in compression (f_m).
EN 1052-3 (1998)	Initial shear strength (f_{vo}) & friction coefficient (μ) in translation.
EN 1052-5 (1998)	Bond strength of masonry (f_w).
EN 1052-2 (1999)	Out-of-plane flexural strength (f_{x2}) .

Table 3.2: Details of European standards and the purpose for respective mechanical properties.

Material Properties	Symbol	Units	Value
Density of masonry	ρ	kg/m^3	1833
Compressive strength of mortar	f_c	MPa	8.79
Flexural strength of mortar	f_t	MPa	2.76
Compressive strength of masonry unit	f_b	MPa	8.79
Bond strength	f_w	MPa	0.95
Flexural strength of masonry unit (weak axis)	f_{btw}	MPa	2.61
Flexural strength of masonry unit (strong axis)	f_{bts}	MPa	3.16
Compressive strength of masonry in perpendicular direction to bed joints	f_m	MPa	9.74
Elastic modulus of masonry	E_m	MPa	5005

Table 3.3: Material properties of masonry tested based on European standards.

3.4. Loading conditions

Firstly, on the specimens, the pre-compression load was applied, and it was followed by incremental dynamic base excitation. In the incremental dynamic tests, three input motions, namely, FHUIZ-DS0, FEQ2-DS3, FEQ2-DS4 with different scaling, were used. The details of the dynamic loading sequence are given in Table 3.4. Signal FHUIZ-DS0 is a second-floor accelerogram obtained from a calibrated TREMURI model of the tested full-scale house when subjected to the ground motion recorded at Huizinge, the Netherlands on 16^{th} April 2012. The other two acceleration signal FEQ2-DS3 and FEQ2-DS4 were scaled EQ2 ground motion. Where EQ2 is second-floor accelerograms of the full-scale house obtained from a 2015 hazard study of the Groningen region. Besides, fourth input acceleration motion SSW was an artificial input signal characterized by a wide spectral shape, and duration was used for the sole purpose of inducing the collapse of CS-005-RR specimen. The time history used for the base excitation is given in Figure 3.4. SSW input motion typically consists of sine impulses with gradual increasing periods to excite the broad range of frequencies in the specimen.

The sequence of input motions for each specimen is shown in Table 3.4 with corresponding scaling factor (S.F.), peak table acceleration (PTA), and maximum wall displacement. For the specimen CS-010-RR/CS-005-RR, the displacement at mid-height of the specimen was measured, while for all the other specimens, the top-height displacement was measured. The highlighted part in the Table 3.4 is conforming to the pre-compression of 0.10 MPa for the first specimen (CS-010-RR). The data written with a bold black letter correspond to the first crack run, while the data written with a bold red letter shows the complete collapse in the specimens.

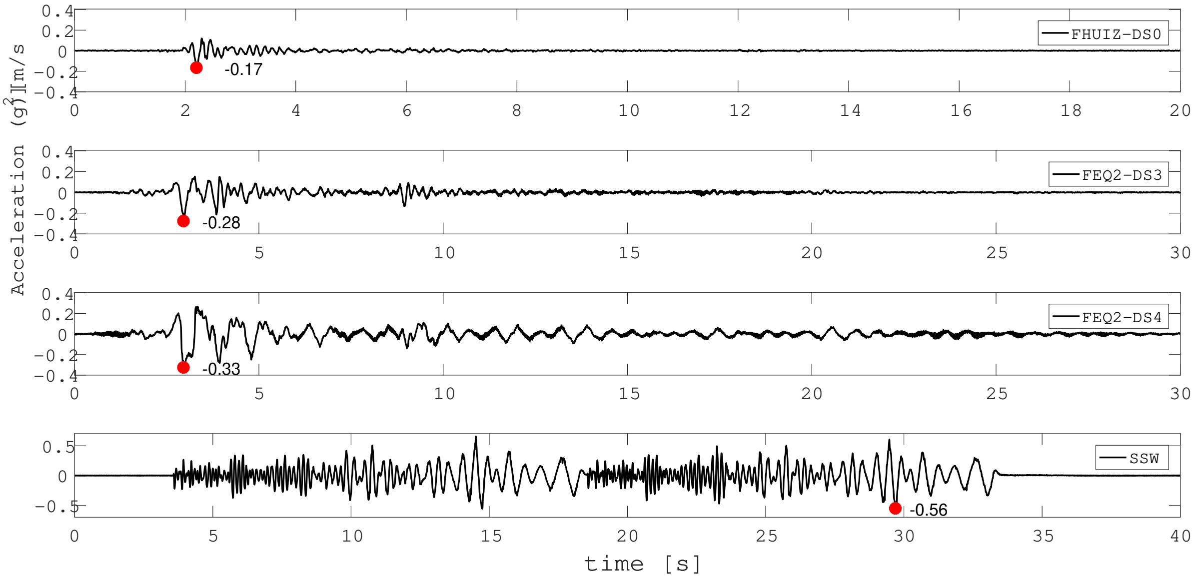

Figure 3.4: Acceleration-time histories of input motion in shake table

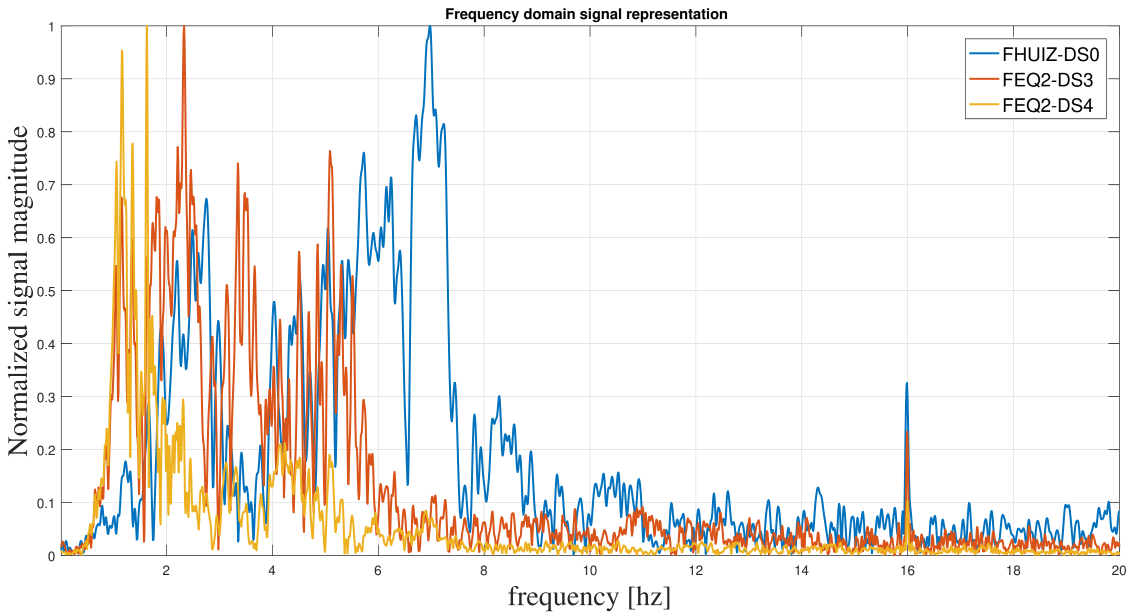

Figure 3.5: Frequency content of the input motion signal

	CS-010-RR		CS-005-RR		CS-000-RF				CSW-000-RF				CL-000-RF				CAV-000-RF			
T#	**Test Input**	**S.F.**	***PTA* [g]**	***MHD* [mm]**	**Test Input**	**S.F.**	***PTA* [g]**	***TD* [mm]**	**Test Input**	**S.F.**	***PTA* [g]**	***TD* [mm]**	**Test Input**	**S.F.**	***PTA* [g]**	***TD* [mm]**	**Test Input**	**S.F.**	***PTA* [g]**	***TD* [mm]**
1	RN	100%	+0.06	-	RN	100%	-0.04	-	RN	100%	+0.05	-	RN	100%	-0.07	-	RN	100%	-0.06	-
2	FHUIZ-DS0	50%	-0.07	+0.1	FHUIZ-DS0	50%	-0.07	+0.2	RN	100%	+0.06	-	FHUIZ-DS0	50%	-0.074	-0.3	FHUIZ-DS0	50%	-0.07	-0.3
3	FHUIZ-DS0	100%	-0.16	+0.2	FHUIZ-DS0	100%	-0.15	+0.5	FHUIZ-DS0	50%	-0.07	-0.3	FHUIZ-DS0	100%	-0.16	+0.5	FHUIZ-DS0	100%	-0.16	+0.5
4	FHUIZ-DS0	150%	-0.20	+0.3	FHUIZ-DS0	150%	-0.23	+0.7	FHUIZ-DS0	100%	-0.16	+0.5	FHUIZ-DS0	150%	-0.19	+0.6	FHUIZ-DS0	150%	-0.23	+0.7
5	FEQ2-DS3	40%	-0.11	+0.1	RN	100%	+0.08	-	FHUIZ-DS0	150%	-0.22	+0.7	FEQ2-DS3	50%	-0.13	+0.5	FEQ2-DS3	50%	-0.13	+0.6
6	FEQ2-DS3	89%	-0.22	+0.1	FEQ2-DS3	50%	-0.16	+0.4	FEQ2-DS3	50%	-0.13	+0.5	FEQ2-DS3	89%	-0.23	+0.8	FEQ2-DS3	89%	-0.26	+1.0
7	FEQ2-DS3	100%	-0.27	+0.2	FEQ2-DS3	89%	-0.23	+0.6	FEQ2-DS3	89%	-0.25	+0.9	FEQ2-DS3	100%	-0.28	+0.9	FEQ2-DS3	100%	-0.27	+1.1
8	FEQ2-DS3	125%	-0.31	+0.2	FEQ2-DS3	100%	-0.25	+0.7	FEQ2-DS3	100%	-0.27	+1.0	FEQ2-DS3	125%	-0.31	+1.1	FEQ2-DS3	125%	-0.32	+1.4
9	RN	100%	+0.07	-	FEQ2-DS3	125%	-0.34	+0.9	FEQ2-DS3	125%	-0.31	+1.2	RN	100%	-0.06	-	RN	100%	+0.06	-
10	RWA	100%	+0.30	-0.2	FEQ2-DS4	100%	-0.39	+1.0	RN	100%	+0.05	-	FEQ2-DS4	50%	-0.16	-0.8	FEQ2-DS4	50%	-0.16	-0.9
11	FEQ2-DS4	50%	-0.17	-0.1	FEQ2-DS4	125%	-0.38	-1.3	FEQ2-DS4	50%	-0.16	-0.8	FEQ2-DS4	100%	-0.32	-1.3	FEQ2-DS4	100%	-0.34	-1.5
12	FEQ2-DS4	100%	-0.32	-0.2	FEQ2-DS4	150%	-0.46	-1.6	FEQ2-DS4	100%	-0.30	-1.4	FEQ2-DS4	125%	-0.39	-1.6	FEQ2-DS4	125%	-0.39	-1.8
13	FEQ2-DS4	125%	-0.38	-0.3	FEQ2-DS4	175%	-0.54	-2.0	FEQ2-DS4	125%	-0.39	-1.7	FEQ2-DS4	150%	-0.48	-1.9	FEQ2-DS4	150%	-0.48	-2.0
14	FEQ2-DS4	150%	-0.47	-0.3	FEQ2-DS4	200%	-0.68	-2.4	FEQ2-DS4	150%	-0.45	-2.0	FEQ2-DS4	175%	-0.53	-2.1	FEQ2-DS4	175%	-0.57	-2.4
15	FEQ2-DS4	200%	-0.74	-0.4	FEQ2-DS4	250%	-0.78	-3.0	FEQ2-DS4	175%	-0.53	-2.3	FEQ2-DS4	200%	-0.67	-2.5	FEQ2-DS4	200%	-0.63	-2.4
16	FEQ2-DS4	250%	-0.91	+0.6	FEQ2-DS4	300%	-0.95	-3.4	FEQ2-DS4	200%	-0.65	+2.6	FEQ2-DS4	250%	-0.76	+2.7	RN	100%	-0.09	-
17	FEQ2-DS4	300%	-0.90	+0.6	FEQ2-DS4	350%	-1.10	+4.7	FEQ2-DS4	250%	-0.81	+3.0	FEQ2-DS4	300%	-0.94	+3.3	FEQ2-DS4	100%	-0.31	-1.6
18	FEQ2-DS4	100%	-0.32	-0.3	**FEQ2-DS4**	**400%**	**-1.28**	**+12.8**	FEQ2-DS4	300%	-0.91	-3.4	FEQ2-DS4	350%	-1.11	+5.0	FEQ2-DS4	250%	-0.86	+3.4
19	FEQ2-DS4	200%	-0.68	+0.5	RN	100%	+0.04	-	FEQ2-DS4	350%	-1.13	+4.1	RN	100%	-0.06	-	FEQ2-DS4	300%	-0.99	+3.9
20	FEQ2-DS4	300%	-1.05	+0.9	FHUIZ-DS0	100%	-0.15	+5.0	**FEQ2-DS4**	**400%**	**-1.28**	**+8.9**	FEQ2-DS4	100%	-0.30	-1.5	FEQ2-DS4	350%	-1.13	+4.8
21	FEQ2-DS4	400%	-1.18	+1.3	FEQ2-DS3	100%	-0.24	+4.9	RN	100%	-0.07	-	FEQ2-DS4	400%	-1.33	+8.5	**FEQ2-DS4**	**400%**	**-1.37**	**-113**
22	**FEQ2-DS4**	**600%**	**-1.93**	**+8.0**	**FEQ2-DS4**	**200%**	**-0.62**	**Coll.**	FHUIZ-DS0	100%	-0.15	+1.5	RN	100%	-0.07	-				
23	RN	100%	+0.08	-					FEQ2-DS3	100%	-0.25	-2.3	**FEQ2-DS4**	**500%**	**-1.71**	**Coll.**				
24	SSWx2	75%	+0.39	+3.0					FEQ2-DS4	100%	-0.33	+3.5								
25	SSWx2	200%	+0.99	+4.4					FEQ2-DS4	150%	-0.46	+5.1								
26	SSWx2	250%	+1.39	+9.0					FEQ2-DS4	200%	-0.78	-7.0								
27	RN	100%	-0.05	-					**FEQ2-DS4**	**300%**	**-0.91**	**+68**								
28	SSWx2	150%	+0.92	+7.2																
29	SSWx2	150%	+0.81	+5.4																
30	SSWx2	100%	+0.66	+5.5																
31	**SSW**	**300%**	**+1.42**	**Coll.**																

Table 3.4: Incremental dynamic test testing sequence for all specimens

3.5. Experimental results

In this section, experimental results are discussed based on the deformed shape, damage patterns, and the failure mechanism in each specimen. The deformed shape for the cracked and complete collapse is shown on the normalized scale with displacement recorded in both positive and negative displacement direction. Finally, to ease the comparison between specimens, the hysteresis behavior has been computed in terms of shear coefficient (SC) vs. the wall displacement. The experimental results of the two specimens, CS-005-RR and CS-000-RF, will be presented in this chapter. The reader can refer to the paper **?**] for the results of the dynamic shake table analysis of the other configurations.

3.5.1. Damage patterns and failure mechanisms

Due to the complexity involves in the identification of the damage during the individual test sequence, the progress of damages could not be quantified because of the change in damage location with the increasing seismic input. Hence, the detailed crack pattern is reported only at the end of the test sequence for both the first crack and just before the collapse. Also, the formation of a new crack with an increasing test sequence is reported for CS-005-RR. The image showing the damage pattern before the collapse mechanism in both specimens is also reported.

Calcium silicate wall restrained at top and bottom extremities, vertically loaded with 0.10MPa and 0.05MPa (CS-010-RR/CS-005-RR)

In the specimen CS-010-RR, under pre-compression of 0.10 MPa, the response observed remained in the elastic range for the peak table acceleration (PTA) of 0.9g and an associated MHD of 0.6mm. Because of this stiff response, the specimen was likely to fail at the table acceleration unrealistic for low-rise buildings. Hence, the overburden pressure was reduced to 0.05 MPa, and the first crack in the specimen occurred in test sequence # 22 (PTA = 1.98g, peak MHD = 8.0mm). In the first crack, two diagonal step crack originates from the upper right and left corners, meeting at the center of the main wall and continued down to meet the horizontal crack in the main wall panel (Figure 3.6a). In the test sequence # 26 (PTA = 1.39g, peak MHD = 9.0mm), a line crack appeared at the connection between the main and return wall (Figure 3.6b). Furthermore, elongation of the horizontal crack formed was in the left return wall. The crack pattern accounting for the specimen collapse was reproduced from the video for test sequence # 31 (PTA = 1.42g).

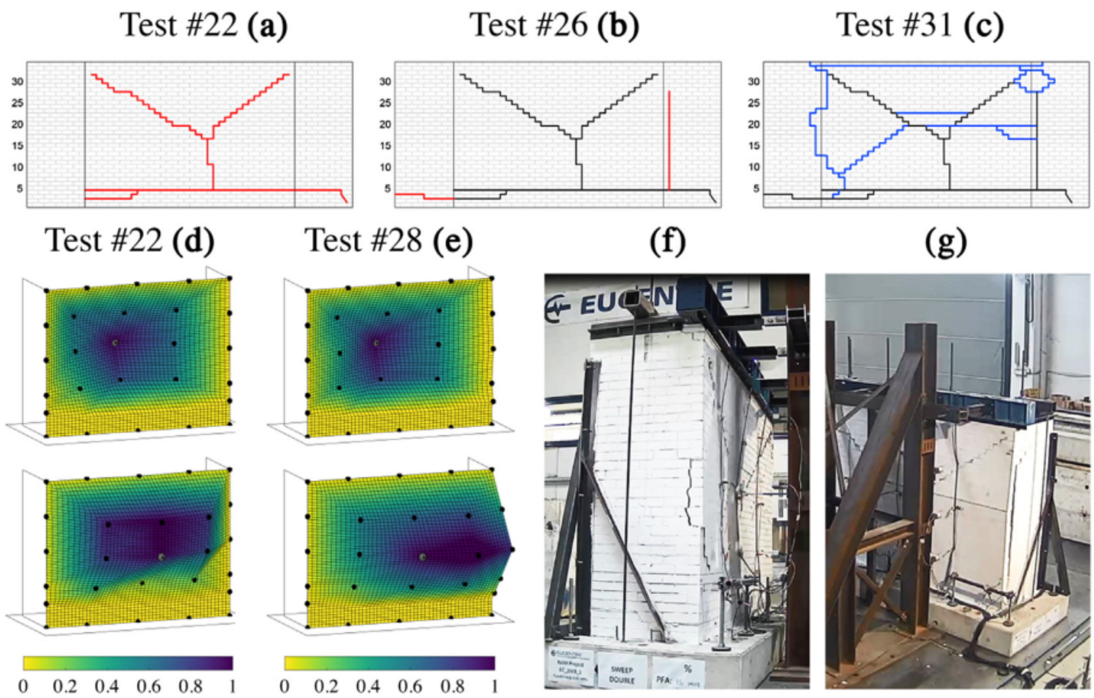

Figure 3.6: Wall restrained on four sides (CS-010-RR/CS-005-RR): Crack evolution (a, b and c); 3D deformed shape in positive (top) and negative (bottom) directions for first cracking (d) and at complete failure (e); pictures of OOP panel overturning (f and g).

Calcium silicate wall restrained at bottom and free at top, vertically loaded at the return wall with 0.05MPa (CS-000-RF)

In the specimen CS-000-RF, the pre-compression load of 0.05 MPa was applied at the top of the return wall. The first crack observed in these specimen during TS # 18 (PTA = 1.28g, peak TD = 12.8mm). The full vertical line crack was formed at the center of the main-wall and the junction of the main-wall and left pier. A small vertical line crack at the junction of the main and right pier was also observed. Furthermore, the stepped and the horizontal cracks were observed in the lower portion of the main wall (Figure 3.7a). The deformed shape is shown in Figure 3.7c, resembles similar displacement in the positive and negative direction. The specimen collapse during test sequence # 22 (PTA = 0.62g). The failure mechanism that led to the collapse of the wall was reproduced from the video shows the full development of vertical line crack along the connection of main and return wall (Figure 3.7b). Moreover, (Figure 3.7d) shows the overturning of the main wall panel along the horizontal crack. The image of the overturning of the main wall collapse is shown in Figure 3.7e and Figure 3.7f.

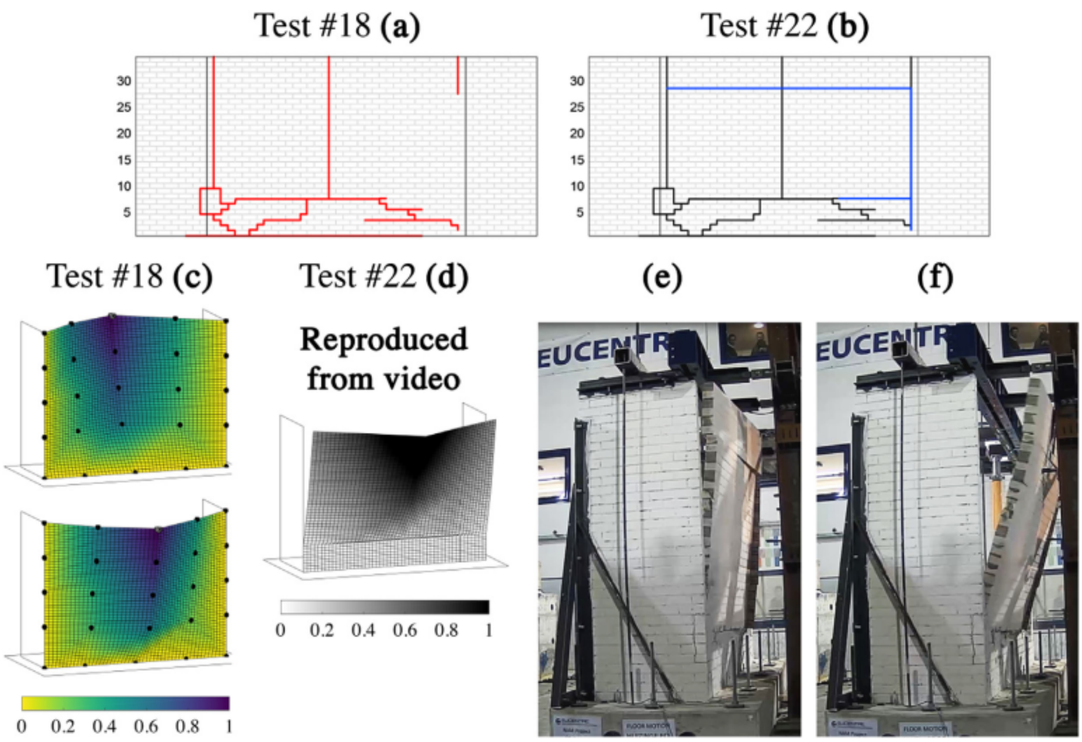

Figure 3.7: CS-000-RF: Crack evolution (a and b); 3D deformed shape in positive (top) and negative (bottom) directions for first cracking (c) and at complete failure (d); pictures of OOP panel overturning (e and f).

3.5.2. Hysteretic behaviour

The hysteretic response has been computed in terms of shear coefficient (SC) vs mid-height displacement (MHD) for specimen CS-010-RR/CS-005-RR and SC vs top displacement (TD) for CS-000-RF. The SC was calculated from the walls inertial force (V_w) using Equation 3.1.

$$SC = \frac{V_w}{m \cdot g}. \tag{3.1}$$

Where m is the mass of each specimen, and g is the acceleration due to gravity. The inertial force was computed by multiplying tributary mass with the respective acceleration recorded by the accelerometer. These tributary mass were modified throughout the testing based on the crack pattern and damage. Hence, the hysteretic response was divided into three phases, namely, pre-cracking, first cracking, and post-cracking test run. In the pre-cracking phase, no visible crack or damage was observed in the specimen. While the first crack observed in the specimen is called the first-cracking run, and often the peak strength was found in the first crack run. Referring to Table 3.4, the first crack test associated with each specimen are shown in bold. As an example, for specimen CS-010-RR Test # 1-17 are pre-cracking run associated with 0.10 MPa of pre-compression, Test # 18-21 are pre-cracking related with pre-compression of 0.05 MPa, Test # 22 is the first cracking run, and Test # 23-31 are the post-cracking test runs. The peak shear coefficient and the corresponding displacement are shown in both positive and negative displacements are shown in Figure 3.8. The maximum displacement attained at the collapse of the specimen is beyond the scale of the plot and, therefore, not shown for clarity.

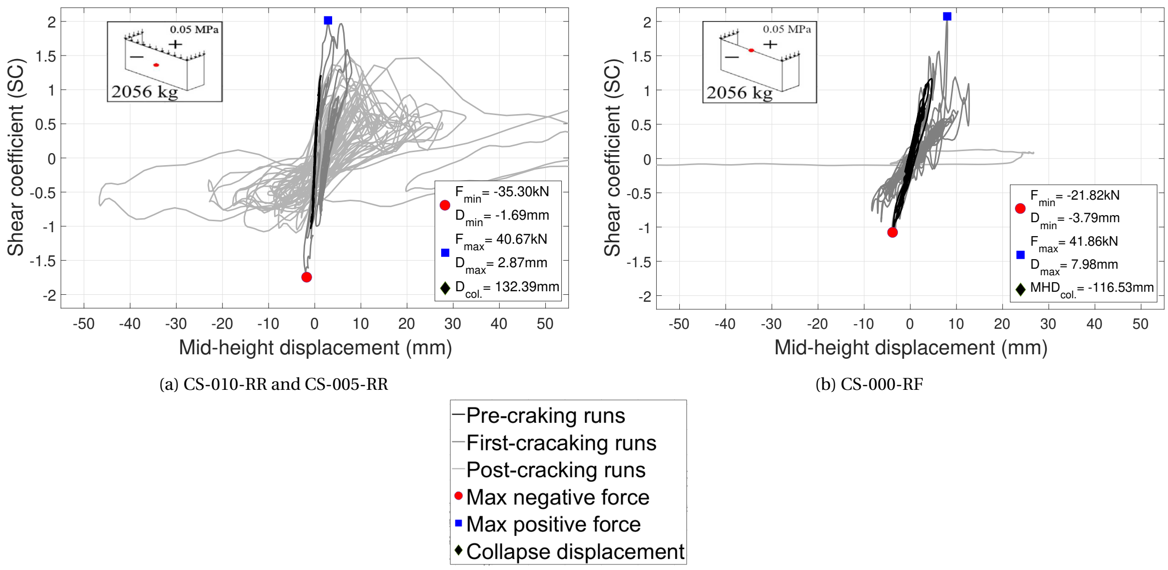

Figure 3.8: Hysteretic response of all specimen, the location of maximum shear coefficient, peak displacement in both positive and negative displacement directions are shown with circle and rectangle marker, respectively.

3.6. Conclusions

- The acceleration capacity associated with all specimens before damage was high for all the specimens. For the wall restrained at all four edges, the first crack was observed at a PTA of 1.93g. While the specimen free at the top of main-wall structural damage was observed at a PTA of 1.28g.
- Following the structural damage, the wall made of CS bricks specimen exhibited brittle behavior because of vertical line failure. As a result, a poor residual capacity was observed in the specimens.
- Following the peak strengths, the specimens shown degradation in both strength and stiffness very rapidly.
- The specimen restrained on all four edges had a higher residual capacity as compared to other specimens due to the combined action of pre-compression and horizontal restraining.

Correspondence with the author
On correspondence to the authors was made via e-mail dated 11-Oct-19 regarding the verification of top support boundary conditions. The author confirmed that crack in the top of the main wall could be formed before complete failure, which could affect the top support condition, but they did not notice this till test sequence #31. Furthermore, the deformed shape was plotted based on the interpolation of the data recorded at black dots (Figure 3.6d,e) and underlying the fact that the bottom part was not moving substantially up to the bottom crack.

InfoBox 3.1: Correspondence with the author regarding the top boundary condition.

4

Numerical modelling of specimens

Introduction

The chapter provides the overview of the finite element modelling of the experimental wall models. The finite element modelling of wall restrained on four sides with pre-compression load and wall restrained on three sides are presented in this chapter. The chapter is divided into five sections that presents the complete description of the finite element modelling setup.All analysis have been performed by using the finite element software package DIANA 10.3 [**?**]. In section 4.1 presents the mesh discretization, section 4.2 gives detail description of convergence criteria, section 4.3 gives a brief description of the constitutive law that will be used in the study. In section 4.4 details of the different the loading used is given, and identification of damping parameters are presented in the subsequent section 4.5.

4.1. Finite element modelling

Element type and properties

The finite element discretization of the physical model for all the analysis are done using 4-node quadrilateral curved shell element (Q20SH). It is based on the linear interpolation shape function with Gauss integration scheme. In the thickness direction of an element, 3-point Simpson integration scheme is used. To capture the high non-linearity in the thickness direction due to out-of-plane loading nine integration points were adopted. Each node of an element has three translations (u_ξ, u_η, & u_ζ) and two rotational degrees of freedom (ϕ_ξ, and ϕ_η) in the iso-parametric plane of an element (Figure 4.1). The stress and strain varies linearly or is constant in the plane of the element, the details are tabulated in Table 4.1.

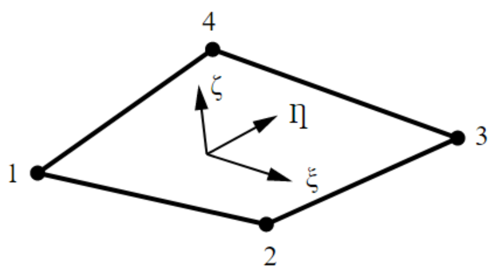

$$u_i(\xi,\eta) = a_0 + a_1\xi + a_2\eta + a_3\xi\eta$$
$$\phi_i(\xi,\eta) = b_0 + b_1\xi + b_2\eta + b_3\xi\eta$$

Figure 4.1: Q20SH: 4-node quadrilateral curved shell element and the shape function in the iso-parametric plane.

4.1.1. Four sides restrained wall with overburden of 0.10 & 0.05 MPa (CS-010-RR/CS-005-RR)

Variable	Symbols	Direction x	Direction y
Strain	ϵ_{xx}	Constant	Linear
Strain	ϵ_{yy}	Linear	Constant
Curvature	κ_{xx}	Constant	Linear
Curvature	κ_{yy}	Linear	Constant
Moment	m_{xx}	Constant	Linear
Moment	m_{yy}	Linear	Constant
Membrane force	n_{xx}	Constant	Linear
Membrane force	n_{xx}	Linear	Constant
Shear force	q_{xz}	Constant	Linear
Shear force	q_{yz}	Linear	Constant

Table 4.1: Properties of four-node shell element[**?**]

Mesh

The finite element meshing of the experimental test specimen CS-010-RR / CS-005-RR using the Q20SH element is carried out. Making use of geometry and the experimental setup, the symmetric modelling has been carried out for both static and NLTH analysis. The pre-compression load, boundary conditions, and load applied on the specimen for both full-scale and half-scale model is shown in Figure 4.2. The pre-compression load is shown using the blue line at the top edge of the main and return wall. For static analysis, the uniform face load is shown using the blue color square box on the main wall (Figure 4.2a and Figure 4.2b). In case of NLTH analysis, the application of the acceleration is shown using red arrows in **??** .

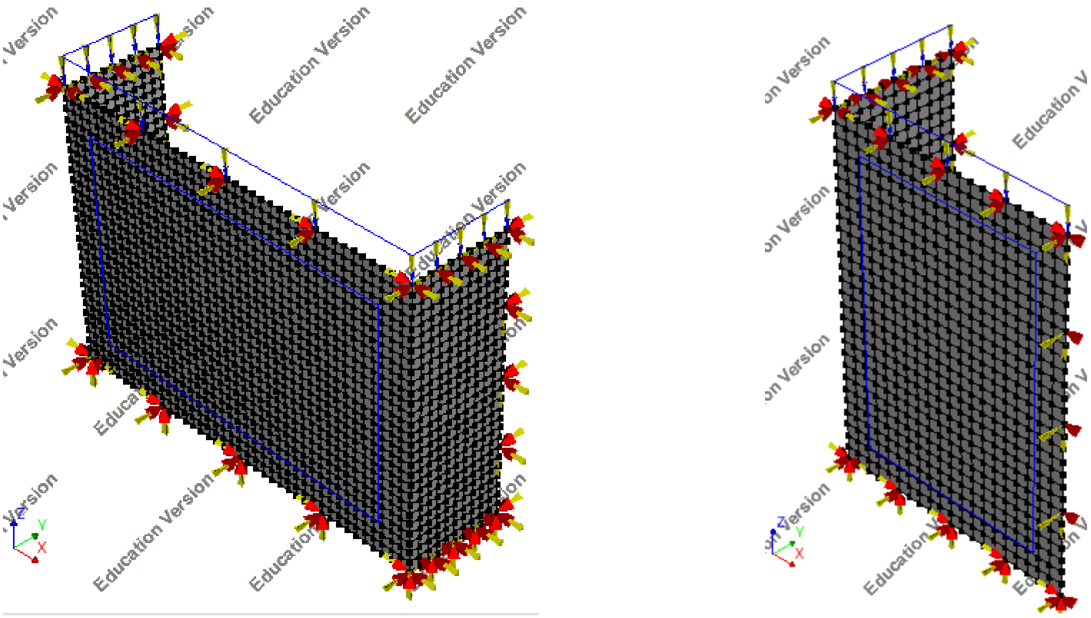

(a) Full scale

(b) Half scale

Figure 4.2: Finite element model of four sides restrained wall with overburden of 0.10MPa and 0.05MPa (CS-010-RR/CS-005-RR)

Geometry

The details of the element geometry used in meshing both full-scale and half-scale finite element model is detailed in Table 4.2.

Boundary Condition

The details of the boundary condition applied to achieve the similar support condition as that of the experimental setup is tabulated in Table 4.3. The highlighted row represent the symmetric boundary condition at the vertical edge.

Dimension	Symbol	Unit	Value
Element size	l	[m]	0.100
Thickness	t	[m]	0.102
Area	A	$[m^2]$	0.10×0.10
Total element (full-scale)	-	-	1680
Total element (half-scale)	-	-	840

Table 4.2: Element size

Location	u_X	u_Y	u_Z	ϕ_X	ϕ_Y	ϕ_Z
Main Wall Top	✓	✓	-	✓	NDoF	✓
Main Wall Bottom	✓	✓	✓	✓	NDoF	✓
Pier Bottom	✓	✓	✓	NDoF	✓	✓
Pier Top	✓	✓	-	NDoF	✓	✓
Pier Vertical	✓	✓	-	NDoF	✓	✓
Symmetry	✓	-	-	-	NDoF	✓

Table 4.3: Boundary conditions (in the global co-ordinate) for wall restrained on four sides with pre-compression load. "-"= Not restricted; "NDof"= Element do not have respective degree of freedom

4.1.2. Three sides restrained wall without overburden (CS-000-RF)

Mesh

The finite element discretization of the CS-000-RF wall model is done using Q20SH element. The primary difference with the previous specimen is the application of pre-compression and boundary condition at the top of main wall. The finite element meshing with support condition, load application for both static and NLTH analysis is shown in Figure 4.3. Additionally, symmetry in the specimen can be exploited by modelling the half of the specimen along the vertical line cut of the main wall.

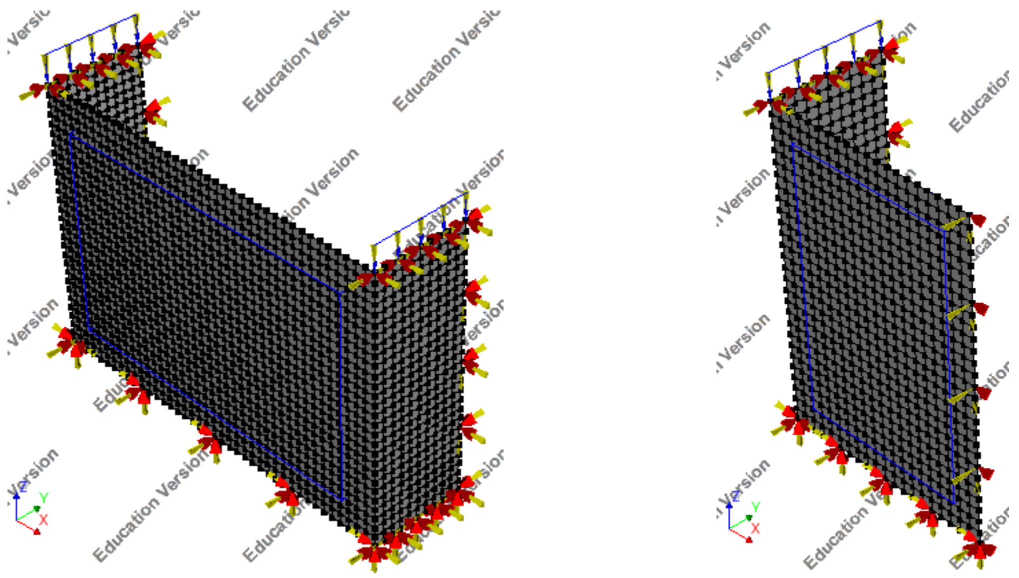

(a) Full scale (b) Half scale

Figure 4.3: Finite element model of three sides restrained wall without overburden (CS-000-RF).

Geometry

The details of the element geometry used for the discretization of the model is similar to that of previous specimen as tabulated in Table 4.2.

Boundary condition

The boundary condition at the top of the main wall is free, and hence no constraint at the top of the main wall is applied. While the boundary conditions similar to that of the previous specimen have been kept the same. The details of the degree of freedom that is applied in the global co-ordinate system are tabulated in Table 4.4.

Location	u_X	u_Y	u_Z	ϕ_X	ϕ_Y	ϕ_Z
Main Wall Bottom	✓	✓	✓	✓	NDoF	✓
Pier Bottom	✓	✓	✓	NDoF	✓	✓
Pier Top	✓	✓	-	NDoF	✓	✓
Pier Vertical	✓	✓	-	NDoF	✓	✓
Symmetry	✓	-	-	-	NDoF	✓

Table 4.4: Boundary conditions (in the global co-ordinate) for wall restrained on three sides without pre-compression load. "-"= Not restricted; "NDof"= Element do not have respective degree of freedom

4.2. Convergence method

The convergence criteria used for non-linear static, mode proportional load and cyclic analysis are tabulated in Table 4.5. The solution must satisfy all the convergence norm before move to next loading step. The default value of the tolerance is used for the analysis.

Method	Convergence norm	Tolerance
Arc length (updated normal plane)	Force	1.0×10^{-2}
	Displacement	1.0×10^{-2}
	Energy[1]	1.0×10^{-3}

[1] Using when solution methods contains line search method.

Table 4.5: Convergence criteria for non-linear static analysis.

Force and energy norm are used for NLTH analysis. Similar to the static analysis, all the norms are needed to be satisfied before moving to the next solution step. The details of the convergence criteria for NLTH analysis is tabulated in Table 4.6.Furthermore, in all the analysis the physical and geometrical non-linearity effects are considered.

Method	Convergence norm	Tolerance
Newton-Raphson (Quasi)	Force	1.0×10^{-2}
	Energy	1.0×10^{-3}

Table 4.6: Convergence criteria for non-linear time history analysis.

4.3. Material model

The following section presents the continuum damage models adopted in this study together with the definition of input parameters. The mechanical properties of the material identified in the experiment (Table 3.3) is used for the constitutive law for engineering masonry model and total strain rotating crack model.

4.3.1. Engineering masonry model (orthotropic)

In the constitutive law of engineering masonry mode (EMM), the stresses are calculated in the bed-joint (x-direction) and head-joint (y-direction) direction of the element to replicate the orthogonality of the masonry. In the present report out of available four type of head joint behaviour, head joint based on friction stress-strain in the bed-joint is chosen (HEADTP=FRICTI). Therefore, in addition to overburden load, failure in the direction normal to the bed-joint and the shear failure, cracking and crushing in the direction normal to head-joint is considered. Furthermore, the linear constitutive law (stress-strain) is changes after the initiation of the crack. After cracking, the stress-strain follows the softening law in tension, compression and shear in EMM.

Cracking

Three parameters are essential in defining the tension behaviour such as tensile strength (f_t), fracture energy in tension also known as mode-I fracture energy (G^I_{ft}), shape of softening diagram. Based on the mechanical properties of the material tensile strength is calculated from the result of the bond strength test as shown in Equation 4.1

$$f_t = \frac{f_w}{1.5}. \tag{4.1}$$

To calculate the fracture energy (Equation 4.2) the analytical expression provided by **?**] is used which is depend on the tensile strength of the material.

$$G^I_f = 0.025(2f_t)^{0.7}. \tag{4.2}$$

The shape of the tensile behaviour in EMM is linear increasing upto the tensile strength. The post-peak behaviour is defined as linear decreasing till ultimate strain is reached. The ultimate strain is defined as the strain at which no transfer of stress could occur and crack is fully open. The ultimate strain value (Equation 4.3) is dependent on the crack bandwidth 'h' of element over which crack can smeared out.

$$\varepsilon_{ult} = \frac{2G^I_{ft}}{h \cdot f_t}. \tag{4.3}$$

Based on the definition define above the constitutive law in tension for EMM is shown in Figure 4.4. Details of behaviour in tension is tabulated in Table 4.7.

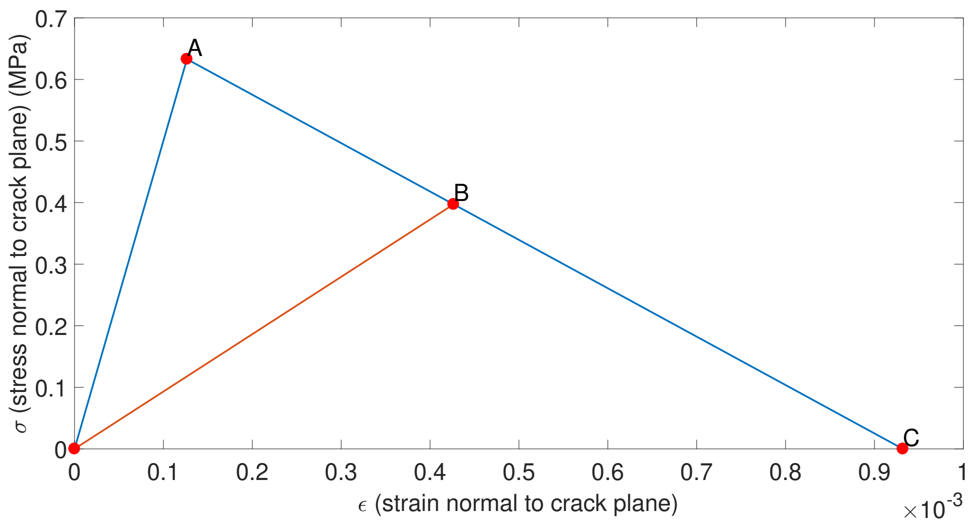

Figure 4.4: Engineering masonry model material behaviour in tension

Path / Point	Description
O-A	Linear branch of tensile behaviour
A	Tensile strength f_t of the material
A-C	Softening curve in tension
B-O	Unloading path follows the secant stiffness
O-B	Re-loading path follows the same secant stiffness to reach the last state
C	Ultimate tensile strain beyond which crack is fully open

Table 4.7: Behaviour of engineering masonry model under tension

Crushing

The compressive behaviour in masonry follows non-linear stress-strain law. Four parameters are needed to define the compressive behaviour such as Young's modulus (E), compressive strength (f_c), compressive crushing energy or mode-III fracture energy (G_{fc}^{III}) and factor n (≥ 0, determine the strain for maximum compressive strength f_c). Unlike tensile strength, compressive strength can be obtained directly from the experimental test on the masonry wallet (EN 1052-3(1998)). To find the mode-III fracture energy analytical formula is given in Equation 4.4.

$$G_{fc}^{III} = 15 + 0.43 f_c - 0.0036 f_c^2. \tag{4.4}$$

The n factor is defined as

$$n = \frac{E\varepsilon_{peak}}{f_c}. \tag{4.5}$$

The shape of the compressive curve is assumed to be the third order curve, parabolic up to the peak compressive strength then linear softening curve up to the residual stress of 10% of the compressive strength is reached. The unloading behaviour follows the initial stiffness upto the compressive stress level of $\lambda\sigma_{rf,compressive}$ and then with secant stiffness upto the origin. The λ defined as unloading factor varies between 0 and 1 such as

- $\lambda = 0$: unloading with linear stiffness.
- $\lambda = 1$: unloading with secant stiffness.

The reloading follows the linear path with secant stiffness E_{sec} upto the last load extreme point (α_{comp},$\sigma_{rf,compressive}$). E_{sec} is given as:

$$E_{sec} = \frac{\lambda\sigma_{rf,compressive}}{\alpha_{comp} - \lambda\frac{\sigma_{rf,compressive}}{E}} \tag{4.6}$$

The ultimate strain (ε_{ult}≥0)at which no compressive stress can be transfer is given as

$$\varepsilon_{ult} = \varepsilon_{peak} + max\left[0, \frac{2G}{hf_c} - \frac{f_c}{A^2E} - \frac{A+1}{A}\left(\varepsilon_{peak} - \frac{f_c}{E}\right)\right]. \tag{4.7}$$

where h is the crack bandwidth of the element and A is define as

$$A = \left(\frac{E\varepsilon_{peak}}{f_c}\right)^{0.5}. \tag{4.8}$$

The compressive curve in masonry is given in Figure 4.5, and details are tabulated in Table 4.8

Path/Point	Description
O-A-B	Parabolic compression curve with no crushing and cracking
B	Compressive strength of the masonry
B-C	Softening branch upto the ultimate strain
C-D-E	Unloading branch follows based on compressive model
E-C	Re-loading branch followed the straight path to the last loading extreme

Table 4.8: Behaviour of engineering masonry model under compression

Shearing

In the plane of the element, shear stress τ is defined by the shear strain γ and the stress normal to the bed joint σ_{yy}. The initial shear stiffness (G) is relating the shear stress and shear strain upto maximum shear strain τ_{max}. The maximum shear stress is based on the Coulomb friction criterion as:

$$\tau_{max} = max[0, c - \sigma_{yy} tan(\phi)]. \tag{4.9}$$

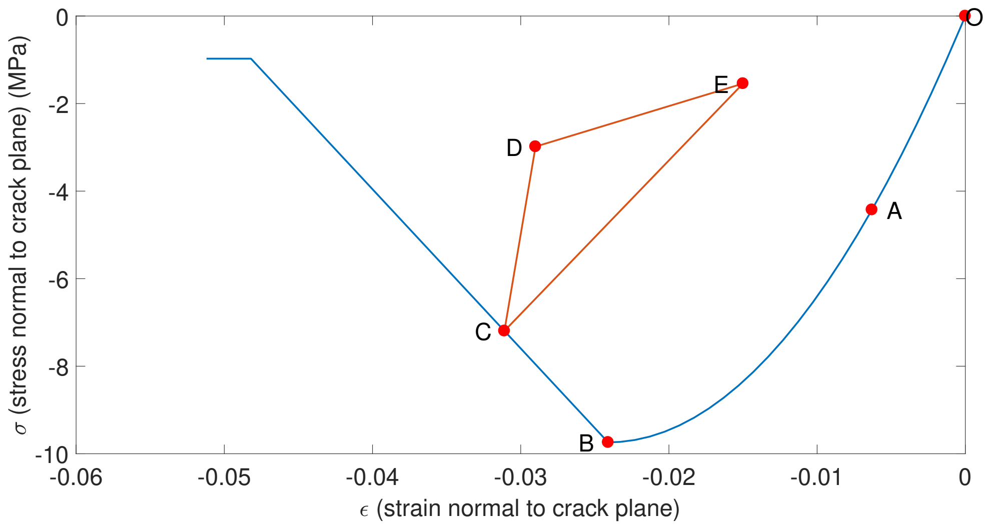

Figure 4.5: Engineering masonry model material behaviour in tension

where, c is the cohesion and ϕ is the friction angle. If the fracture energy in shear or mode-II fracture energy (G_{fs}^{II}) is specified by the user, upon reaching the maximum shear stress the cohesion decreases linearly to zero at total shear strain γ_{ult}.

$$\gamma_{ult} = \frac{2G_{fs}^{II}}{n \cdot c} - \frac{c}{G}. \tag{4.10}$$

Where, h is the crack bandwidth of the element. The behaviour in shear is shown in Figure 4.6 with details are tabulated in Table 4.9. If no fracture energy in shear has been specified, in shear elasto-plastic model has been followed instead. At the cracking of the integration point the cohesion is immediately reduced to zero. In the out-of-plane direction of the element shear stress in the bedding plane is checked with the Coulomb friction criterion.

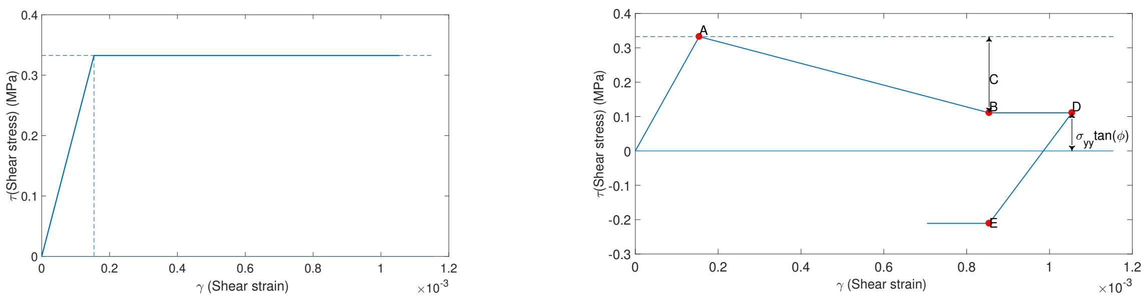

(a) Elasto-plastic (for static and dynamic analysis.)

(b) Shear softening (for cyclic analysis.)

Figure 4.6: Engineering masonry model material behaviour in shear.

Path/Point	Description
O-A	Linear branch of the shear behaviour
A-B	Cohesion softening
B-D	Shear with
C-D-E	Unloading branch follows based on compressive model
E-C	Re-loading branch followed the straight path to the last loading extreme

Table 4.9: Behaviour of engineering masonry model in shear

Based on the above discussion for the different material properties, the Table 4.10 gives the value of the necessary parameters needed in defining the behaviour in finite element software.

Parameter	Symbol	Unit	Value
Tensile strength (bed-joint)	f_t	MPa	0.633
Mode-I fracture energy	G_f^I	N/mm	0.0295
Ultimate strain in tension	ε_{ult}	-	9.32×10^{-4}
Mode-III fracture energy	G_f^{III}	N/mm	18.85

Table 4.10: Parameters for defining the material behaviour in the finite element analysis.

4.3.2. Total strain rotating crack model (isotropic)

Total Strain Rotating Crack (TSRC) model initially assume the material to be isotropic. After cracking in the element the constitutive law changes to orthogonal constitutive law in the direction parallel to crack and perpendicular to crack. In tension: based on fracture energy out of six different softening curves can be chose from. In the following report linear softening behaviour similar to EMM will be used. Similar to tension, there are sixteen predefined compression curves and 7 predefined shear stress reduction models are available. But the unloading and reloading behaviour in TSRC is based on secant stiffness which is not representative of masonry.

Compression

Out of the 16 pre-defined compressive function the parabolic curve will be used for the following study also to make the qualitative comparison between the EMM and TSRC model. The parabolic curve in the DIANA formulated based on the fracture energy. Three parameters are needed for describing the parabolic curve in compression are, (1) strain at one-third $\alpha_{c/3}$ of the maximum compressive strength f_c; (2) strain α_C at peak compressive stress; and (3) ultimate strain α_u

$$\alpha_{c/3} = -\frac{1}{3}\frac{f_c}{E}. \tag{4.11}$$

$$\alpha_c = -\frac{5}{3}\frac{f_c}{E} = 5\alpha_{c/3}. \tag{4.12}$$

$$\alpha_u = min\left(\alpha_c - \frac{3}{2}\frac{G_{fc}^{III}}{hf_c}, 2.5\alpha_c\right) \tag{4.13}$$

The behaviour in tension and compression under loading and unloading is shown in Figure 4.7.

Shearing

Shear behaviour is only specified in case of fixed crack concept and for combined rotating to fixed crack concept where shear stiffness is reduced after cracking. The stiffness reduction is based on shear retention factor. Shear retention based on the damage due to cracking will be used. In this, the opening in the cracked direction does not lead to contraction in the direction perpendicular to the crack.

4.4. Loading conditions

In the following section, loading scheme will be presented in detail. The four different loading schemes are considered for the following analysis such as:

- Non-linear static analysis with uniform loading: the wall subjected to uniform incremental load.
- Non-linear static analysis with mode proportional loading: the wall subjected to incremental load proportional to first mode shape.
- Non-linear time history analysis: the wall subjected to applied base acceleration.
- Non-linear cyclic analysis: the wall subjected to cyclic load defined on the basis of maximum base shear force obtained during dynamic test.

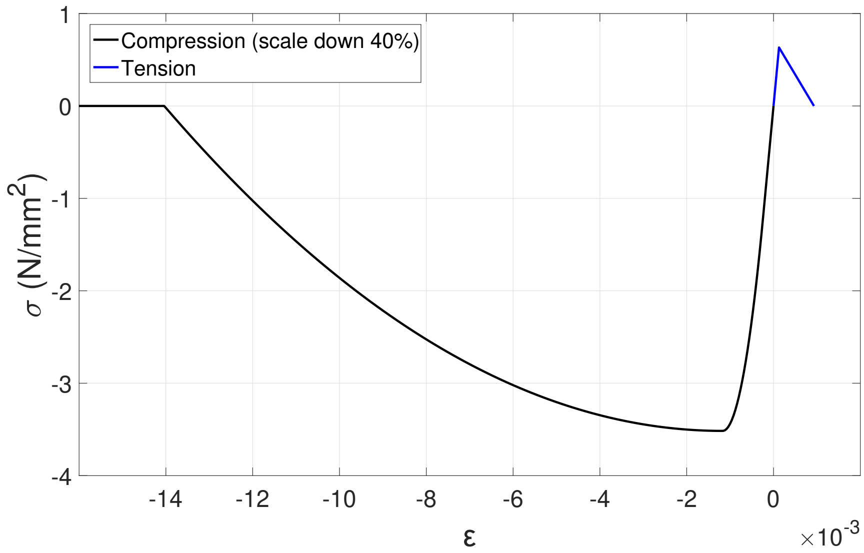

Figure 4.7: Total strain crack model in compression and tension.

4.4.1. Non-linear static analysis (Uniform loading)

As detailed in the Table 3.4, the pre-compression load on the specimen is changed after test sequence (TS) # 17. In the non-linear static analysis the pre-compression upto the maximum mid-height displacement (MHD) corresponds to TS # 17 was kept 0.10 MPa and then changed to 0.05 MPa for the remaining analysis. The pre-compression load was applied as equivalent line load by multiplying with wall width (102mm) as 0.10×102=10.2 N/mm. The uniform load applied on the main wall in the out of plane direction (Push load) toward the pier notated as positive displacement direction. Details of the load step and direction of application are detailed in Table 4.11. Separate analysis was carried out when main wall was loaded away from the pier in the out-of-plane direction is indicated as negative displacement direction.

Phase	Type of load	Location of application	Step size / No. of step	Direction
1	Self-weight	-	1(1)	-Z
2	Pre-compression	Main and pier wall top	10.200 N/mm(1)	-Z
3	Push load	Outer face of main wall	5×10^{-5} MPa (36)	+Y
4	Pre-compression	Main and pier wall top	5.100 N/mm(1)	-Z
5	Push load	Outer face of main wall	Varying[1]	+Y

[1] The both step size and no. of steps varied to obtain converge solution.

Table 4.11: Details of load application for non-linear static analysis with uniform loading.

The load scheme for the non-linear static analysis used for the calcium silicate wall with free support at the top is tabulated in Table 4.12. The pre-compression applied only at the top of the return wall. Step size and no. of steps are changed with analysis to get the converge solution.

Phase	Type of load	Location of application	Step size (No. of step)	Direction
1	Self-weight	-	-(1)	-Z
2	Pre-compression	Pier wall top	5.100 N/mm (1)	-Z
3	Push load	Outer face of main wall	Varying[2]	+Y

[2] The both step size and no. of steps varied to obtain converge solution.

Table 4.12: Details of load application for non-linear static analysis

4.4.2. Non-linear static analysis (Mode proportional loading)

The application of the out-of-plane load on the main wall is based on the first mode shape of the structure. The first mode-shape is found using the eigenvalue analysis of the specimen as discussed in the **??**. Similar to the static analysis, for test specimen CS-010-RR/CS-005-RR, a phased analysis was conducted by decreasing the overburden once mid-height displacement of 0.60 mm was reached.

4.4.3. Non-linear time history analysis

The input signal used for the non-linear time history analysis in FE analysis consists of parts of total input motion (Figure 3.4, and Table 3.4) where the majority of the damage in the experiment was observed. The time signal of the input motion and maximum peak table acceleration (PTA) is expressed in terms of gravitational acceleration (g).

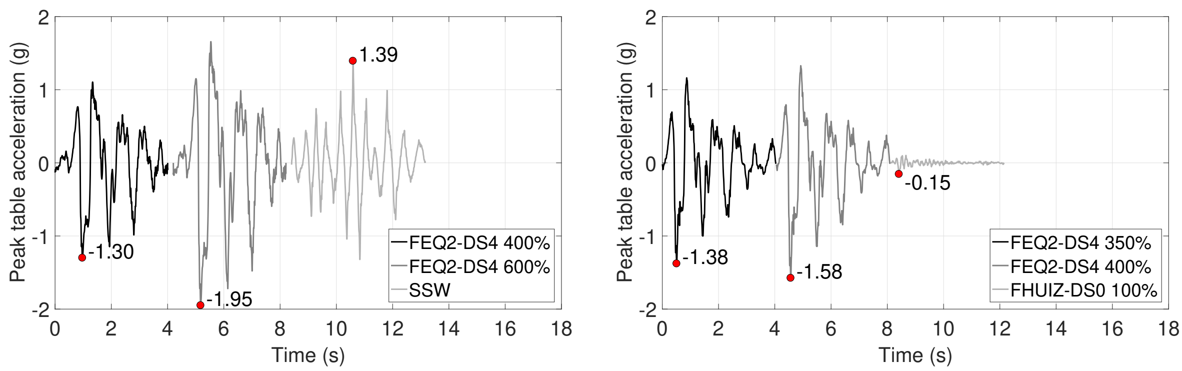

(a) Acceleration time history input for CS-005-RR

(b) Acceleration time history input for CS-000-RF

Figure 4.8: Acceleration time history used for the input motion in the non-linear time history analysis.

4.4.4. Non-linear cyclic analysis

In the cyclic analysis, the uniform load applied on the main wall is varied in the cyclic manner i.e. force in both positive and negative displacement direction. For the cyclic analysis the pre-compression load of 0.05 MPa was applied and uniform load with a step size of 2×10^{-5}. The pre-compression on the wall restrained on four sides did not changed as in the case of static analysis because in the experiment damage in wall occurred at the pre-compression of 0.05 MPa.The applied peak load on the main wall is scaled between 60% to 180% of the peak force in the positive and negative direction from Figure 3.8 respectively. This scaling is chosen to fully cover the pre-crack to post-crack behaviour in the both the walls. The details of the cyclic loading scheme are shown in Figure 4.9a and Figure 4.9b for wall restrained on four sides with pre-compression and wall restrained on three sides without pre-compression load respectively.

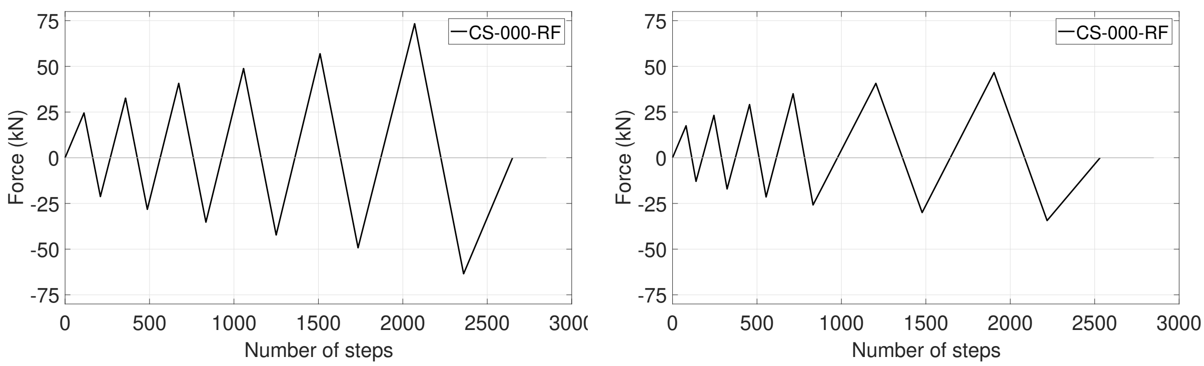

(a) Cyclic load scheme for CS-005-RR

(b) Cyclic load scheme for CS-000-RF

Figure 4.9: Details of the complete cyclic load history.

4.5. Determination of Rayleigh damping parameter based on eigenvalue analysis

The Rayleigh damping parameters to be used in the non-linear time history analysis are identified through eigenvalue analysis. The parameters namely, eigenfrequency, eigenmode, and effective mass percentage are identified. The frequency corresponding the mode that contributes most in terms of effective mass percentage (out of first 10 modes) in the direction of out-of-plane is used for calculating Rayleigh damping parameter. Mass(a) and stiffness(b) proportional damping coefficient are calculated for 2% damping ratio (ξ). Natural frequency and effective mass percentage for the wall restrained on four sides (CS-010-RR/CS-005-RR) are given in Table 4.13.

Natural frequency and effective mass percentage for test specimen CS-010-RR/CS-005-RR are given in Table 4.13. The first 4 mode shapes of the analysis are shown in Figure 4.10.

Mode	Frequency [Hz]	X-direction		Y-direction		Z-direction	
		Eff. mass %	Cum. mass %	Eff. mass %	Cum. mass %	Eff. mass %	Cum. mass %
1	25.23	0.00	0.00	35.21	35.21	0.00	0.00
2	34.07	0.07	0.07	0.00	35.21	0.00	0.00
3	50.40	0.00	0.07	5.56	40.77	0.00	0.00
4	64.57	0.00	0.07	0.00	40.77	0.00	0.00
5	72.45	0.00	0.07	0.00	40.77	0.00	0.00
6	73.39	1.32	1.39	0.00	40.77	0.00	0.00
7	86.67	0.00	1.39	0.00	40.77	0.00	0.00
8	97.91	0.00	1.39	0.91	41.69	0.00	0.00
9	107.13	31.00	32.39	0.00	41.69	0.00	0.00
10	107.25	2.29	34.68	0.00	41.69	0.00	0.00

Table 4.13: Wall restrained on four sides: outcomes of eignevalue in terms of natural frequencies, effective mass and cumulative mass percentage

The calculation of the Rayleigh damping parameter are given below

$$\begin{bmatrix} a \\ b \end{bmatrix} = \frac{2\xi}{\omega_i + \omega_j} \begin{bmatrix} \omega_i \omega_j \\ 1 \end{bmatrix} \tag{4.14}$$

Where, ω_i and ω_j are the frequencies with respective to the selected vibration modes. The proportional damping coefficients are calculated using the frequencies highlighted in Table 4.13 as

$$\begin{bmatrix} a \\ b \end{bmatrix} = \begin{bmatrix} 4.225 \\ 8.418 \times 10^{-5}. \end{bmatrix}$$

Natural frequency, effective mass percentage for test specimen CS-000-RF is given in Table 4.14. The first 4 mode shape of the analysis are shown in Figure 4.11.

The Rayleigh damping parameters is calculated for mode 1 and mode 3 using Equation 4.14, the proportional damping coefficients are calculated using the frequencies highlighted in Table 4.14 as

$$\begin{bmatrix} a \\ b \end{bmatrix} = \begin{bmatrix} 1.772 \\ 1.733 \times 10^{-4}. \end{bmatrix}$$

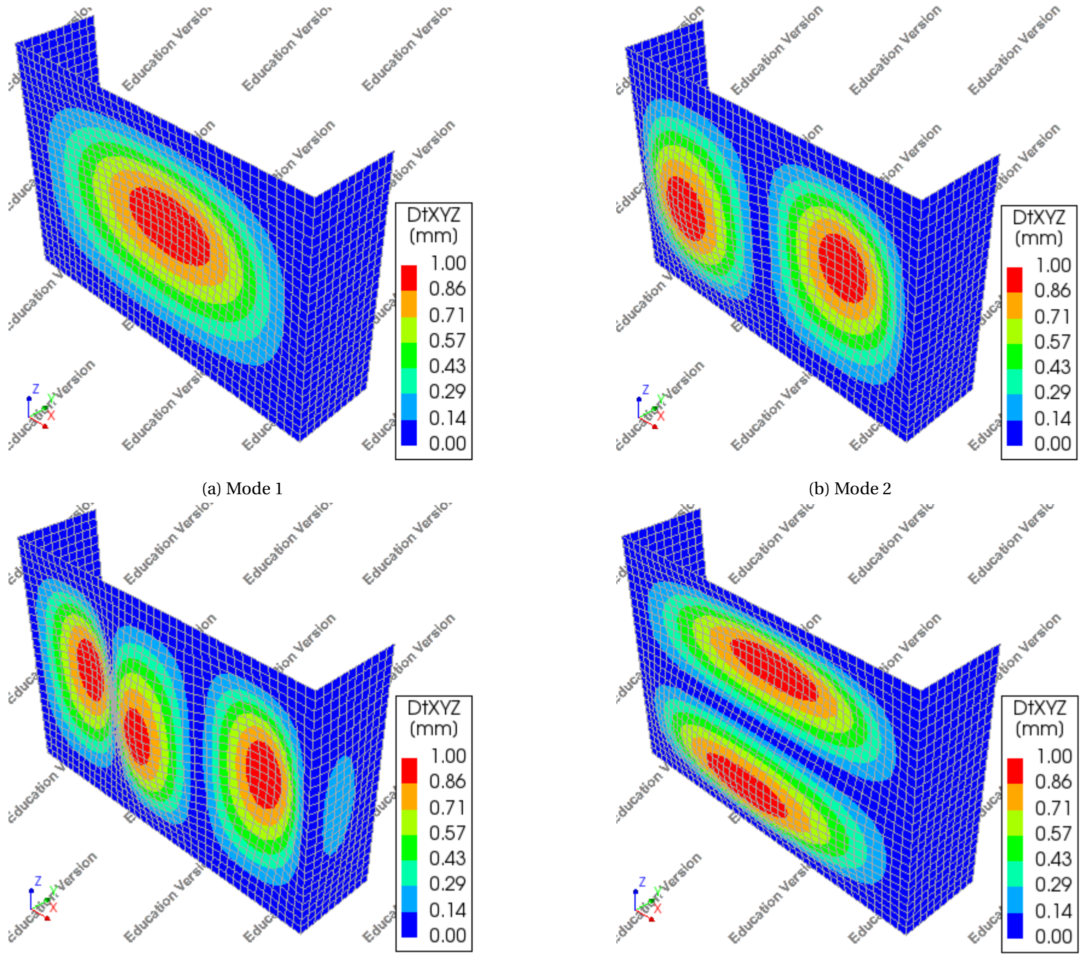

(a) Mode 1 (b) Mode 2

(c) Mode 3 (d) Mode 4

Figure 4.10: First four mode shapes based on eigenvalue analysis for four sides restrained wall. Absolute deformation scale=250

Mode	Frequency [Hz]	X-direction		Y-direction		Z-direction	
		Eff. mass %	Cum. mass %	Eff. mass %	Cum. mass %	Eff. mass %	Cum. mass %
1	9.56	0.00	0.00	32.46	32.46	0.00	0.00
2	22.17	0.00	0.00	0.00	32.46	0.00	0.00
3	27.35	0.00	0.00	7.79	40.25	0.00	0.00
4	40.20	0.06	0.06	0.00	40.25	0.00	0.00
5	41.24	0.00	0.06	6.17	46.42	0.00	0.00
6	59.23	0.00	0.06	0.62	47.04	0.00	0.00
7	66.20	0.00	0.06	3.19	50.23	0.00	0.00
8	66.33	0.21	0.27	0.00	50.23	0.00	0.00
9	77.47	0.00	0.28	0.00	50.23	0.00	0.00
10	83.40	11.66	11.94	0.00	50.23	0.00	0.00

Table 4.14: Wall restrained on three sides: outcomes of eignevalue in terms of natural frequencies, effective mass and cumulative mass percentage.

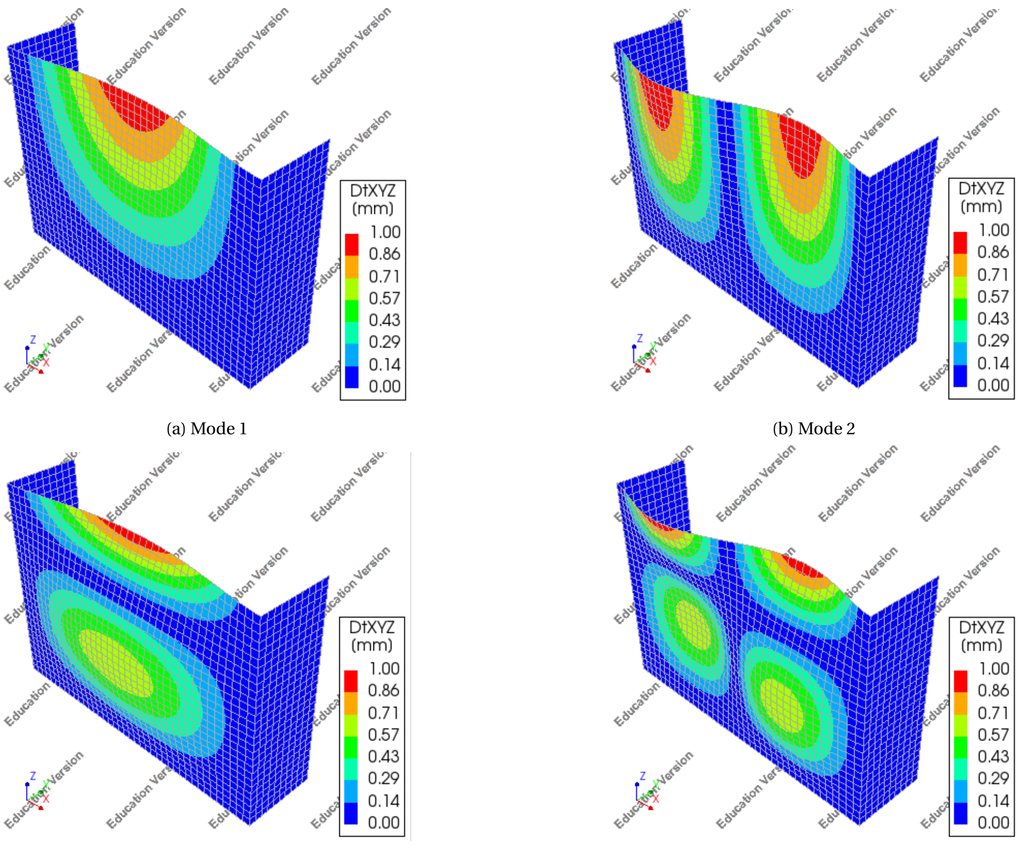

(a) Mode 1

(b) Mode 2

(c) Mode 3

(d) Mode 4

Figure 4.11: First four mode shapes based on eigenvalue analysis for three sides restrained wall. Absolute deformation scale=250.

5

Numerical results

Introduction

In the following chapter, the results of the numerical analysis performed are presented. Four distinct types of analysis are carried out to present the behavior of the URM wall subjected to out-of-plane loading. The following chapter is divided into four sections. The analysis results are elaborated in terms of force-displacement curves, and the crack patterns are shown in terms of principal strain contour plots. In the section 5.1, the result of the non-linear static analysis is presented. Furthermore, the influence of the boundary condition on the crack pattern is shown using the deformed shape. In section 5.2 results of the non-linear static analysis with mode proportional loading, section 5.3 results of the non-linear time history analysis, and section 5.4 results of the cyclic analysis is presented for both the wall.

Post-processing and results

To facilitate the comparison between different material models, the force-displacement curve has been computed in terms of shear coefficient (SC) vs. mid-height displacement (MHD) for wall restrained on four sides with overburden (CS-010-RR/CS-005-RR), and SC vs. top-displacement (TD) for wall restrained on three sides without overburden (CS-000-RF) specimen. The shear coefficient is calculated from the base shear force as given below:

$$SC = \frac{V_b}{m \cdot g} \tag{5.1}$$

Where V_b is the base shear force, or the support reaction force obtain from the numerical analysis, 'm' is the mass of the specimen, and 'g' is gravitational acceleration. The legend used for the principal strain plots corresponds to the tension softening behavior, as shown in Figure 5.1. The peak strain and ultimate strain are calculated as:

$$\epsilon_{peak} = \frac{f_t}{E} = \frac{0.633}{5005} = 1.26 \times 10^{-4},$$
$$\epsilon_{ult} = \frac{2G_{ft}}{hf_t} = \frac{2 \times 0.0295}{100 \times 0.633} = 9.32 \times 10^{-4}.$$

5.1. Non-linear static analysis (Uniform loading)

5.1.1. Wall restrained on four sides

The outcomes of the non-linear static analysis adopting the two material models for the four sides restrained wall with top overburden load is shown in Figure 5.2. The initial stiffness of EMM and TSRC are computed using the linear trend of the hysteretic curve of the experimental TS# 17 and are within 10% difference that of the experiment. Representative load levels are selected to show the crack patterns in terms of maximum

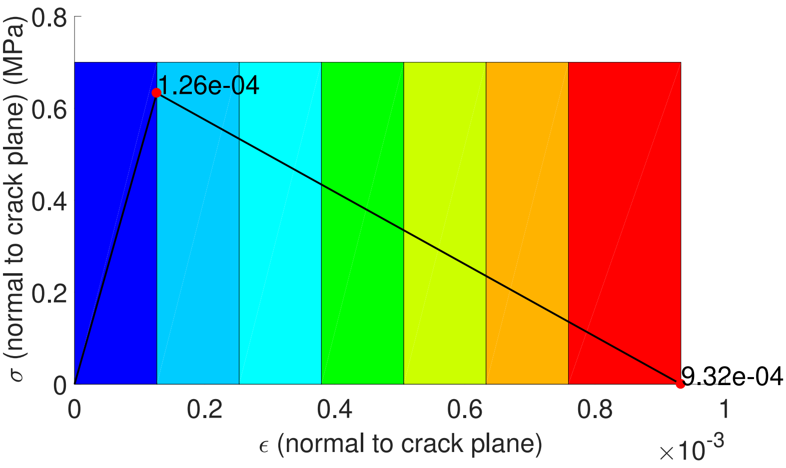

Figure 5.1: Legend for principal strain plot.

principal strains. The nomenclature is chosen, for example, for point E1p, 'E' refer for engineering masonry model, '1' for the sequence, and 'p' for positive displacement direction. While in T1n, 'T' refers to the total strain rotating crack model, '1' for the sequence, and 'n' for negative displacement direction. The *maximum principal strain* means the maximum strain computed in all the nine layers, i.e., over the thickness of the wall, is shown in one contour plot.

The plot of the maximum principal strain for indicated load levels is provided in Figure 5.3 for positive and negative displacement direction for the engineering masonry model. Each drop in the shear coefficients corresponds to the formation of a new crack in the numerical model that eventually leads to a decrease in load-carrying capacity.

IIn the non-linear analysis in the positive displacement direction, i.e., the load is applied on the main wall towards the pier, at point 'E1p', i.e., the first drop in the SC, and also the onset of cracking in the wall has started. The crack along the top and bottom edge of the main wall starts to form at the load level of 35.16kN (Figure 5.3b). The horizontal crack propagates along the length of the wall in the inner face (tension side) of the main-wall, and vertical cracks at the connection between main wall and pier start to form (E2p) together with the diagonal cracks at the outer face i.e., compression side (Figure 5.3c). With further increase in the load, cracks along the main-wall and pier connection are formed (E3p to E4p). After the load level E4p, the numerical model shows significant displacement with a minor increase in load-carrying capacity, as seen in Figure 5.2d, e. The maximum force capacity is found to be 69.38kN (Peakp) for mid-height displacement of 19.42mm. Furthermore, the crack pattern observed is not similar to the crack pattern based on the boundary conditions as given in section 2.1. Whereas, the force-displacement curve can be idealized into a tri-linear curve, as stated in literature Figure 2.11. The dashed line in the analysis is due to the non-converge solution i.e., the norm specified for the solution is not satisfied. In the convergence study, it was found that, on increasing the tolerance to 0.10 from a default value of 0.01, the solution obtained can be reliable but having a higher tolerance value.

In the non-linear static analysis in the negative direction, i.e., the load applied on the main wall in the direction away from the pier, the initiation of cracks started at the top and bottom support together with at the connection between main wall and pier as shown in Figure 5.3g. Following this, non-convergence in the analysis observes with a noticeable decrease in SC; after that, it remains constant before the termination of analysis. Figure 5.3h shows maximum strain in the top, and bottom support has been reached, with the initiation of diagonal cracking in the main-wall and at the connection between the main-wall and pier.

The result of the non-linear static analysis with total strain rotating crack model (TSRC), which is isotropic i.e., identical stiffness and strength property in all the direction. Because of this difference, the initial stiffness of the TSRC material model is more compared to the EMM (shown in the inset of Figure 5.2). The initiation of the crack is similar to the EMM, i.e., at the top and bottom of the main wall, as shown in Figure 5.4b (T1p). The peak shear coefficient is attained at relatively lower MHD (Peakp) as compared to EMM with the progress of crack along the edges of the main wall (Peakp to T2p), as shown in Figure 5.4c, d. Following T2p, the shear coefficient rapidly drops (to T3p) with a slight increase in MHD (3.45mm to 3.91mm). This drop is

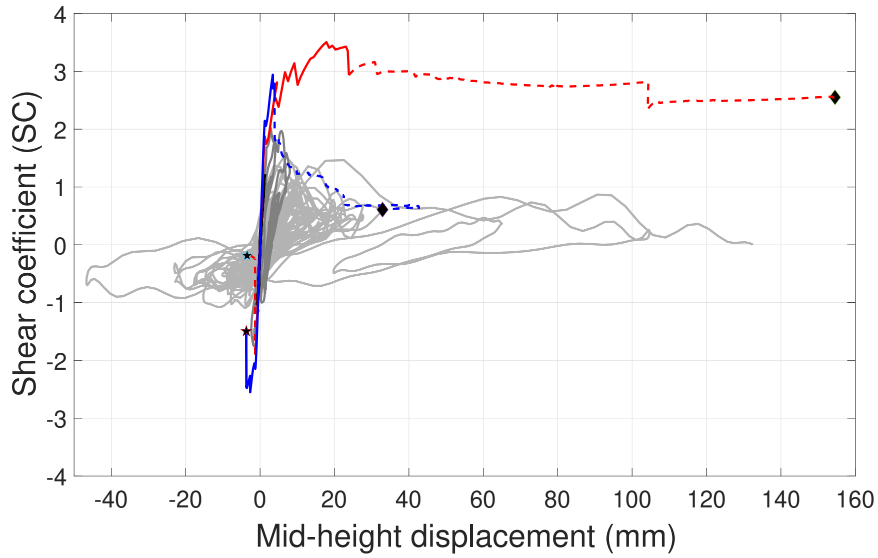

(a) Full response of numerical analysis compared with experiment

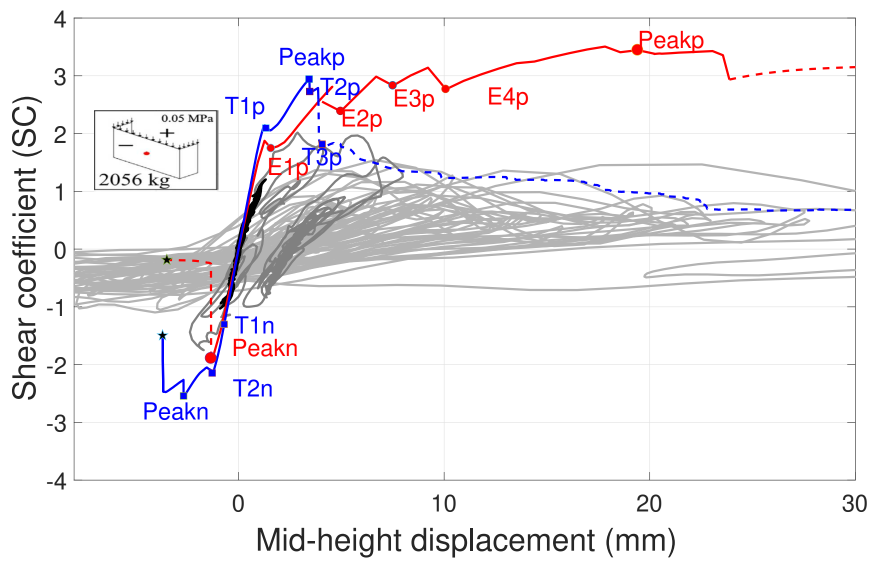

(b) Details of load levels

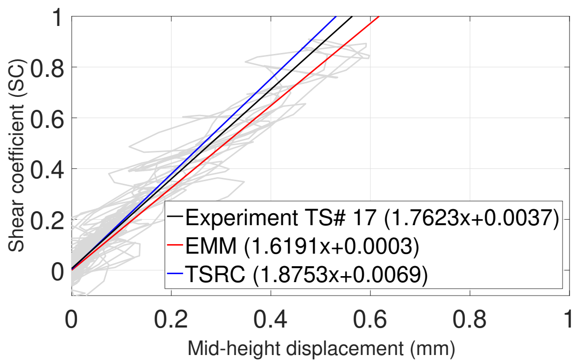

(c) initial stiffness

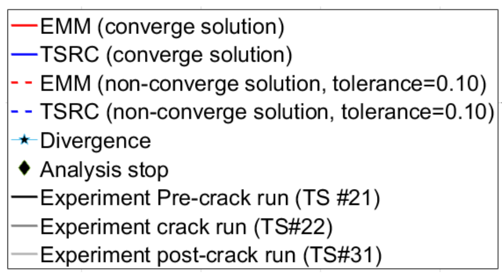

(d) Legend details.

Figure 5.2: Shear coefficient vs mid-height displacement curve for four sides restrained wall (CS-010-RR/CS-005-RR) comparing engineering masonry model (EMM) and total strain rotating crack model (TSRC).

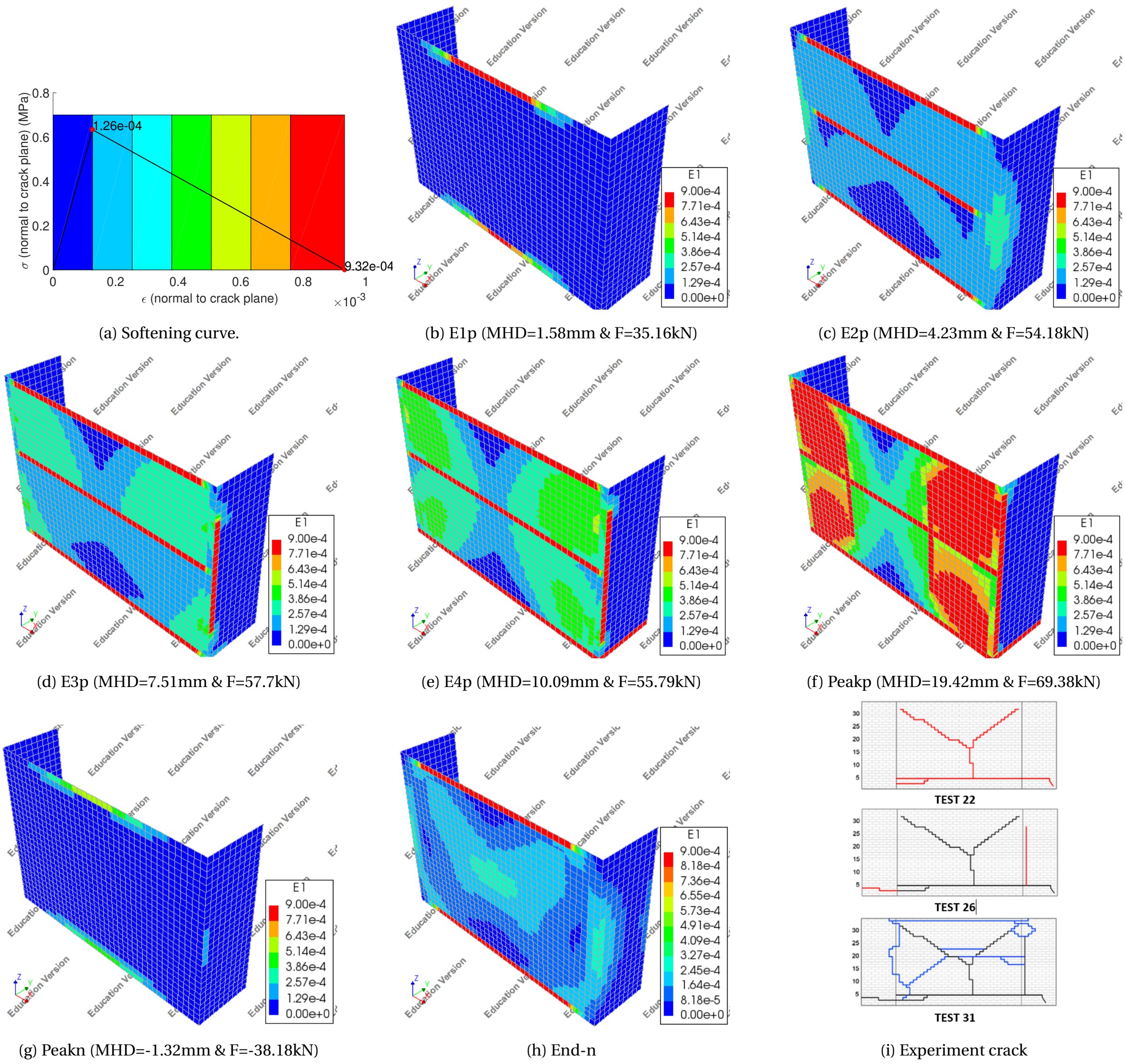

Figure 5.3: Four sides restrained wall (EMM): Maximum principal strain at different load level as specified in Figure 5.2.

followed by a fully formed diagonal crack in the main wall, as shown in Figure 5.4e. Furthermore, the force-displacement curve using the TSRC material model is no longer replicating the trilinear force-displacement curve as specified in the literature (section 2.1). The crack pattern observes in the following analysis is similar to one suggested in the literature (Figure 2.8) with restrained support condition at four edges and matching with the experimental results at failure shown in Figure 5.4i (Test 31).

Applying the load in the negative direction (away from pier), the response observed is similar to the case when the load is applied the positive direction up to point 'T1n'. The cracks in the top and bottom of the main wall are seen in the Figure 5.4f,g. As the analysis progress, the complete softening at the junction of the main-wall and pier initiated rapidly for a minor increase in MHD from 2.67 to 2.68mm (Figure 5.4c) and analysis diverges with ultimate strain in all the four edges along with softening in the middle horizontal of the main wall Figure 5.4d.

The advantage of symmetry in the model is utilized for the following numerical analyses. The comparison between the full scale and half-scale model is presented in Figure 5.5 for four sides restrained wall. The analysis was done to verify the initial stiffness, overall trend, and peak shear coefficient estimation. The analysis stops at the mid-height displacement of 29mm just after five-step of non-convergence. Knowing the symmetry in the model verify the above criteria, and the analysis did not run further.

The crack pattern listed in the literature based on boundary condition is significantly different from that

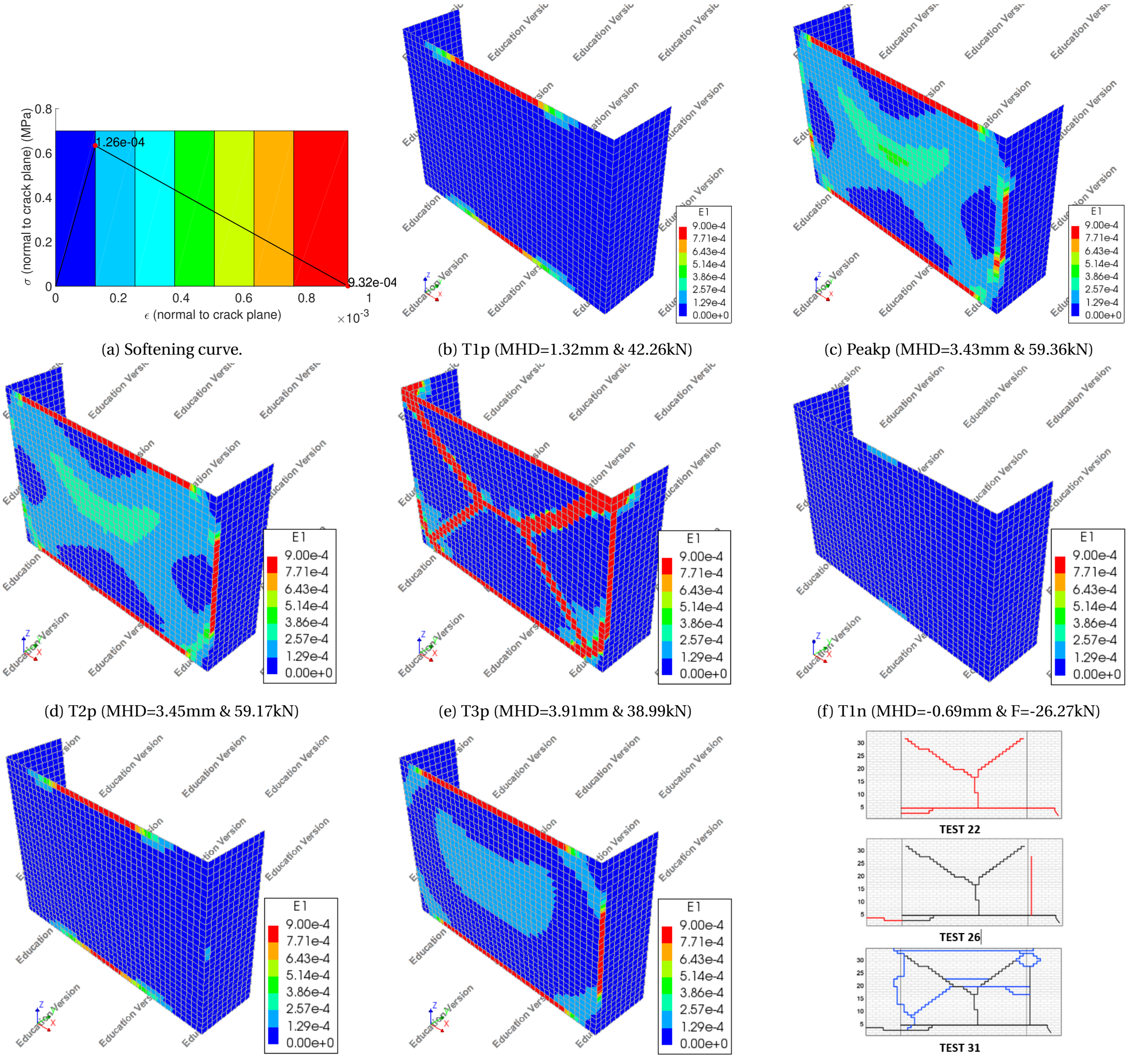

(a) Softening curve.
(b) T1p (MHD=1.32mm & 42.26kN)
(c) Peakp (MHD=3.43mm & 59.36kN)
(d) T2p (MHD=3.45mm & 59.17kN)
(e) T3p (MHD=3.91mm & 38.99kN)
(f) T1n (MHD=-0.69mm & F=-26.27kN)
(g) T2n(MHD=-1.28mm & F=-43.28kN)
(h) Peakn (MHD=-2.68mm & F=-51.47kN)
(i) Experiment crack

Figure 5.4: Four sides restrained wall (TSRC): Maximum principal strain at different load level as specified in Figure 5.2.

of experiment and numerical analysis. The two primary reasons are identified for these differences. (1) The top support condition effect on crack initiation and propagation in the wall based on the literature for two-way support wall Figure 2.8. (2) The diagonal cracks have higher tensile strength and fracture energy [**?**], hence required a higher load to open a diagonal crack and can dissipate higher energy on cracking.

Firstly, the effect of boundary condition study was carried out based on the deformed shape of the wall. The 3-D deformed shape of the wall at the maximum displacement of the first crack run is given in Figure 5.6a. This deformed shape is not concurrent with the deformed surface plot of the numerical analysis (Figure 5.6b) applying similar support conditions as specified in the experiment. Therefore, on changing the boundary condition by allowing the wall to rotate along with the top horizontal support, the deformed shape (Figure 5.6c) shows the peak displacement is shifted in the top and resembles similarity with the experiment.

The response of the non-linear static analysis with changed boundary condition in terms of shear coefficient vs. the mid-height displacement curve is given in Figure 5.7 for the fully converged solution. Based on the response, the results are less stiff for EMM $\phi_{top} \neq 0$ due to boundary conditions, whereas the response is similar to that of wall restraining in the top support rotation (EMM $\phi_{top} = 0$). The evolution of crack pattern is shown in Figure 5.7 at the load levels specified in Figure 5.6.

The initiation of crack starts at the bottom of the wall (Figure 5.7b). At P2p, the crack along the bottom support is fully formed with the initiation of the crack in the diagonal pattern in the wall (Figure 5.7c). As the

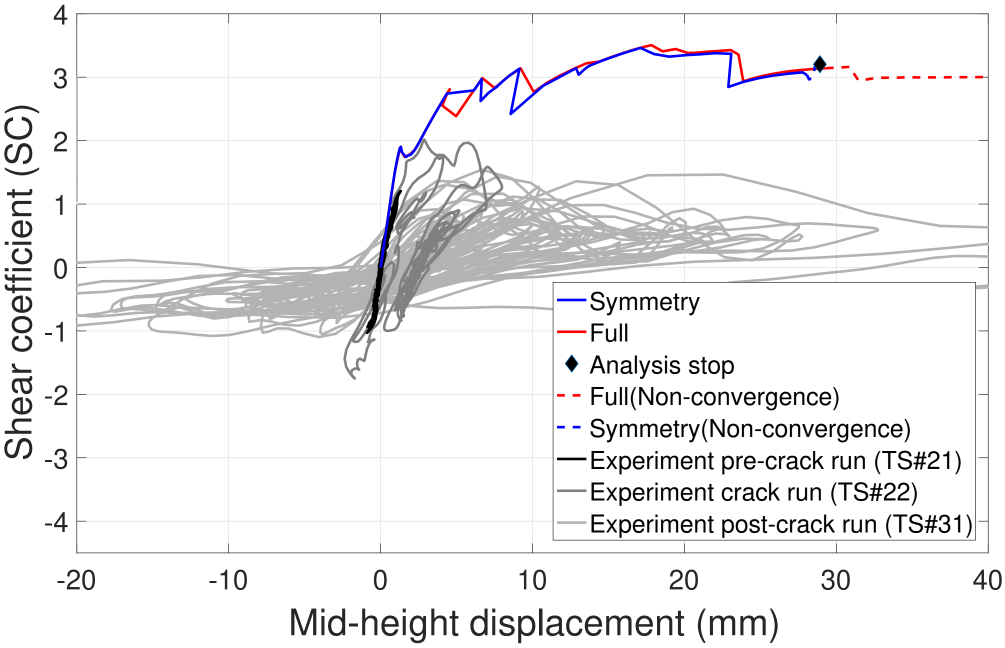

Figure 5.5: Shear coefficient vs mid-height displacement curve for four sides restrained wall (CS-010-RR/CS-005-RR) for full-scale and symmetry model.

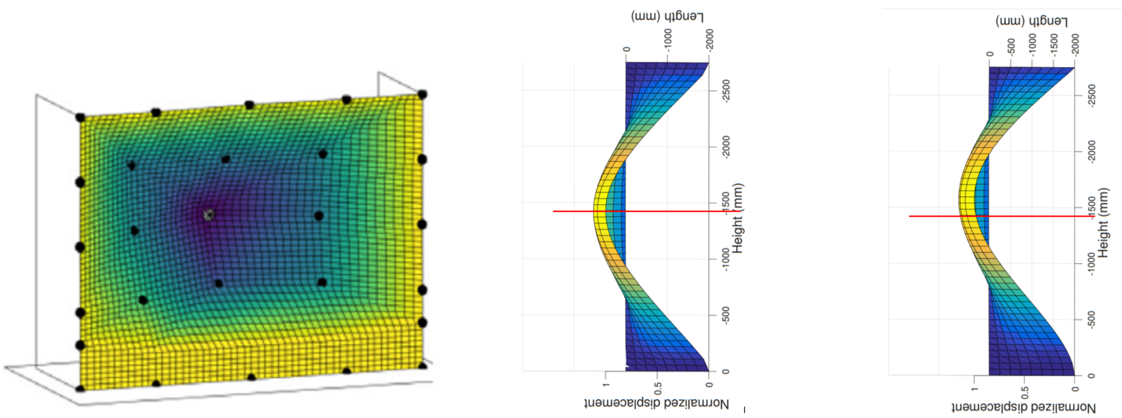

(a) Experiment (b) Numerical $\phi_{top} = 0$ (c) Numerical $\phi_{top} \neq 0$

Figure 5.6: Effect of top boundary condition (rotation) on the deformed shape of main wall.

analysis progress, the horizontal crack in the main wall is fully formed together with a diagonal crack at P3p (Figure 5.7d). After that, the mid-height displacement increases at a faster rate (10.4mm at P4p to 17.04 mm at peak) with an increase in shear coefficient (Figure 5.7e, f). Based on these changing boundary conditions, the crack pattern in the numerical analysis resembles the similarity with that of the right part of the wall from the experiment at failure in addition to the vertical crack in the pier-wall connection (Figure 5.7g). After reaching the peak, the wall reaches the maximum displacement of 24.4mm, and snap back behavior is observed.

Following the second reasoning, wherein the diagonal elements have higher tensile strength and fracture energy to reflect the orthotropic nature of the masonry ([**?**]). In engineering masonry model, these orthotropic nature is account into the model. Furthermore, the tensile strength of the diagonal element is calculated based on the tensile strength in the bed and head joint direction. The numerical model with specifying the diagonal element having higher mode-I fracture energy is carried out. The finite element model of the localized element is shown in Figure 5.10a. The boundary support condition of the numerical model was kept similar to that of the experiment.

The outcome of the numerical results in terms of shear coefficient vs. mid-height displacement (MHD)

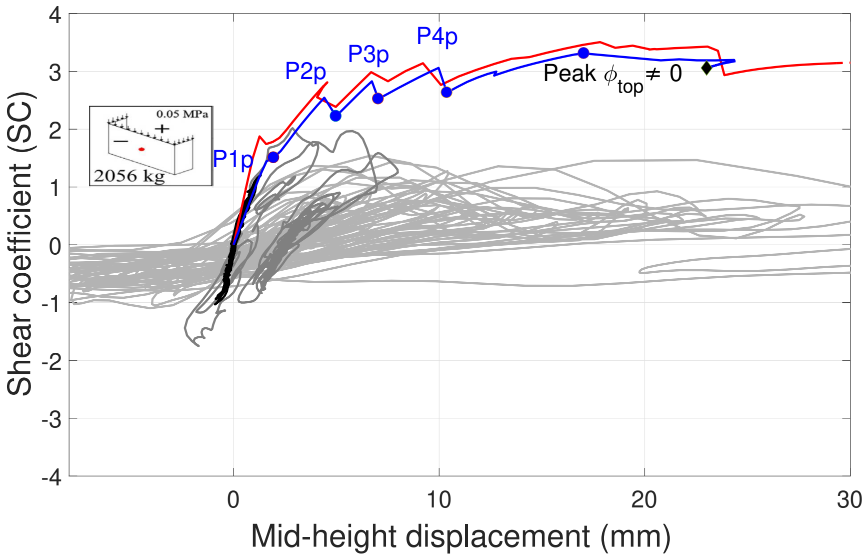

(a) Full response of numerical analysis compared with experiment

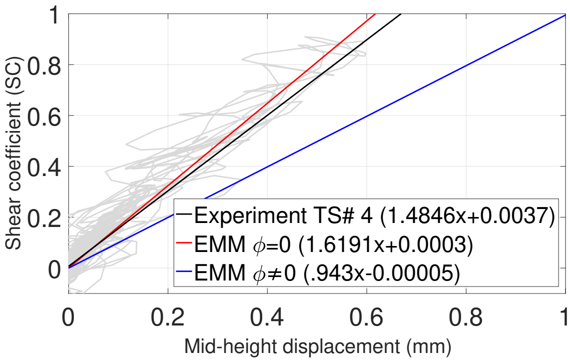

(b) initial stiffness

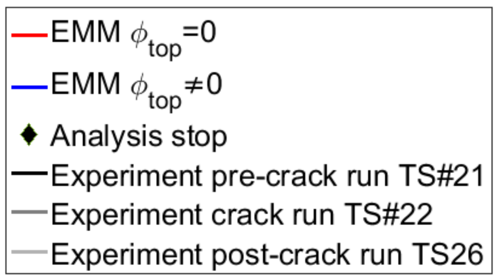

(c) Legend details.

Figure 5.7: Shear coefficient vs mid-height displacement curve for four sides restrained wall (EMM): modified top support condition.

is shown in Figure 5.9a. In Figure 5.9b, the load levels are identified at which the crack propagation in the wall can be traced. The initial stiffness comparison (Figure 5.9c), shows that the analysis with localized element is less stiff. However, post crack (L1p to Peak to end of analysis) response is similar to the one model having uniform properties for all the elements. The crack propagation and evolution in the wall are shown in Figure 5.10 for the indicated load levels.

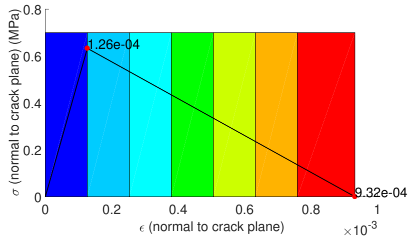

(a) Softening curve.

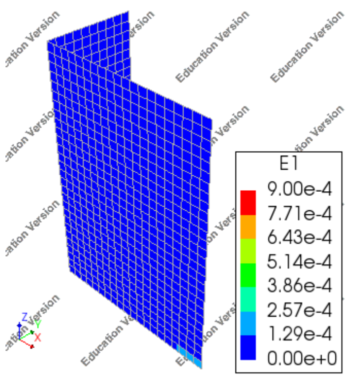

(b) P1p (MHD= 1.95 mm & F=30.4 kN)

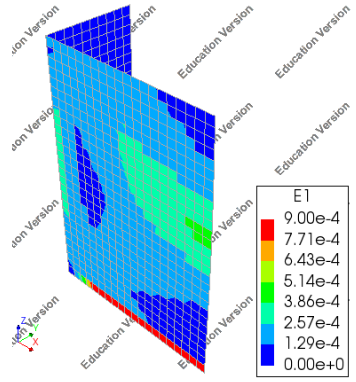

(c) P2p (MHD= 4.98 mm & F= 44.85 kN)

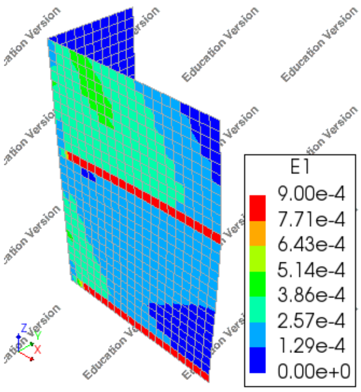

(d) P3p (MHD= 7.04 mm & F= 50.9 kN)

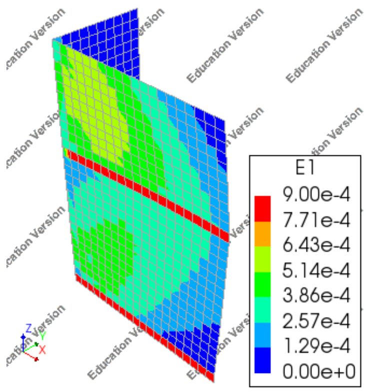

(e) P4p (MHD= 10.38 mm & F= 53.1 kN)

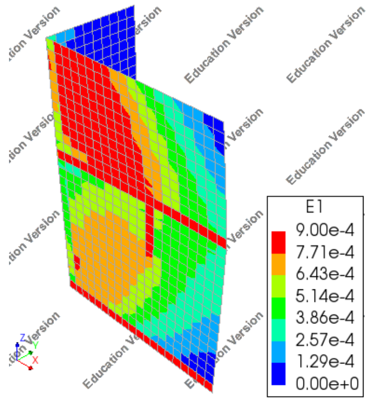

(f) Peak (MHD= 17.04 mm & F= 66.77 kN)

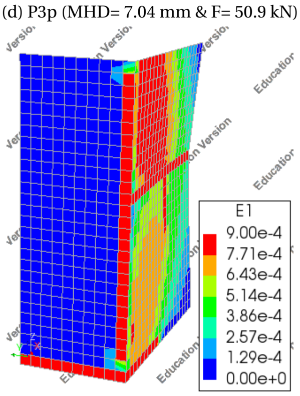

(g) Side view at peak.

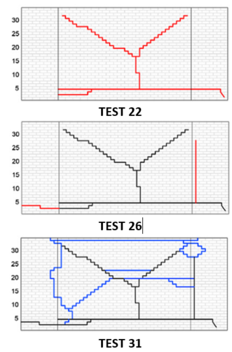

(h) Experiment crack

Figure 5.8: Four sides restrained wall (EMM): Maximum principal strain at different load levels specified in Figure 5.7 with modified top support condition.

5.1.2. Wall restrained on three sides

The result of the numerical analysis for calcium silicate wall with free top support is presented in the Figure 5.11. The stiffness of the numerical analysis using the EMM material model is less compared to the experimental results (shown in inset). Whereas, the stiffness using TSRC is close to the linear trend line of the TS# 17 of the experiment. As done previously, a contour plot of maximum principal strain is reported for the point indicated in the SC vs. TD plots. The legends of the principal strain plot are following Figure 5.1.

The contour plot is shown in Figure 5.12, presents the evolution of crack as the analysis progress. The cracks specimen is started at the bottom support and the connection between the main-wall and pier (E1p). With an increase in loading, the crack along with the main wall-pier connection progress along the edge (E2p), and crack along the main wall in the vertical line is formed (E3p). The state of crack at E3p is similar to the first crack observe in the experiment at the end of TS # 18. Finally, at the peak load (Peakp), horizontal

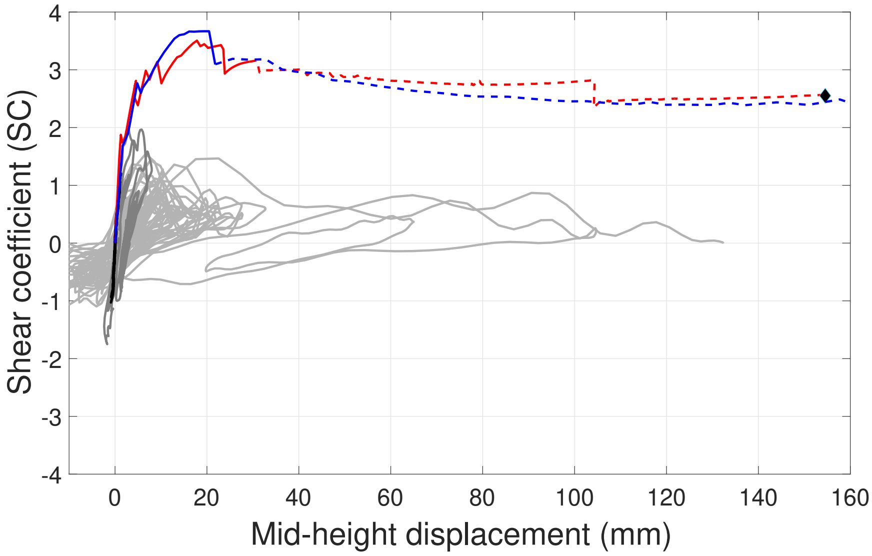

(a) Full response of numerical analysis compared with experiment

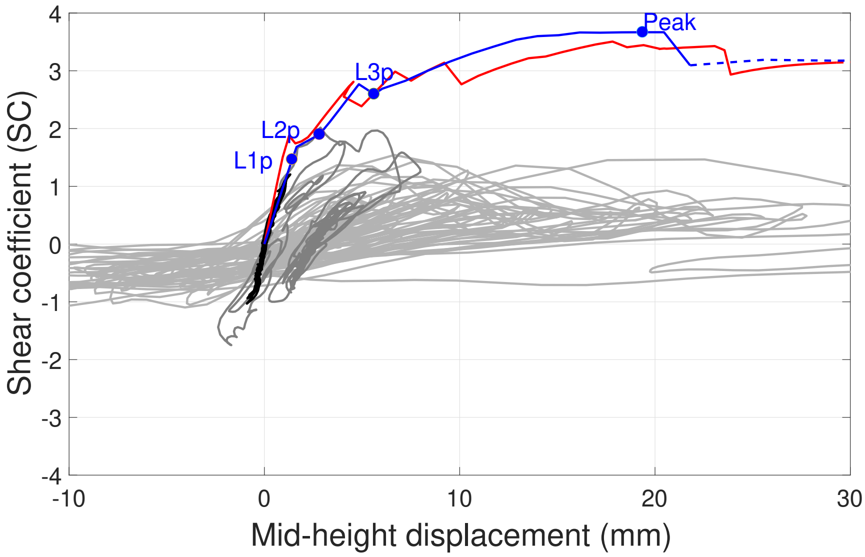

(b) Details of load levels

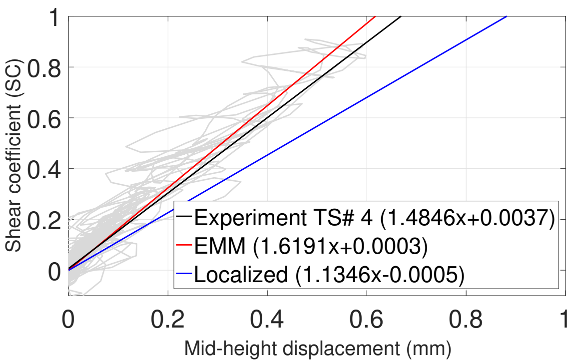

(c) initial stiffness

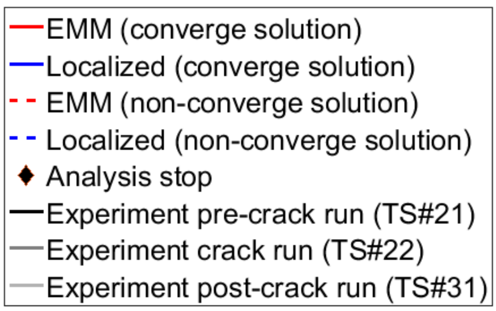

(d) initial stiffness

Figure 5.9: Shear coefficient vs mid-height displacement curve for four sides restrained wall (CS-010-RR/CS-005-RR) with localized element.

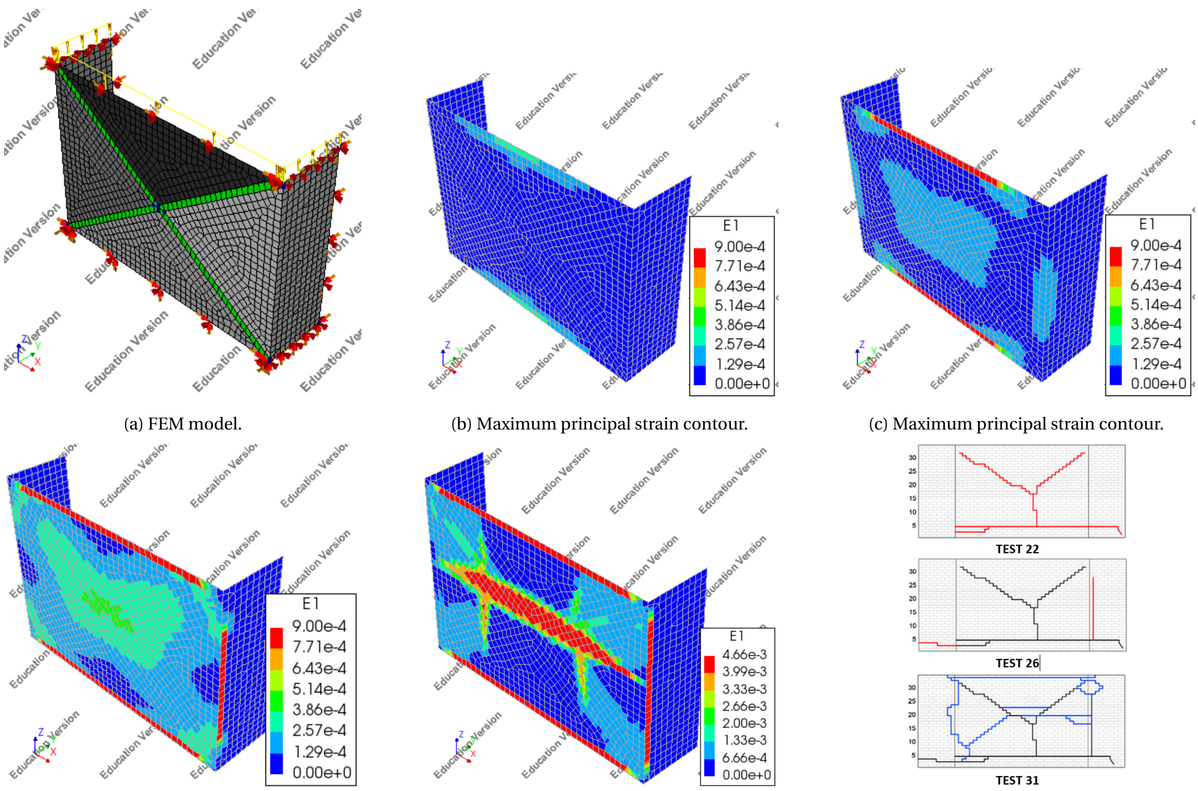

(a) FEM model. (b) Maximum principal strain contour. (c) Maximum principal strain contour.

(d) Maximum principal strain contour. (e) Maximum principal strain contour. (f) Experiment crack

Figure 5.10: Four sides restrained walls (Localized element): Maximum principal strain at different load levels specified in Figure 5.9

crack is initiated (Figure 5.12d) in the upper half of the main wall, which resembles the crack pattern observe at the complete failure in the experiment (Figure 5.12e). Furthermore, the non-convergent solution is shown with the dashed line for EMM.

Numerical analysis with uniform load acting in the direction away from the pier, the cracking is initiated at the junction of the main-wall and pier also with a mid-vertical line of the main wall (Figure 5.12f). As the load increases, the crack progresses rapidly along the edge, covering 50% of the height, which is accompanied by a slight decrease in force (E1n to E2n). With an increase in load, the full connection between the main-wall and pier reached the ultimate strain. The softening in the main wall follows the shape of λ. This crack pattern is typical for a two-way spanning URM with no support condition at the top in the literature (Figure 2.8).

The crack evolution shows the changes in the lateral load-carrying scheme with the progress of analysis. Before the formation of full vertical crack at the connection of the main-wall and pier, the load is resisted mainly by the horizontal bending along the vertical edge. As the cracks along the vertical edge fully formed, the wall panel is free to rotate about these edges, and load is only resisted by the bed joint torsion (Figure 5.12c). Finally, the main wall panel can resist the external load via vertical bending giving rise to horizontal crack in the main wall panel Figure 5.12d.

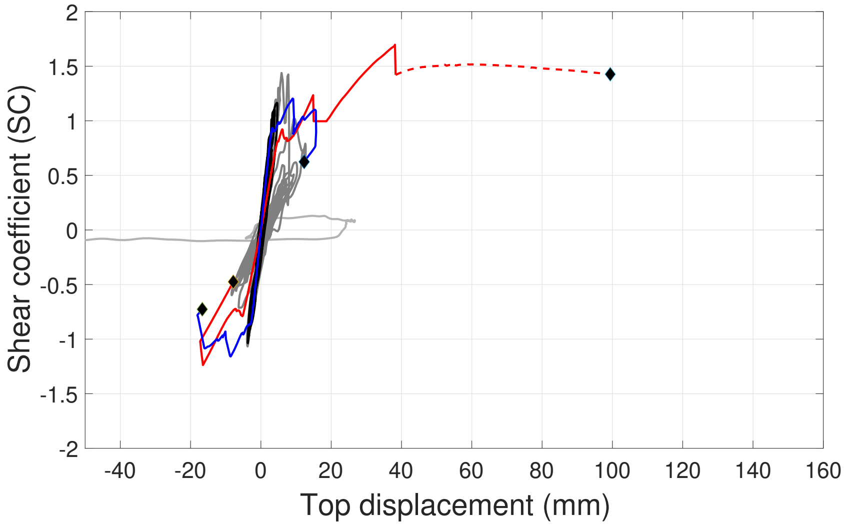

(a) Full response of numerical analysis compared with experiment

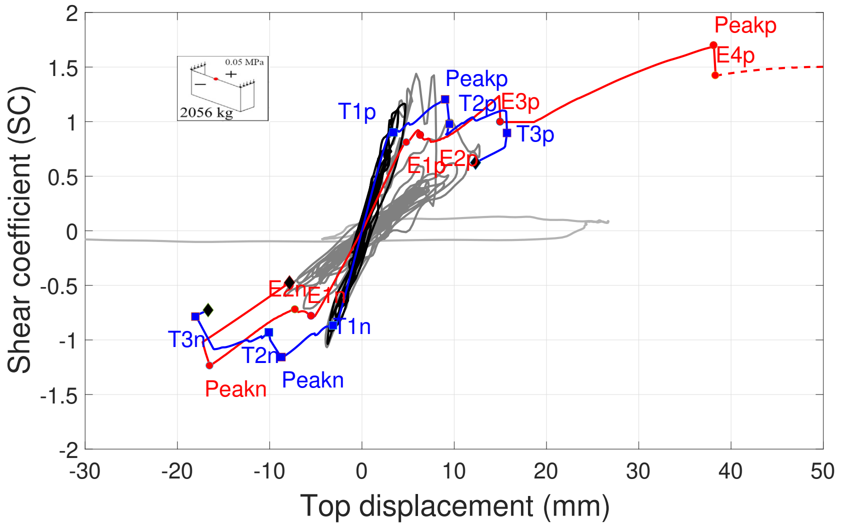

(b) Details of load levels

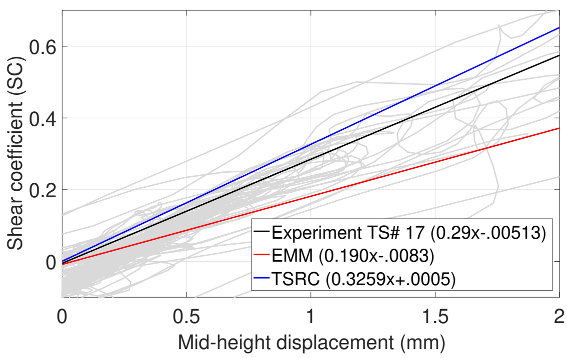

(c) initial stiffness

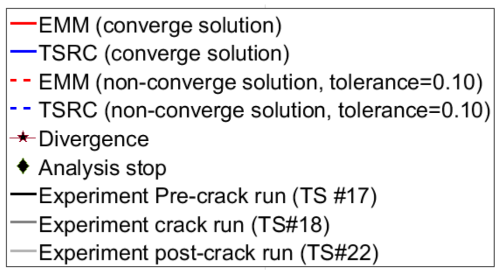

(d) Legend details.

Figure 5.11: Shear coefficient vs mid-height displacement curve for three sides restrained wall (CS-000-RF) comparing engineering masonry model (EMM) and total strain rotating crack model (TSRC).

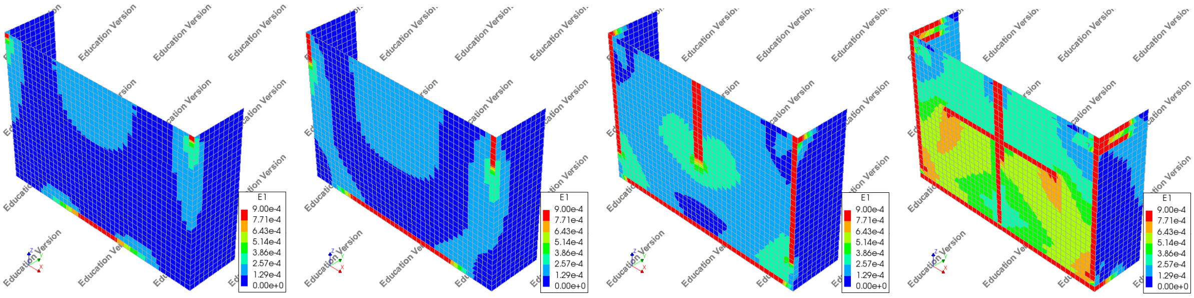

(a) E1p (TD =4.837mm & F=16.32kN). (b) E2p (TD=15.003mm & F=20.09kN) (c) E3p (TD=15.003mm & F=20.09kN) (d) Peakp (TD=38.143mm & F=34.23kN).

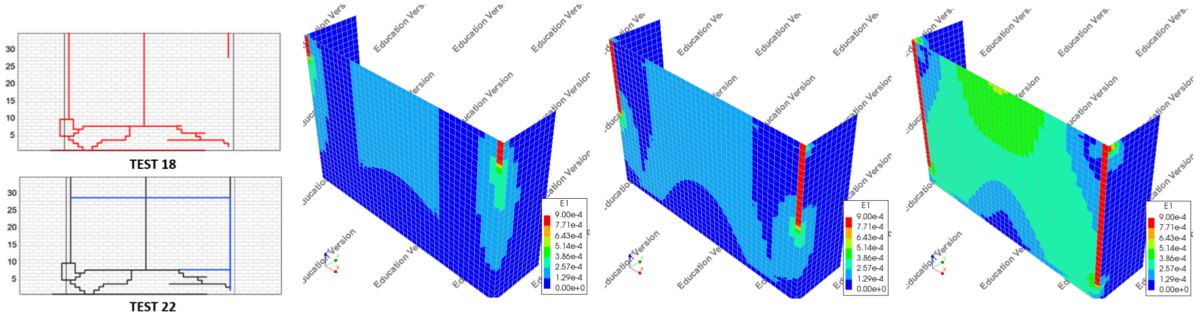

(e) Experiment (f) E1n (TD=-5.480mm & F=-15.73kN). (g) E2n (TD=-7.234mm & F=-14.56kN). (h) Peakn (TD=-8.054mm & F=-15.02kN).

Figure 5.12: Three sides restrained walls (EMM): Maximum principal strain at different load levels specified in Figure 5.11.

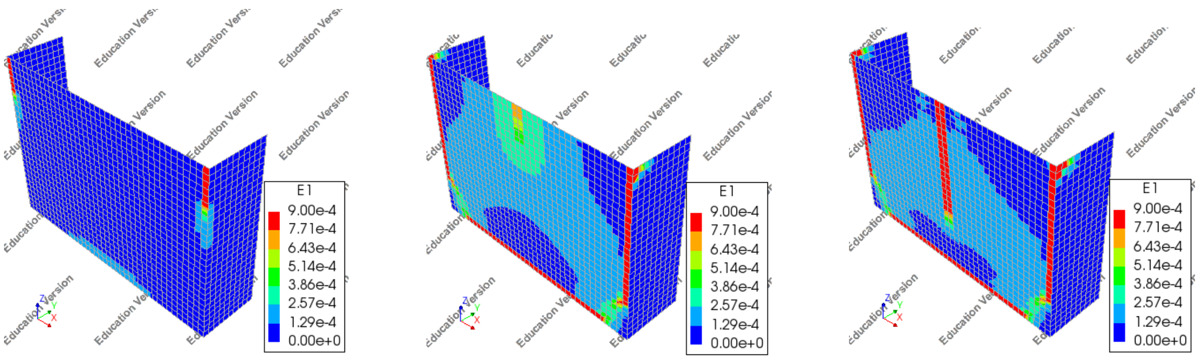

(a) T1p (TD=3.50mm & F=18.21kN). (b) T2p (TD=9.904mm & F=19.61kN). (c) Peakp (TD=9.232mm & F=24.23kN).

Figure 5.13: Three sides restrained walls (TSRC): Maximum principal strain at different load levels specified in Figure 5.11

5.2. Non-linear static analysis (Mode proportional loading)

5.2.1. Wall restrained on four sides

In the mode proportional loading, the load shape applied similar to the first mode of the structure identifying from eigenvalue analysis. Referring to the first mode shape Figure 4.10, the magnitude of load in the center of the main wall is of considerable intensity as compared to the edges. Because of this, the rapid degradation in the stiffness occurs, and the force capacity is significantly lower as compared to the experiment, as shown in Figure 5.14a. The support condition is kept similar to that of the experiment. The material sensitivity study was done for mode-I fracture energy to get the peak shear coefficient as close to the peak experiment shear coefficient. Based on the outcomes, for $G_f^I = 0.118$N/mm, the peak load level is close to the experiment. As the analysis progress, the drop in load is followed by the snap-back behavior; hence, the analysis stops. The crack pattern at the peak load level is shown in Figure 5.14b.

5.2.2. Wall restrained on three sides

For three sides restrained wall, the mode-proportional analysis keeping the material properties similar to that of the non-linear static analysis presented in the previous section (section 5.1), the response obtained are less

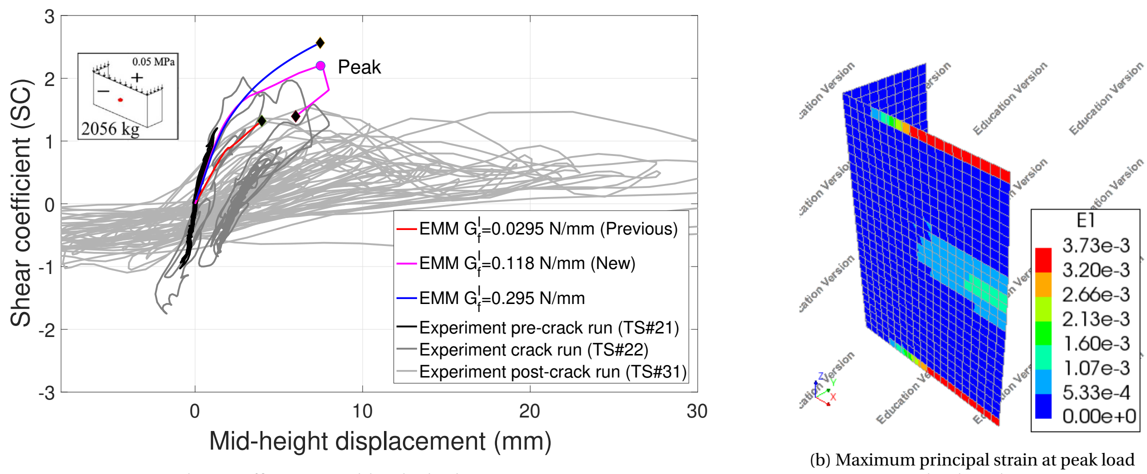

(a) Shear coefficient vs mid-height displacement curve.

(b) Maximum principal strain at peak load level (Peak).

Figure 5.14: Four sides restrained walls (EMM): subjected to mode proportional loading.

stiff, and the peak load observed at a top-displacement of 40mm (Figure 5.15a). In the material sensitivity study, in addition to mode-I fracture energy, Young's modulus, tensile strength, and mode-II fracture energy are changed as detailed in Table 5.1. Note for clarity x-axis scale is shown from -20mm to 50mm. The response of this analysis is shown in Figure 5.15a labeled EMM (New). The crack pattern at the peak load level (Peak4) shown in Figure 5.15b for the calibrated material parameter. However, these crack pattern is similar for the other peak load also using different material parameters. The applied load intensity is higher at the wall top and small near the bottom support; therefore, the significant portion of the external load is resisted by the horizontal bending along the vertical edges. Hence, the crack initiation in these analysis starts at the wall-pier connection, rather than wall bottom as shown for non-linear static analysis with uniform loading (Figure 5.12).

Parameter	Unit	Value
E_x=E_y	MPa	12000
f_{tx}	MPa	0.6
f_{ty}	MPa	0.3
G_f^I	N/mm	0.118
G_f^{II}	N/mm	0.04

Table 5.1: Wall restrained on three sides:Parameter deduced from the material sensitivity study for EMM update.

The non-linear static analysis with mode-proportional loading required material sensitivity study for the inputted parameters. These parameters are modified to obtain the initial stiffness and peak shear coefficient close to the experimental curves. Based on the material sensitivity study CS-005-RR, mode-I fracture energy is needed to increase by four times, while in CS-000-RF, in addition to mode-I, and mode-II fracture energy, the stiffness, Young's modulus, and tensile strength in the direction parallel and perpendicular needed to be changed

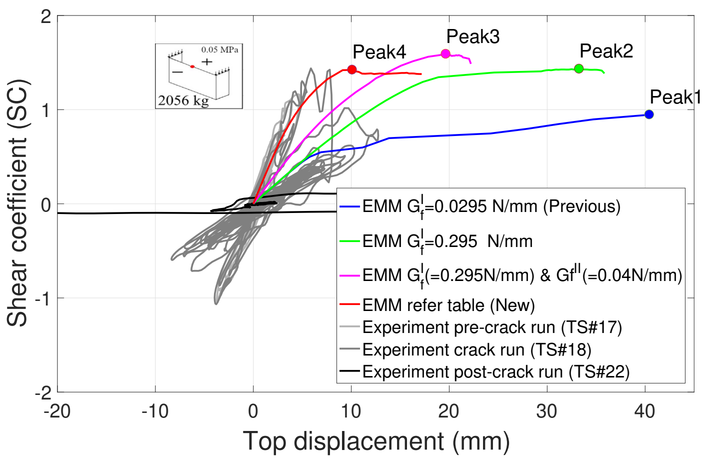

(a) Shear coefficient vs mid-height displacement curve.

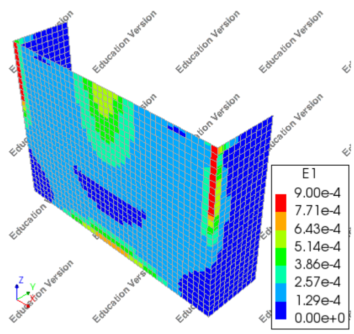

(b) Maximum principal strain at peak load level (Peak4).

Figure 5.15: Three sides restrained walls (EMM): subjected to mode proportional loading.

5.3. Non-linear time history analysis (NLTH)

In the following section, the result of non-linear time history analysis is presented and discussed for two material models, namely, TSRC and EMM, for both the specimens. The aim is to verify the critical parameters like stiffness, peak SC, maximum displacement (MHD or TD) in both the positive and negative direction, as well as the evolution of crack patterns in the model.

5.3.1. Wall restrained on four sides

The input acceleration signal used for the NLTH analysis corresponds to TS # 21, 22, and 26, which represents the pre-crack, first crack, and post crack run in the analysis. The reason for starting the NLTH analysis from TS # 21 is that no crack is found in the individual test run up to TS #21. Moreover, in the experiment, the first crack is detailed after TS# 22 based on visual observation.

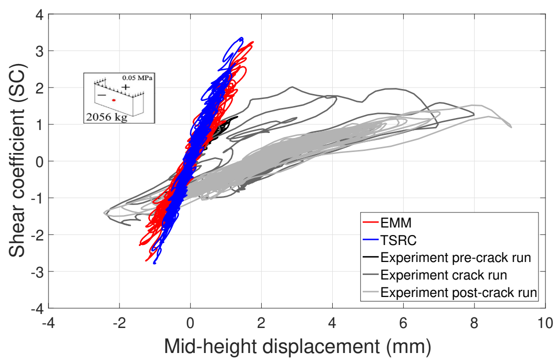

(a) Hysteretic response using shear force obtained from support reaction.

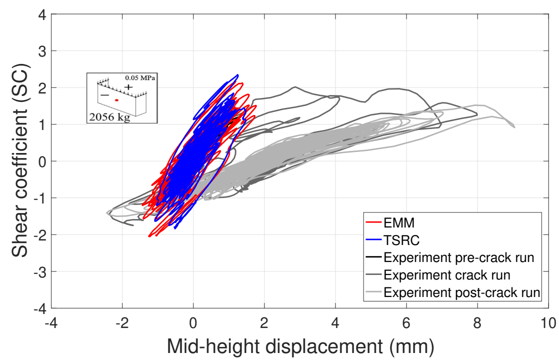

(b) Hysteretic response using shear force obtained from acceleration.

Figure 5.16: Shear coefficient vs mid-height displacement curve for four sides restrained wall (CS-005-RR) comparing engineering masonry model (EMM) and total strain rotating crack model (TSRC) in Non-linear time history analysis

The base shear force calculated in the experiment by obtaining the acceleration record at the designated point multiply by the mass allocated the particular point. With the progress of the analysis, the mass allocated to these points changes with the evolution of new cracks. However, in the finite element analysis, the base shear force can be obtained directly from the support reaction (Figure 5.16a). Whereas, to undertake a proper comparison with the experimental results, the accelerations obtained at the node close to the data acquisition points are obtained to calculate the base shear force (Figure 5.16b).

In Table 5.2, details such as stiffness, maximum MHD, and peak SC are tabulated for experiment and numerical results. The stiffness is calculated using the slope of the linear trend line for each test sequence.

The SC and MHD for TS# 21 in the negative displacement direction are close to 20% difference, whereas, in the positive displacement direction, over 20% for both EMM and TSRC. Moreover, the stiffness is found to be in good agreement with the experiment. Similar to the experiment, no crack is identified in the experiment in both the positive and negative displacement direction, as shown in Figure 5.17b,c, and Figure 5.18b,c for both EMM and TSRC model respectively.

			EMM		TSRC	
	Item	Experiment	Value	% diff	Value	% diff
TS-21	Slope	1.263	1.272	0.7	1.386	9.74
	SC +/-	1.21/-1.03	1.54/ -1.19	27/16	1.58/-1.19	30/16
	MHD_{max} +/-	1.33/-0.89	0.94/ -0.79	29/11	0.90/-0.67	32/24
TS-22	Slope	0.193	1.035	436	1.275	560
	SC +/-	2.02/-1.75	2.17/ -2.05	7.5/17	2.35/-1.84	16/5
	MHD_{max} +/-	7.98/-2.37	1.77/ -1.43	78/39	1.48/-1.04	81/56
TS-26	Slope	0.353	1.110	214	1.123	325
	SC +/-	1.52/-1.5	1.46/-1.57	3.6/4.5	1.49/ -1.51	0/8.9
	MHD_{max} +/-	9.04/-2.44	1.18/ -1.41	87/42	0.95/-1.08	89/55

Table 5.2: Four sides restrained wall: Quantitative comparison between experiment and numerical results, in terms of slope (linear regression line), shear coefficient, and max MHD for test sequence 21-22-26.

Test sequence # 21	Test sequence # 22	Test sequence # 26

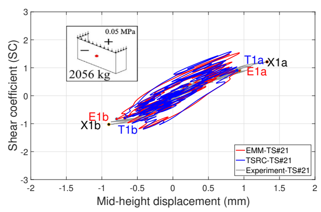

(a) Test sequence 21 (SC based on acceleration)

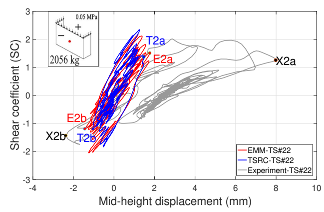

(d) Test sequence 22 (SC based on acceleration)

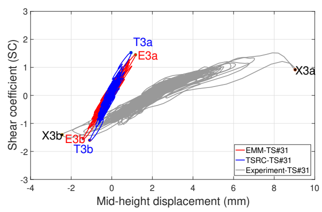

(g) Test sequence 26 (SC based on acceleration)

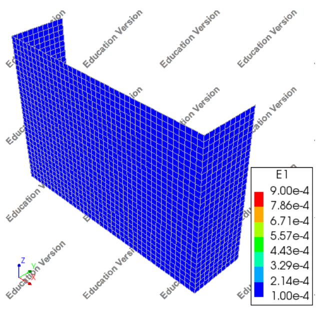

(b) Q1a (MHD=0.937mm).

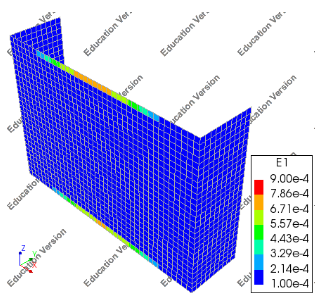

(e) Q2a (MHD=1.770mm).

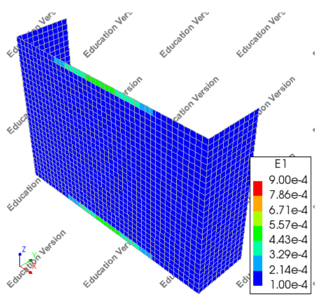

(h) Q3a (MHD=1.177mm).

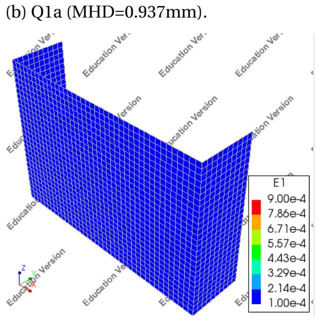

(c) Q1b (MHD=-0.789mm).

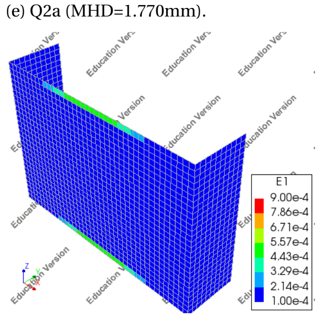

(f) Q2b (MHD=-1.436mm).

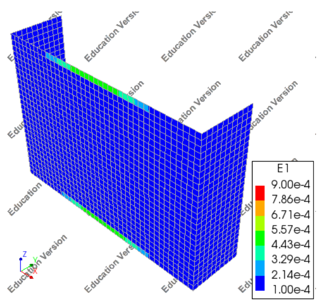

(i) Q3b (MHD=-1.409mm).

Figure 5.17: Four sides restrained walls (EMM): Maximum principal strain contour plots at the load level indicated in SC vs MHD plots.

Test sequence # 21	Test sequence # 22	Test sequence # 26

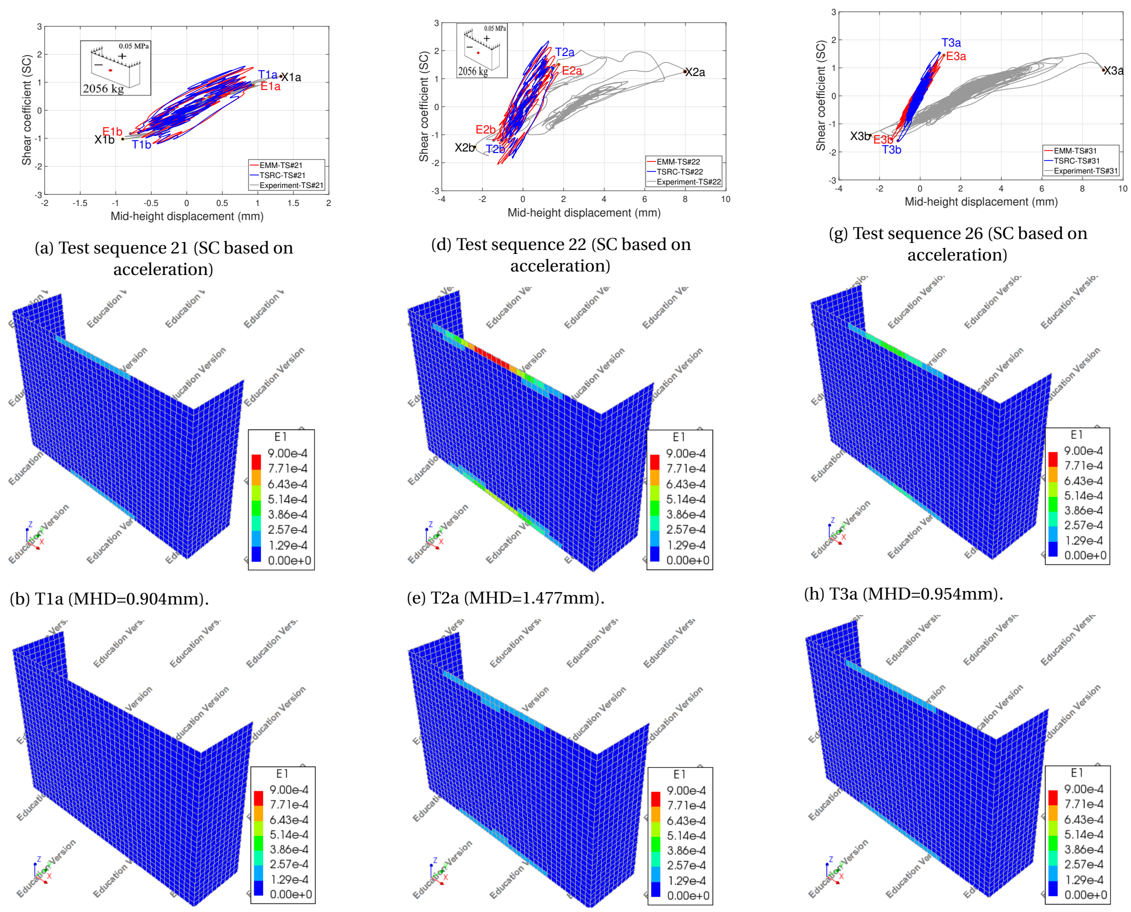

(a) Test sequence 21 (SC based on acceleration)

(d) Test sequence 22 (SC based on acceleration)

(g) Test sequence 26 (SC based on acceleration)

(b) T1a (MHD=0.904mm).

(e) T2a (MHD=1.477mm).

(h) T3a (MHD=0.954mm).

(c) T1b (MHD=-0.675mm).

(f) T2b (MHD=-1.038mm).

(i) T3b (MHD=-1.083mm).

Figure 5.18: Four sides restrained walls (TSRC): Maximum principal strain contour plots at the load level indicated in SC vs MHD plots.

As the analysis progress into the crack run i.e., TS# 22, the degradation of stiffness and increased in MHD can not be captured in the numerical analysis. On the contrary, SC_{max} in both the positive and negative direction are within 20% difference as that of an experiment. The primary reason for this behavior is due to the use of short-time signal used in the analysis. Because of the short time signal, cracks that are initiated could not dissipate energy. Hence, the displacement (MHD) of the wall is limited. During the crack run, cracks are only initiated only in the top and bottom support for both the material models, as shown in Figure 5.17e,f, and Figure 5.18e,f. Similar to the crack-run, the post-crack run i.e., TS#26, does not show any further degradation in the wall. Since the peak-ground acceleration of the signal (in TS# 26) is lower than the crack-run; as a result of the cracks that are opened and shown in the Figure 5.17e,f for higher strain value, does not reach at the same state in the post-crack run in the numerical analysis Figure 5.17h, i. This similarity is also identified in the TSRC (Figure 5.18h,i). Based on the NLTH analysis for the wall restrained on four sides, the difference in the response based on the material model can not be made.

The outcomes of the non-linear time history analysis with modified boundary condition in-wall restrained on four sides are presented in terms of shear coefficient vs. mid-height displacement in Figure 5.19. The details of the parameters are tabulated in Table 5.3 shows the changing the boundary conditions the results improve significantly. In the experiment, the hysteretic cycles are concentrated at the MHD of 2mm after the crack run results in permanent deformation in the wall mid-height due to crack. This slipping off behavior can not be simulated using the shell elements in finite element analysis. Furthermore, the crack evolution is plotted in Figure 5.20 for the maximum positive and negative displacement directions. The contour plots show, besides, to crack at the wall bottom (failure of bed-joint), initiation of a diagonal crack in the main wall, but the cracks are not fully formed. Therefore, based on NLTH analysis with modified top boundary conditions evident that the horizontal support at the top can rotate.

			$EMM\ \phi_{top} \neq 0$	
	Item	Experiment	Value	% diff
TS-21	Slope	1.263	.873	45
	SC +/-	1.21/-1.03	1.535/ -1.255	21/18
	MHD_{max} +/-	1.33/-0.89	1.365/-1.535	2/42
TS-22	Slope	0.193	.734	74
	SC +/-	2.02/-1.75	2.011/ -1.843	0/5
	MHD_{max} +/-	7.98/-2.37	2.585/ -2.545	208/7
TS-26	Slope	0.353	.713	50
	SC +/-	1.52/-1.5	1.296/-1.415	17/6
	MHD_{max} +/-	9.04/-2.44	1.866/-2.248	385/9

Table 5.3: Four sides restrained wall with changed top support boundary: Quantitative comparison between experiment and numerical results, in terms of slope (linear regression line), shear coefficient, and max MHD for test sequence 21-22-26.

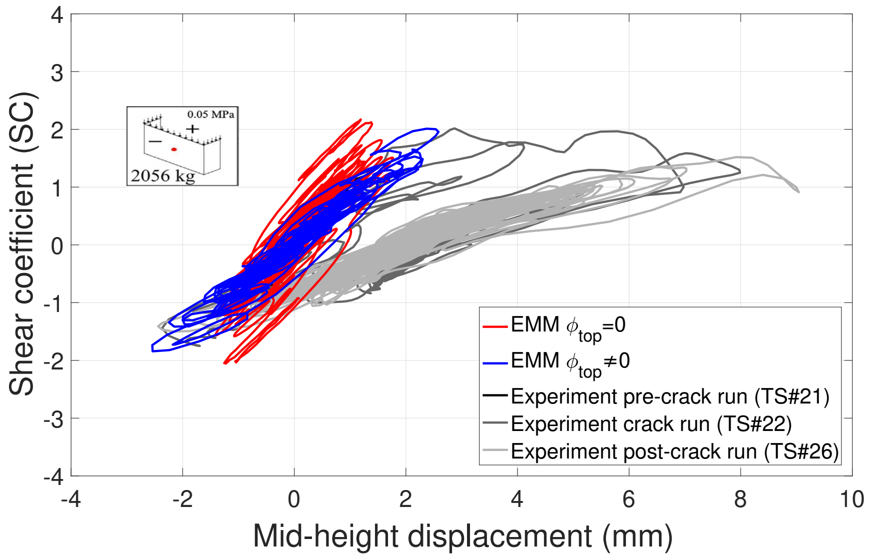

Figure 5.19: Shear coefficient vs mid-height displacement curve for four sides restrained wall with modified top support condition.

Test sequence # 21	Test sequence # 22	Test sequence # 26

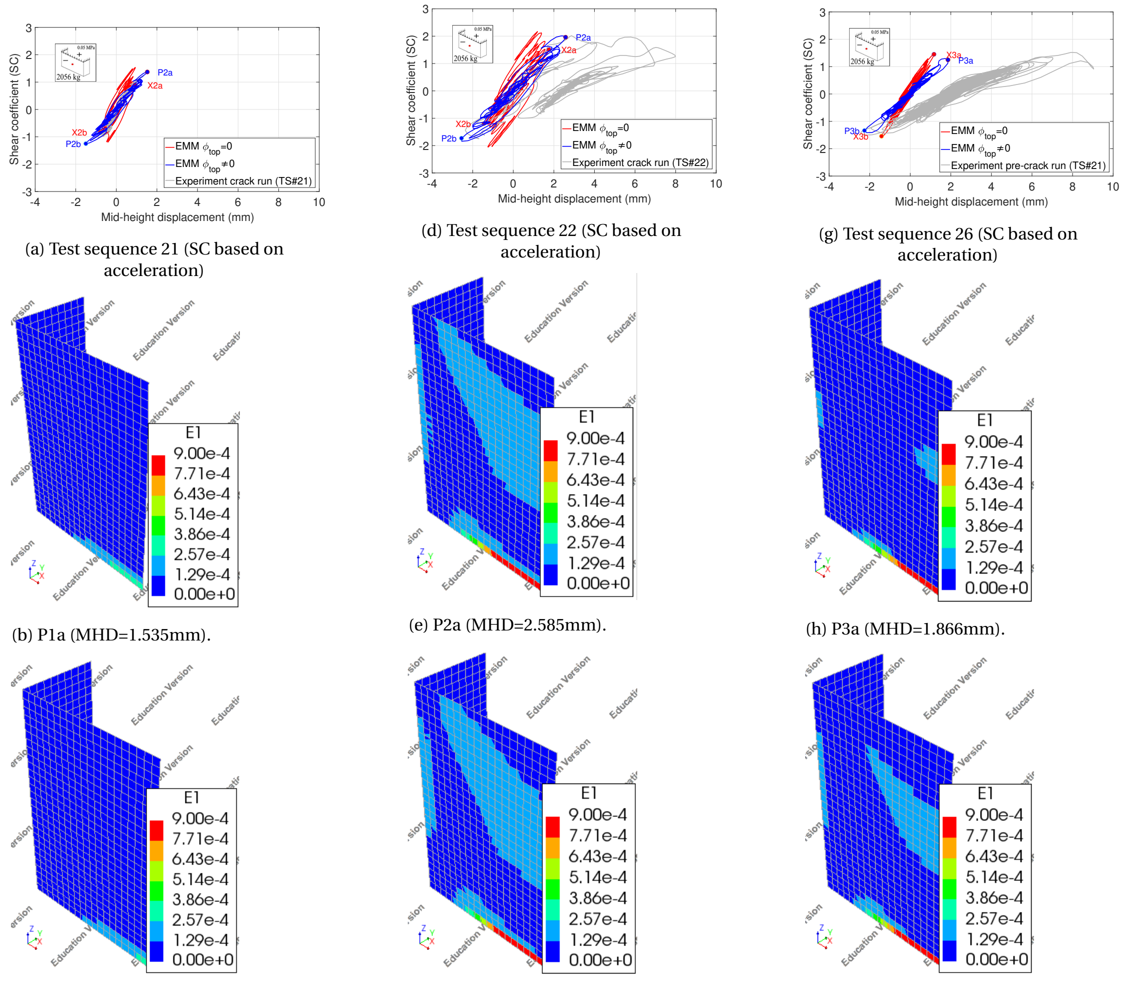

(a) Test sequence 21 (SC based on acceleration)

(d) Test sequence 22 (SC based on acceleration)

(g) Test sequence 26 (SC based on acceleration)

(b) P1a (MHD=1.535mm).

(e) P2a (MHD=2.585mm).

(h) P3a (MHD=1.866mm).

(c) P1b (MHD=–1.495mm).

(f) P2b (MHD=-2.545mm).

(i) P3b (MHD=–2.247mm).

Figure 5.20: Four sides restrained walls (modified top support): Maximum principal strain contour plots at the load level indicated in SC vs MHD plots.

5.3.2. Wall restrained on three sides

The input signal used for the NLTH analysis for the wall restrained on three sides is TS#17, TS#18, and TS#20. These signals correspond to the pre-crack, crack, and post a crack run in the experiment. Similar to the CS-005-RR, the hysteresis response can be obtained (1) by obtaining the base shear force directly (Figure 5.21a)or (2) by obtaining the acceleration at the nodes close to the instrument locations in the experiment (Figure 5.21b).

In the pre-crack run (TS# 17), the response obtained using EMM and TSRC has a vast gap compared to the experiment outputs Table 5.4. The primary reason being the fully opened crack in the numerical model along the (one-fourth length of) wall-pier connection together with bottom support of the main wall, as shown in Figure 5.22b,c for EMM. While in the TSRC material model, the crack along with the wall-pier connection and mid-vertical of the main wall is fully opened Figure 5.23a,b. Based on the observation, the base acceleration is resisted by both the horizontal bending along with the vertical wall-pier connection and vertical bending by bottom support. Furthermore, the zone of crack initiation is observed in the mid-top portion of the main wall.

As the analysis progress to crack-run (TS# 18), the length of the crack formed previously increased further, as seen in Figure 5.22e,f. Furthermore, in the negative direction, the vertical crack in the mid of the main wall is started at the top. The analysis using the TSRC material model, the solution does not converge for the full-time history. Whereas, the solution with EMM is converged for the full-time history, but shows the higher displacement reach of the wall as compared to the experiment.

Finally, in the post-crack run (TS# 22), since the magnitude of the signal and peak ground acceleration of the overall time signal is very less compared to crack run. The vast difference in shear coefficient and top displacement is found. Since the maximum displacement reached by the wall top is significantly less, most of the crack closes and hence the principal-strain plot shown in Figure 5.22h, i is at lower strain value.

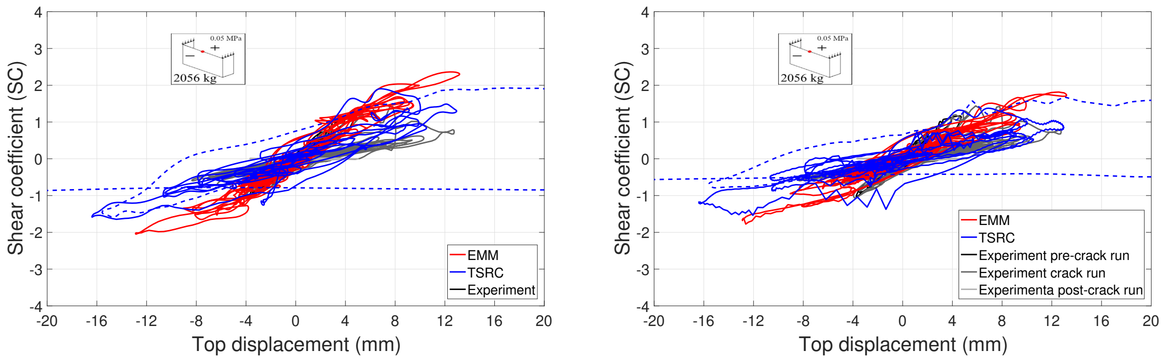

(a) Hysteretic plot of non-linear time history analysis combine with experiment.

(b) Hysteretic plot of non-linear time history analysis combine with experiment.

Figure 5.21: Shear coefficient vs top displacement curve for three sides restrained wall (CS-000-RF) comparing engineering masonry model (EMM) and total strain rotating crack model (TSRC) in Non-linear time history analysis.

			EMM		TSRC	
	Item	Experiment	Value	% diff	Value	% diff
TS-17	Slope	0.291	0.225	22.5	0.1137	61
	SC +/-	1.17/-1.04	1.67/-1.31	43/26	1.375/-1.537	12/48
	TD_{max} +/-	4.71/-3.75	9.93/-8.12	80/117	12.95/-16.42	175/337
TS-18	Slope	0.0903	0.129	43	9×10^{-5}	-
	SC +/-	2.08/-1.08	1.82/-1.78	13/64	1.789/-0.994	14/8
	TD_{max} +/-	12.75/-8.36	13.19/-12.9	3/54	164.14/-401.74	-
TS-20	Slope	0.00	0.11	-	-	-
	SC +/-	0.03/-0.02	0.27/-0.31	725/1319	-0.068/-0.082	127/312
	TD_{max} +/-	5.03/-3.69	1.48/-3.35	70/9	-402.34/-768.31	-

Table 5.4: Three sides restrained wall: Quantitative comparison between experiment and numerical results, in terms of slope (linear regression line), peak shear coefficient, and max TD for test sequence 17-18-20.

Based on the above outcomes of NLTH analysis for wall restrained on four sides, for the given input signal, not sufficient cracks are developed that could dissipate the energy. The NLTH analysis using the full-time signal is performed for the test sequence given in Table 5.5. The outcomes of the results show the wall restrained on the four sides is still showing stiff response as the MHD_{max} reached in the post-crack run is under 3mm in both the positive and displacement direction.

Test Seq.	Signal input	S.F.	MHD_{max} +/- (mm)	SC +/-	
21	FEQ2-DS4	400%	1.01 / -0.64	1.69/-1.26	Pre-crack run
22	FEQ2-DS4	600%	1.79/-1.39	2.82/-2.57	Crack-run
26	SSWx2	250%	1.47 / -1.27	2.01/-2.11	
28	SSWx2	150%	0.86/-0.96	1.18/-1.29	
31	SSWx2	300%	2.47/-3.02	2.19/-2.56	Post-crack run

Table 5.5: Four sides restrained wall: Details of the input signal, obtained maximum MHD and corresponding SC. (S.F.= Scale factor)

Figure 5.24 shows the outcome of the analysis in terms of SC vs. MHD, and the respective principle-strain is plotted for pre-crack, crack, and post-crack run. Based on the principal strain plots of the crack run shows,

Test sequence # 17	Test sequence # 18	Test sequence # 20

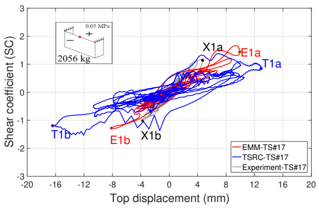

(a) Test sequence 17 (SC based on acceleration).

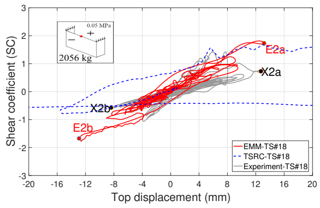

(d) Test sequence 18 (SC based on acceleration).

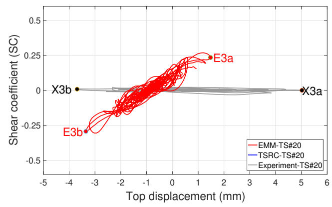

(g) Test sequence 20 (SC based on acceleration).

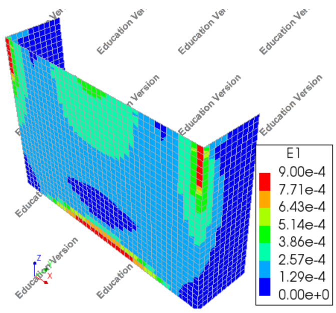

(b) Q1a (TD=9.931mm).

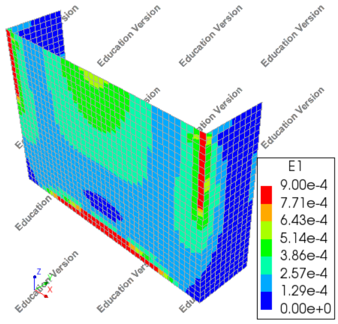

(e) Q2a (TD=13.186mm).

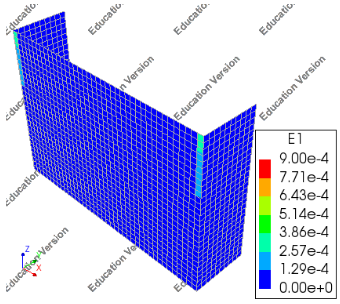

(h) Q3a (TD=1.484mm).

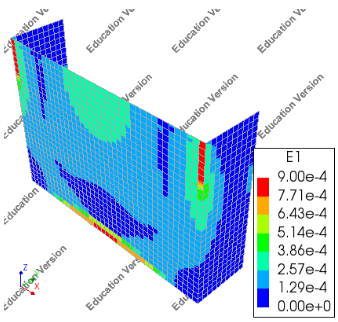

(c) Q1b (TD=-8.115mm).

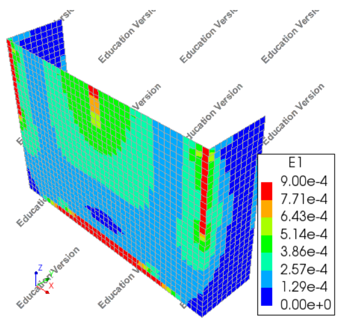

(f) Q2b (TD=-12.890mm).

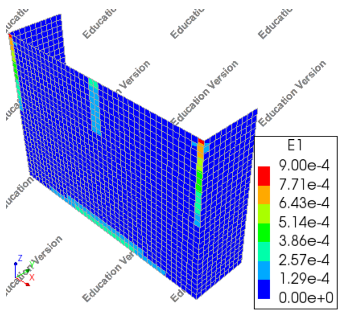

(i) Q3b (TD=-3.350mm).

Figure 5.22: Three sides restrained walls (EMM): Maximum principal strain contour plots at the load level indicated in Figure 5.21.

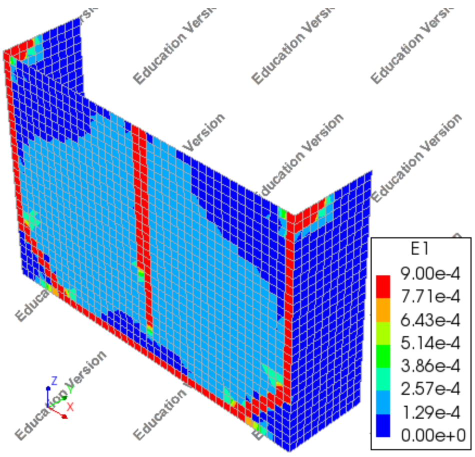

(a) T1a

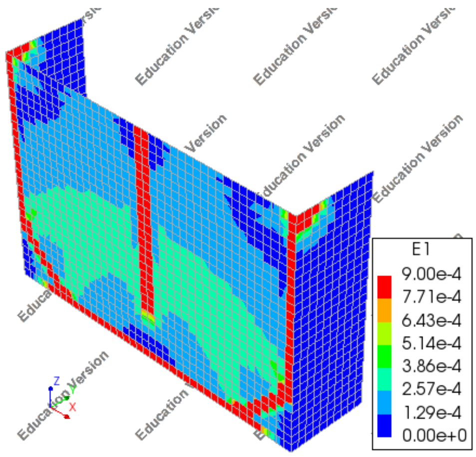

(b) T1b

Figure 5.23: Three sides restrained walls (TSRC): Maximum principal strain contour plots at the maximum top displacement in test sequence 17.

cracks are only open in the element along the top and bottom support. While in the post-crack run, the crack is fully formed along the top and bottom support, crack initiation in the main wall in the diagonal direction, and at the wall-pier connection. Based on the crack pattern and the hysteresis plot, the response of the wall restrained on four sides is stiff using the EMM.

Test sequence # 21	Test sequence # 22	Test sequence # 31

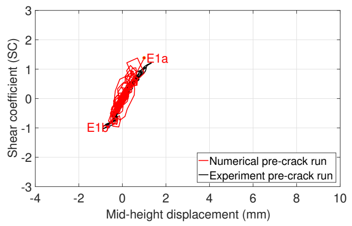

(a) Test sequence 21 (SC based on acceleration)

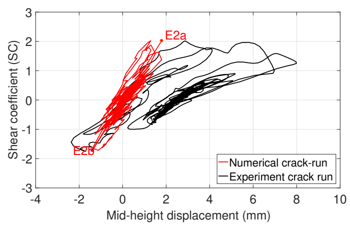

(d) Test sequence 22 (SC based on acceleration)

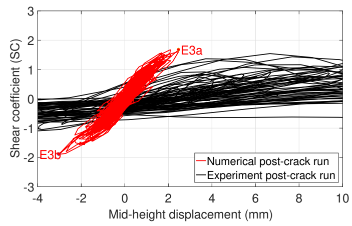

(g) Test sequence 26 (SC based on acceleration)

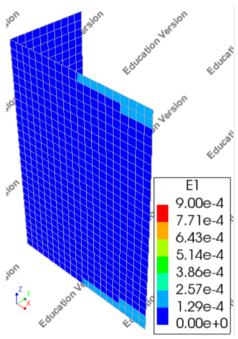

(b) E1a (MHD=1.01mm).

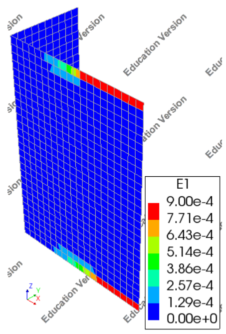

(e) E2a (MHD=1.79mm).

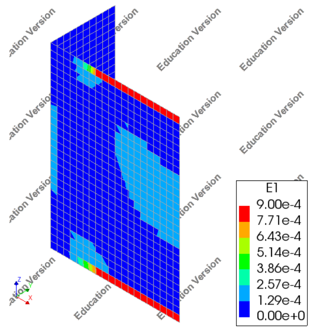

(h) E3a (MHD= 2.47mm).

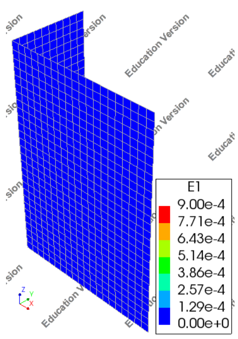

(c) E1b (MHD= -0.64mm).

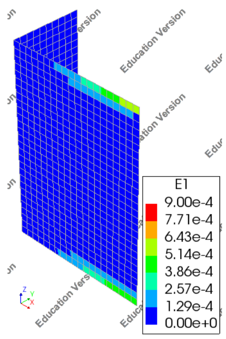

(f) E2b (MHD=-1.39mm).

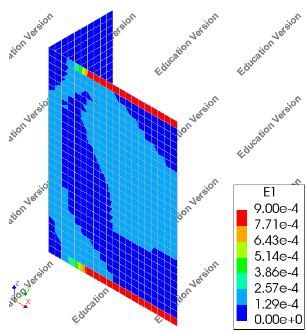

(i) E3b (MHD= -3.02mm).

Figure 5.24: Non-linear time history analysis for four sides restrained walls (long input signal): Maximum principal strain contour plots at the load level indicated in SC vs MHD plots.

NLTH analysis for wall restrained on three sides with a long-time signal was performed. The details of the test sequence, maximum top displacement, and maximum shear coefficient obtained are given in Table 5.6. Based on the outcomes, it can be seen that during the crack run, the maximum top displacement reached in the analysis in both positive and negative displacement direction is greater than the wall thickness. This refers to the complete collapse state in the wall. Furthermore, in test sequence 20, TD is concentrated in the negative displacement direction, which refers to the permanent displacement in the wall.

Test Seq.	Signal input	S.F.	TD_{max} +/- (mm)	SC_{max} +/-	
16	FEQ2-DS4	300%	4.61/-3.99	1.25/-1.02	
17	FEQ2-DS4	350%	13.70/-10.84	1.48/-1.18	Pre-crack run
18	FEQ2-DS4	400%	143.13/-179.17	1.90/-1.39	Crack run
20	FHUIZ-DS0	100%	-30/-41.28	.099/-0.12	
21	FEQ2-DS3	100%	23.73/-59.10	.20/-.19	Post-crack run

Table 5.6: Three sides restrained wall: Details of the input signal, obtained maximum TD and corresponding SC. (S.F.= Scale factor)

The crack pattern in the principle-strain plots is shown for pre-crack and crack run in Figure 5.25. Based on the response, it can be seen that the elements in the bottom half of the main wall reached the ultimate strain value in the crack run. These elements have the residual capacity in out-of-plane shear as observed from the cohesion softening plots in Figure 5.26a for negative displacement direction. Whereas, in positive displacement direction (Figure 5.26b), the elements in the bottom half soften sufficiently in cohesion. The hysteresis response obtained shows the wall have higher displacement capacity (larger than wall thickness) without failure. Furthermore, the response obtained using EMM in the wall restrained on three sides overestimates the displacement capacity when compared to the experiment outcomes.

Test sequence # 17	Test sequence # 18	Test sequence # 21

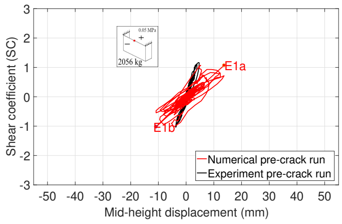

(a) Test sequence 21 (SC based on acceleration)

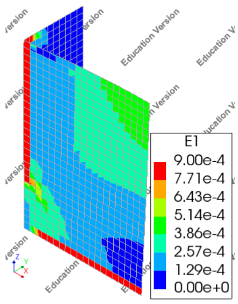

(b) E1a (TD=13.70mm).

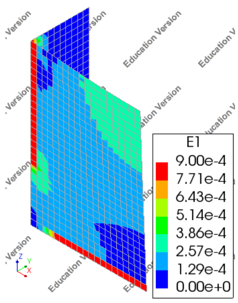

(c) E1b (TD= -10.84mm).

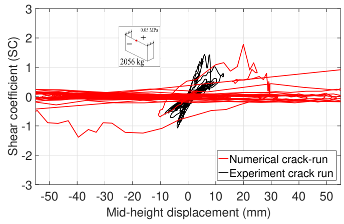

(d) Test sequence 22 (SC based on acceleration)

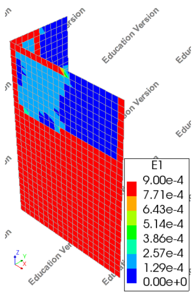

(e) E2a (TD=143.13mm).

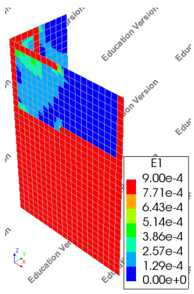

(f) E2b (TD=-179.17mm).

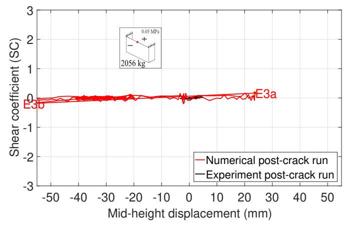

(g) Test sequence 21 (SC based on acceleration)

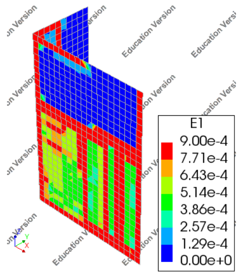

(h) E3a (TD= 23.73mm).

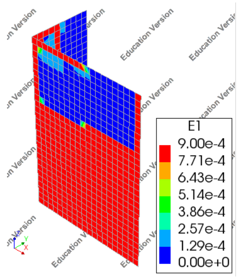

(i) E3b (TD= -59.01mm).

Figure 5.25: Non-linear time analysis for three sides restrained walls (long input signal): Maximum principal strain contour plots at the load level indicated in SC vs TD plots.

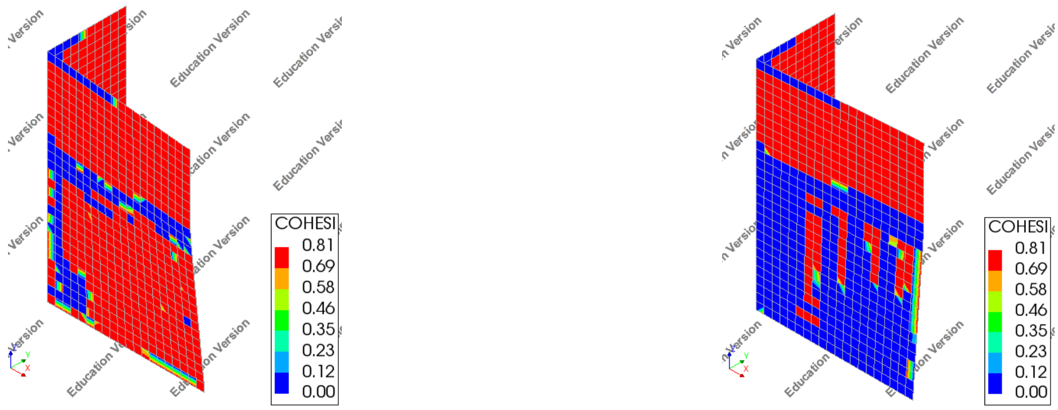

(a) Negative displacement direction.

(b) Positive displacement direction.

Figure 5.26: Three sides restrained walls (long time signal): Cohesion softening in test sequence 18. Absolute deformation scale = 5.

Based on the NLTH analysis, the difference between the EMM and TSRC is not evident for the CS-005-RR specimen. Therefore, the cyclic analysis was performed with a load cycle containing a higher magnitude of loading. The uniform load on the main wall is applied cyclically. Because of the horizontal fixity on the main wall, the NLTH analysis could not show any resemblance to the experiment. Furthermore, the deformed shape of the numerical model presented in Figure 5.6 supports that removing top rotation fixity provides more realistic behavior of the specimen in terms of damage patten. Therefore, top rotation restrained in the main wall is removed in the cyclic analysis for the specimen CS-005-RR.

5.4. Non-linear cyclic analysis

In the following section, the result of the cyclic analysis is presented for both the wall specifications. The comparison between the TSRC and EMM are carried based on the hysteretic plots and the crack pattern. Furthermore, the study is carried out to check the contribution of the out-of-plane shear in net resistance capacity using the energy dissipation plot. For this, EMM has the option to specify mode-II fracture energy. Most often, the out-of-plane shear stress is not considered as internal resisting mechanism due to thin wall thickness. Hence, the effect of shear softening is neglected while computing the capacity of the URM wall to out-of-plane loading. Whereas, in Figure 2.6 of chapter 2 shows bed-joint or head joint torsion as the internal resistance component of the masonry. Hence, the onset of cracking in the wall, energy not only dissipated in tension but also in shear. The two different sets of cyclic analysis are carried out for both the specimens based on the variation of fracture energy in tension and shear as follows:

- Set 1: Mode-I fracture energy (keeping the same value as 0.0295N/mm) is less than the mode-II fracture energy (G_f^{II} = 0.04 N/mm).
- Set 2: Mode-I fracture energy (G_f^{I} =0.118N/mm) is larger than the mode-II fracture energy (G_f^{II} = 0.04 N/mm).

In Set-1, mode-I fracture energy is less than mode-II; therefore, onset cracking the dissipation of energy in shear will be higher compared to a tension based upon the exceedance of shear strength. While in Set-2 parameters, the mode-I fracture energy is higher than the mode-II. As found before (in non-linear static analysis with mode-proportional loading), taking higher fracture energy increases not only the dissipation but also increases the load capacity. Therefore, the Set-II is used for the only purpose to evaluate the contribution of mode-II fracture energy in energy dissipation and on the crack pattern.

For each set of parameters, the results of two different analysis are present in the following section. One with only using mode-I fracture energy in Engineering Masonry Model (EMM G_f^I), second with mode-I and mode-II in EMM (EMM $G_f^I + G_f^{II}$), and third with total strain crack (TSRC) model, where only mode-I fracture energy is specified. The outcome of the numerical analysis is presented in shear coefficient vs. displacement as well as the cumulative energy vs. max displacement reached in each cycle. The *energy dissipation* is calculated from the base shear versus displacement curve as the area enclosed within each hysteretic cycle of each model following the trapezoidal formula.

5.4.1. Wall restrained on four sides

CS-005-RR (Set-1)

The result of the cyclic analysis for the specimen with a pre-compression load of 0.05 MPa on the main wall panel and restrain top support for horizontal translation is presented in the following section. With the Set 1 parameter of fracture energy, the solution did not converge for the complete load cycle, as shown in Figure 5.27a with a dashed line. Furthermore, from Figure 5.27b, no significant difference in the cumulative energy dissipation of the model is based on the inclusion of the mode-II fracture energy in the EMM. Whereas, the energy dissipation using TSRC is less as compared to the EMM. The crack pattern shown for the positive and negative mid-height displacement, at last, converge solution in Figure 5.28. In all the three analyses, the crack in the bottom of the main wall is fully open, as evident from positive and negative displacement direction contour plots. For EMMs, the diagonal crack in the main wall is initiated along with the softening in the wall-pier connection, and the horizontal crack in the main wall is formed in EMM G_f^I. While in TSRC, the diagonal crack in the main wall is initiated in positive displacement direction with a narrow band as compared to EMM, and small diagonal crack connecting bottom support to wall-pier edge in the lower-left corner of the wall.

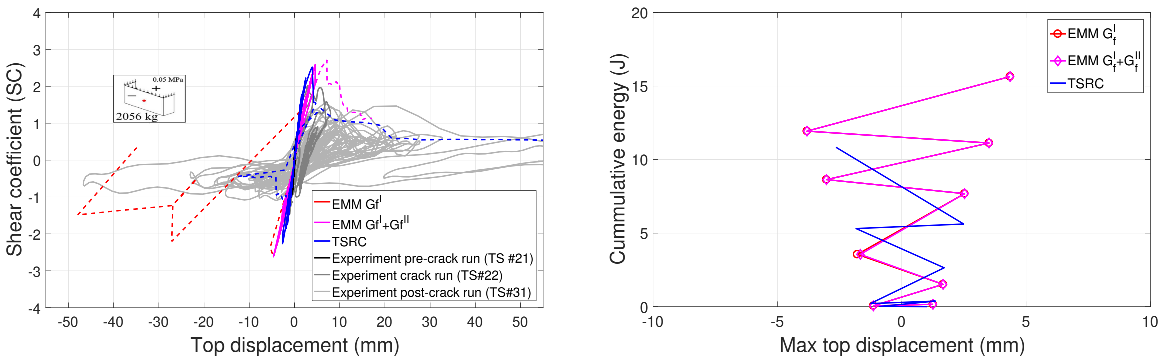

(a) Shear coefficient vs mid-height displacement.

(b) Energy vs max mid-height displacement.

Figure 5.27: Shear coefficient vs top displacement curve for four sides restrained wall (CS-005-RR) for Cyclic analysis for Set-1 parameters (a) Hysteretic response, and (b) Energy dissipation.

CS-005-RR (Set-2)

For the second set of parameters, the mode-I fracture energy is higher than mode-II fracture energy while keeping the rest of the parameters similar to the previous. The result of the hysteretic behaviour is presented in Figure 5.29a. The essential difference due to the inclusion of mode-II fracture energy is visible in the energy dissipation plot (Figure 5.29b). The analysis with EMM $G_f^I + G_f^{II}$ can dissipate more energy as compared to EMM G_f^I, where only mode-I fracture energy is used. Figure 5.30 shows the maximum principal strain contour plots at the positive and negative displacement for the last cycle. The crack pattern formed in EMM $G_f^I + G_f^{II}$ shows a horizontal crack in the wall progress to diagonal pattern together with softening along with the wall-pier connection.

Cyclic analysis of the localized model for CS-005-RR specimens is presented in the following part. Note that the top boundary condition is kept as stated in the experiment i.e., rotation in the top boundary is restrained. The mode-I fracture energy of the diagonal element is five-times higher than the rest of the elements in the model. The hysteretic response of the analysis exhibits the stiff response as compared to the EMM with uniform material properties (Set-1) in all the elements (Figure 5.31a). The maximum principal strain contour plot is shown in Figure 5.32 at the maximum displacement in the positive and negative direction. The contour plots show the element in the diagonal direction starts to crack, which is further supported by higher energy dissipation in the positive displacement direction (Figure 5.31b).

5.4.2. Wall restrained on three sides

CS-000-RF (Set-1)

The outcome of the cyclic analysis for wall restrained on three sides shows the difference in response based on different material models is shown inFigure 5.33a. Using TSRC, the response obtained is stiff, with a relatively

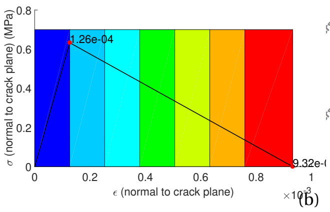

(a) Softening curve.

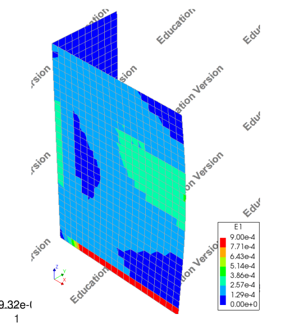

(b) EMM G_f^I: Maximum positive mid-height displacement.

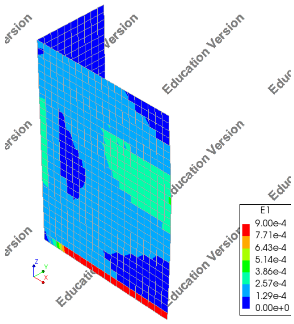

(c) EMM $G_f^I + G_f^{II}$: Maximum positive mid-height displacement

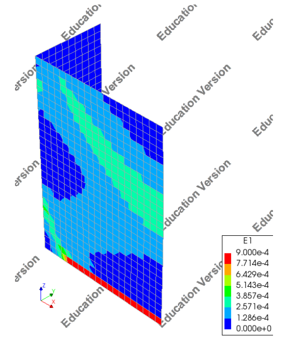

(d) TSRC G_f^I: Maximum positive mid-height displacement

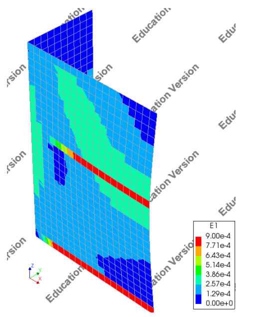

(e) EMM G_f^I: Maximum negative mid-height displacement

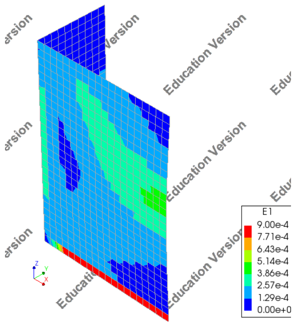

(f) EMM $G_f^I + G_f^{II}$: Maximum negative mid-height displacement

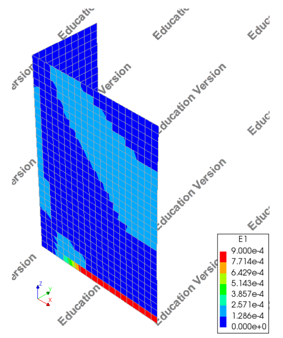

(g) TSRC G_f^I: Maximum negative mid-height displacement

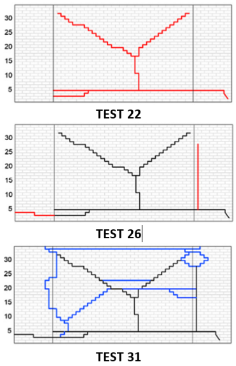

(h) Experiment

Figure 5.28: CS-005-RR (Set-1 parameter): Principal strain plot at the peak positive and negative displacement direction, absolute deformation scale = 5.

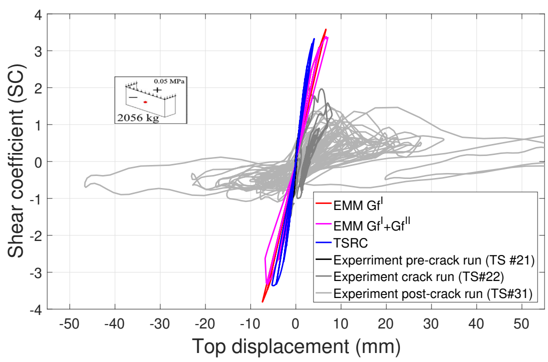

(a) Shear coefficient vs mid-height displacement.

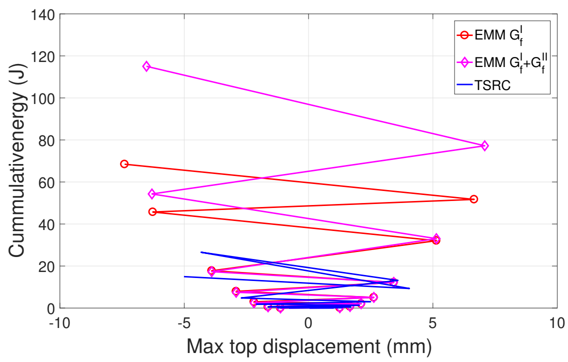

(b) Energy vs max mid-height displacement.

Figure 5.29: Shear coefficient vs top displacement curve for four sides restrained wall (CS-005-RR) for Cyclic analysis for Set-2 parameters (a) Hysteretic response, and (b) Energy dissipation.

small degradation in stiffness with load cycles. Whereas in EMM, degradation in stiffness is rapid, and the wall top reaches larger displacement compared to TSRC. The difference between the two models is also seen based on the cumulative energy dissipation plot shown in Figure 5.33b. The cumulative energy dissipation for the non-converge (dashed line) is excluded for clarity. Furthermore, the cumulative energy dissipation for EMM $G_f^I + G_f^{II}$ is higher than EMM G_f^I and TSRC. Based on the difference in the cumulative energy plot, the contribution due to shear in energy dissipation can be found.

The principle-strain plot for the maximum TD in the positive and negative direction is shown in Figure 5.34. The crack in the bottom support (bed-joint crack) and along the connection between wall-pier (head-joint crack) is formed in all three analyses. In EMM G_f^I, an additional horizontal crack in the upper half of the wall is formed in the thickness of the wall representing the bed-joint crack. While in EMM $G_f^I + G_f^{II}$, the

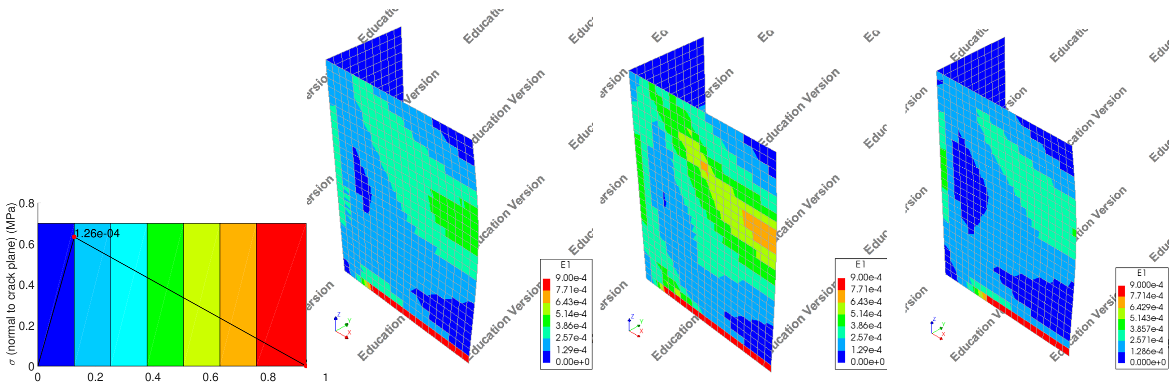

(a) Softening curve. (b) EMM G_f^I: Maximum positive mid-height displacement. (c) EMM $G_f^I + G_f^{II}$: Maximum positive mid-height displacement (d) TSRC G_f^I: Maximum positive mid-height displacement

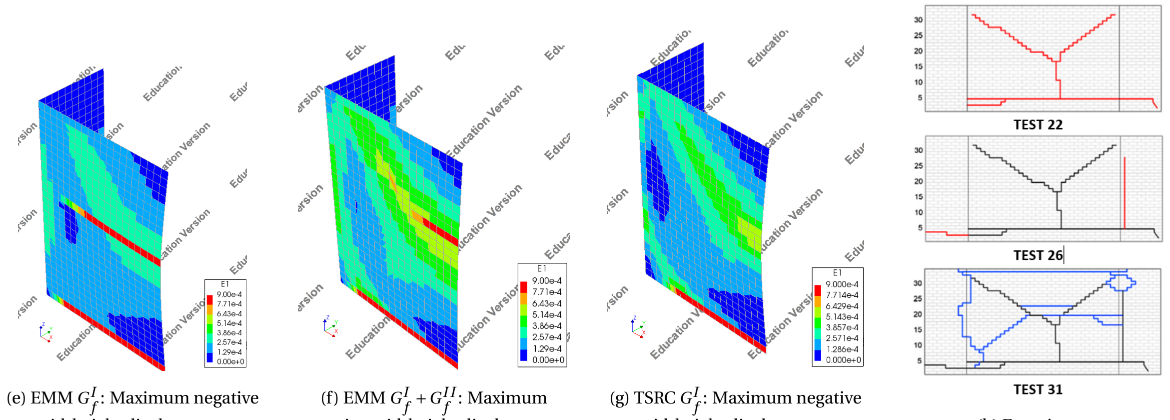

(e) EMM G_f^I: Maximum negative mid-height displacement (f) EMM $G_f^I + G_f^{II}$: Maximum negative mid-height displacement (g) TSRC G_f^I: Maximum negative mid-height displacement (h) Experiment.

Figure 5.30: CS-005-RR (Set-2 parameter): Principal strain plot at the peak positive and negative displacement direction, Absolute deformation scale = 5.

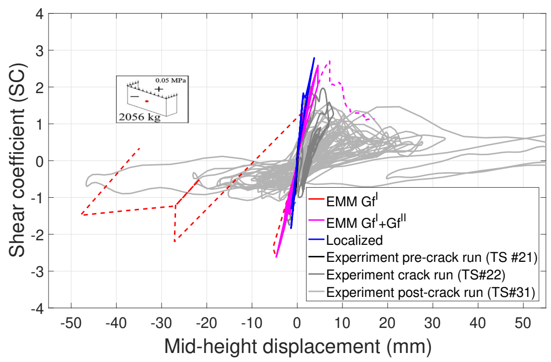

(a) Shear coefficient vs mid-height displacement.

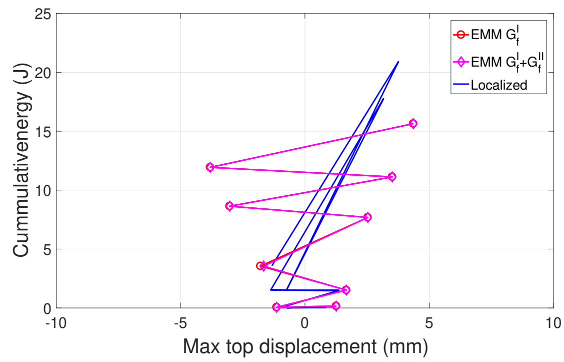

(b) Energy vs max mid-height displacement.

Figure 5.31: Shear coefficient vs top displacement curve for four sides restrained wall (Localized element) for Cyclic analysis(a) Hysteretic response, and (b) Energy dissipation.

initiation of the horizontal crack is visible in the negative displacement direction only. In TSRC, no crack in the wall (in the horizontal direction) is seen.

CS-000-RF (Set-2)

The hysteretic response using the Set-2 parameter is shown in Figure 5.35a and corresponding energy dissipation in each cycle is plotted against the max TD in Figure 5.35b. The response of EMM with or without mode-II fracture energy is clear differentiable in the last converge loading cycle. The maximum principal strain plot in the maximum TD in the positive and negative direction is shown in Figure 5.36.

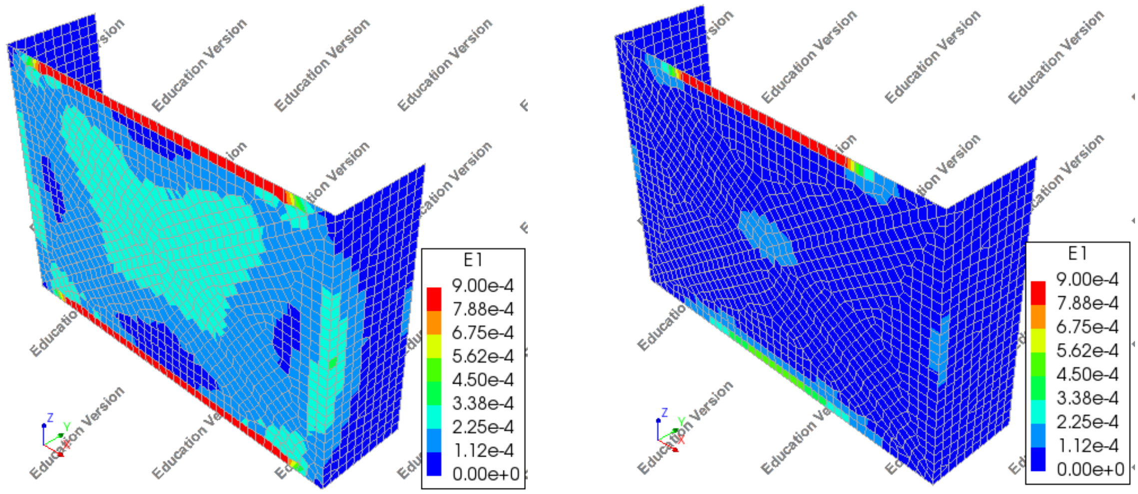

(a) Maximum positive mid-height displacement.

(b) Maximum negative mid-height displacement.

Figure 5.32: CS-005-RR Localized model: Principal strain plot at the maximum MHD in positive and negative direction.

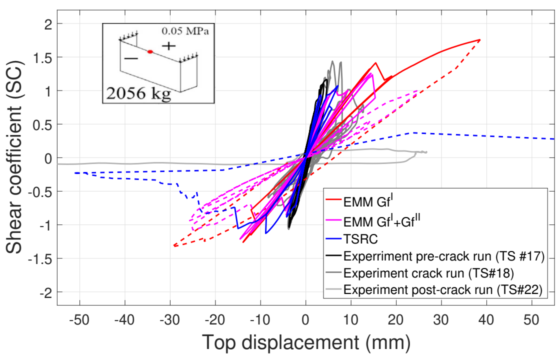

(a) Shear coefficient vs mid-height displacement.

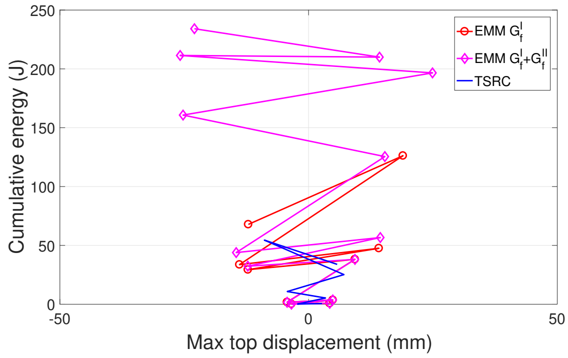

(b) Energy vs max mid-height displacement.

Figure 5.33: CS-000-RF (Set-1 parameters): (a) Hysteretic response, and (b) Energy dissipation

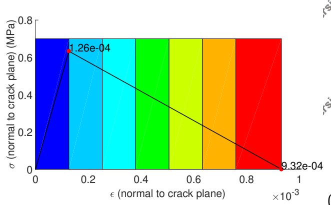

(a) Softening curve.

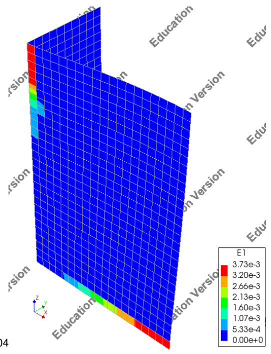

(b) EMM G_f^I: Maximum positive mid-height displacement.

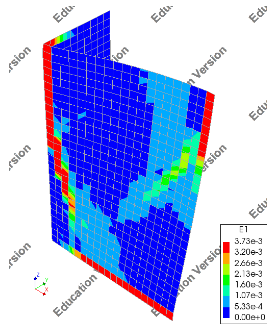

(c) EMM $G_f^I + G_f^{II}$: Maximum positive mid-height displacement

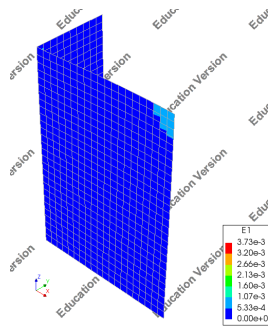

(d) TSRC G_f^I: Maximum positive mid-height displacement

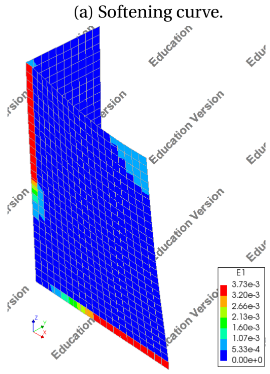

(e) EMM G_f^I: Maximum negative mid-height displacement

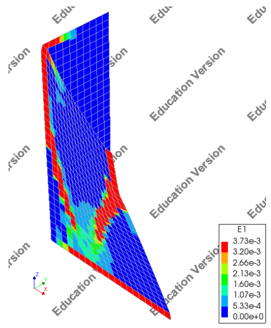

(f) EMM $G_f^I + G_f^{II}$: Maximum negative mid-height displacement

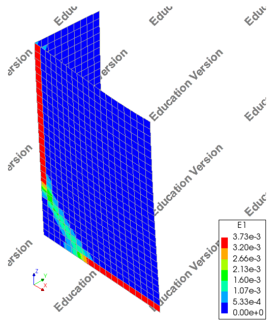

(g) TSRC G_f^I: Maximum negative mid-height displacement

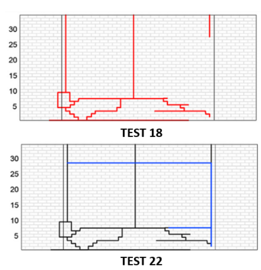

(h) Experiment

Figure 5.36: CS-000-RF (Set-2 parameters): Principal strain plot at the peak positive and negative displacement direction using Set-2 parameters. Absolute deformation scale 10

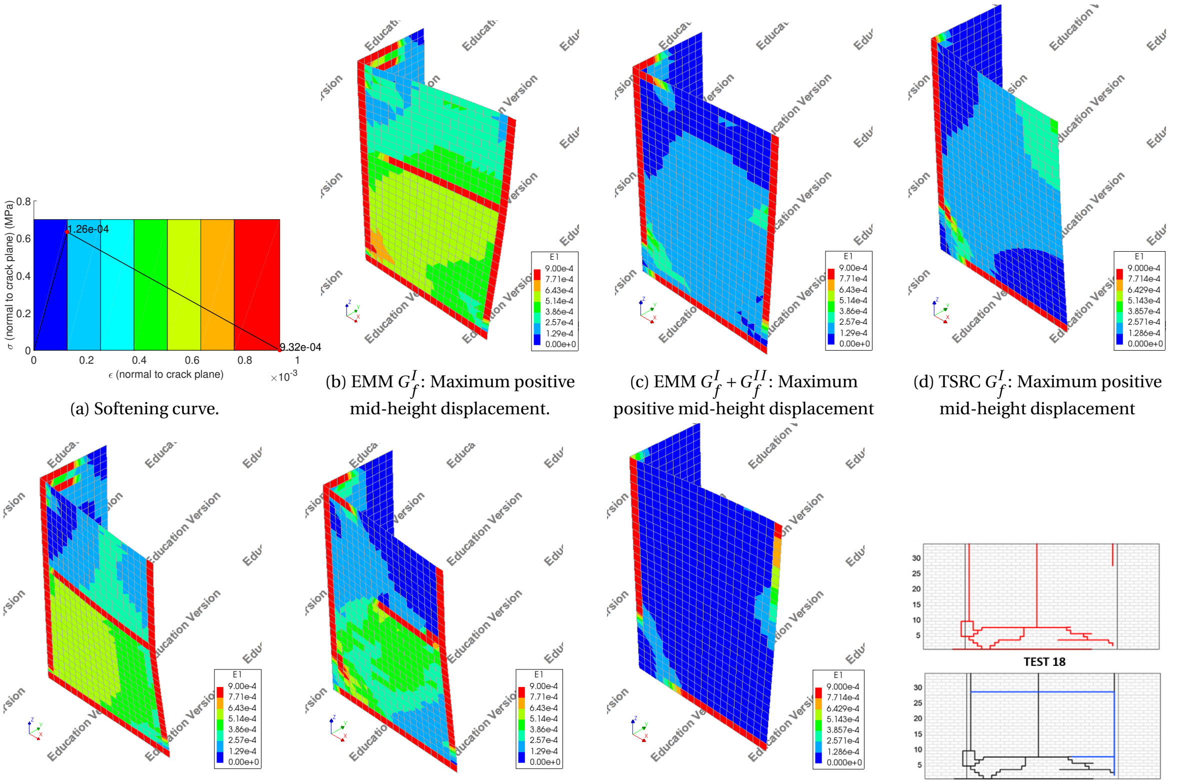

(a) Softening curve.

(b) EMM G_f^I: Maximum positive mid-height displacement.

(c) EMM $G_f^I + G_f^{II}$: Maximum positive mid-height displacement

(d) TSRC G_f^I: Maximum positive mid-height displacement

(e) EMM G_f^I: Maximum negative mid-height displacement

(f) EMM $G_f^I + G_f^{II}$: Maximum negative mid-height displacement

(g) TSRC G_f^I: Maximum negative mid-height displacement

(h) Experiment.

Figure 5.34: CS-000-RF (Set-1 parameter): Principal strain plot at the peak positive and negative displacement direction. Absolute deformation scale 5

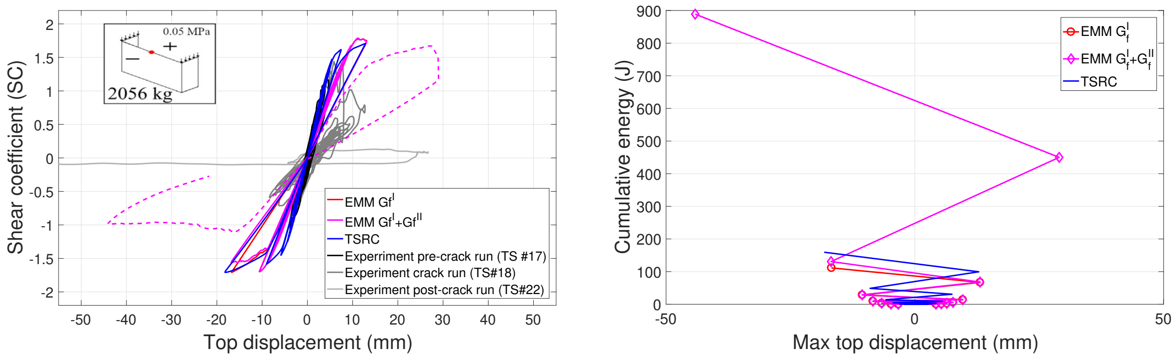

(a) Shear coefficient vs mid-height displacement.

(b) Energy vs max mid-height displacement.

Figure 5.35: CS-000-RF (Set-2 parameters): (a) Hysteretic response, and (b) Energy dissipation

5.5. Conclusions

In this chapter, the numerical results of the analysis are presented for the specimens having restrained at the top with pre-compression load (CS-005-RR) and without any top restrain (CS-000-RF) for different loadings. The outcomes of the results are presented for different material models are compared with the experimental results. The comparison is made in terms of shear coefficient vs displacement and cracks pattern. Based on the outcomes following reasons can be drawn:

- Non-linear static analysis with Uniform loading:
  - For both the wall configurations, the initial stiffness found from numerical results are close to the undamaged experiment hysteresis cycles. Furthermore, the force capacity of numerical outcomes

is higher than the experiment. This is primarily due to the application of load, as in static analysis load is applied in increments in one direction (either positive or negative displacement direction).

  – The crack pattern of the wall restrained on four sides does not resemble that of an experiment. Referring to the Figure 2.8, the primary reason being the top support condition. Furthermore, this is verified with the deformed shape of the numerical results with the experiment (Figure 5.6). Whereas, wall restrained on three sides shows closeness in a crack pattern using engineering masonry model (EMM) with experiment as compared to total strain crack (TSRC) model.
  – Both wall configurations have sufficient displacement capacity to uniform static load (more than wall thickness), and the force-displacement curve (for EMM) can be idealized into a trilinear curve as stated in Figure 2.11.

- Non-linear static analysis with Mode-proportional loading: To access the behaviour of walls subjected to mode proportional loading, the material sensitivity analysis is performed. For wall restrained on four sides, mode-I fracture energy is increased by five times. While for wall restrained on three sides in addition to mode-I, Young's modulus, mode-II fracture energy is needed to be calibrated. Based on the outcomes, both the wall does not have sufficient displacement and show snap-back behaviour in response.
- Non-linear time history analysis:
  – In both the wall configurations, the pre-crack parameters in EMM are matching with experimental outcomes. These parameters are stiffness, peak shear coefficient, and maximum displacement. While the crack and post-crack run differ significantly.
  – The peak forces both in positive and negative displacement are within the 20% difference but the displacement capacity is underestimated. This underestimation is because of the fewer cracks are opened which could able to dissipate the energy hence the displacement behaviour can not be captured. However, on changing the top boundary condition, initiation of cracks in the diagonal pattern is observed in the crack runs contour plots but not fully open. Moreover, crack along the bottom support is fully formed. This is reasoned to be due to the exclusion of the time signal which could cause further dissipation in the model.
  – For the wall restrained on three sides, the difference in the two material behaviours can be observed in both hysteresis response and crack patterns. In crack and post-crack run, using TSRC gives non-convergent solution and top displacement is overestimated. In EMM, the crack patterns in the wall-pier connection match with the experiment. However, in the post-crack run, the response is stiff and due to no dissipation of energy, no further cracks open.
- non-linear cyclic analysis:
  – The cyclic analysis with increasing load magnitude both in positive and negative direction was carried out in addition to the parameter sensitivity study of fracture energy in cracking and shearing on the failure mechanism. The response observed in EMM is better than the TSRC material model based on the hysteresis curves, energy dissipation plots and crack pattern in the wall. The difference in both the material properties is primarily due to different definition of shear behaviour and the orthogonality in material properties in EMM.
  – The contribution of shear behaviour in dissipating the energy is found only when the wall displaces with higher magnitude. Since, in the wall restrained on four sides, the contribution of energy dissipation of shear is negligible, whereas, in the wall restrained on three sides, the onset of cracking, the energy is dissipated in both shears and tension.

6

Discussion and Conclusions

Introduction

Unreinforced masonry (URM) buildings are vulnerable when subjected to out-of-plane dynamic loading, especially under earthquakes. In the masonry building structures, the two-way spanning wall restrained on four and three sides are the most commonly found wall configuration. If the wall is load-bearing, out-of-plane failure to these walls frequently leads to the partial or global collapse in the URM building structures. Due to the higher seismic vulnerability of the one-way spanning wall in the out-of-plane direction, very limited research focuses on the two-way spanning wall that was carried out in the past. Therefore, in this thesis work, the use of a numerical analysis method is adopted to validate the numerical results with the outcomes of the case study performed on four sides and three sides restrained wall.

The following chapter contains the discussion of the results for the wall restrained on four sides, and the wall restrained on three sides based on the numerical analysis. The chapter is divided into five parts — the first three sections belonging to the three research objectives of this thesis (chapter 1). The first section of the chapter compares the results obtained with the two continuum material model, namely the engineering masonry model (EMM), which is an orthotropic material model and total strain rotating crack (TSRC) model, which is an isotropic model. In the second section, discussion based on the influence of different top boundary conditions is made, including related modeling choices. In the third section, the effect of different loading conditions on each wall configuration is discussed. Based on the discussion presented in the three-section conclusion have been drawn, and future recommendations are given.

6.1. Continuum isotropic and orthotropic material model

In this section, the thesis objective related to the comparison of isotropic (total strain rotating crack, TSRC) and orthotropic (engineering masonry model, EMM) material models is addressed to quantify their applicability in evaluating the behavior of two-way spanning unreinforced masonry walls.

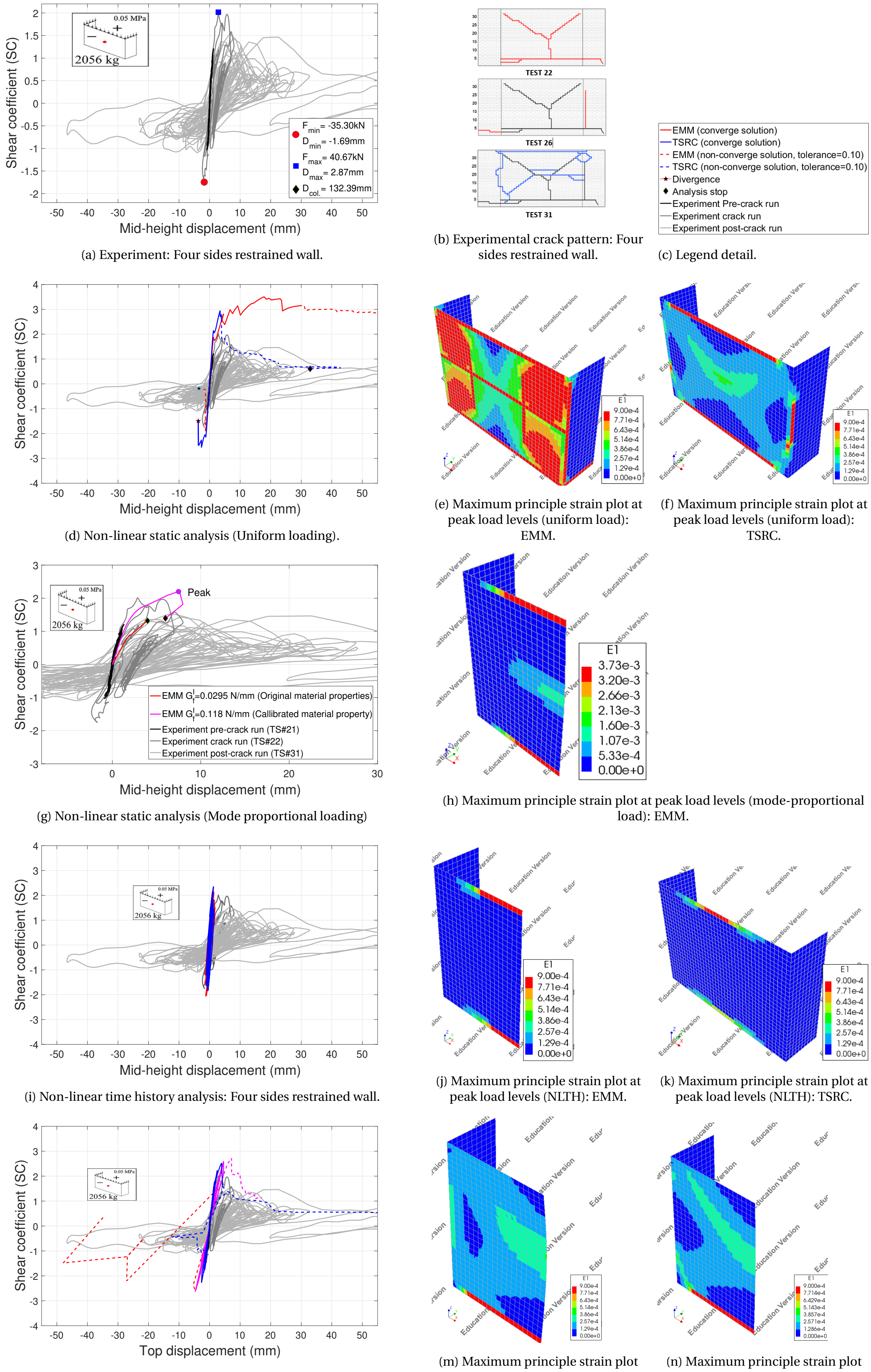

(a) Experiment: Four sides restrained wall.

(b) Experimental crack pattern: Four sides restrained wall.

(c) Legend detail.

(d) Non-linear static analysis (Uniform loading).

(e) Maximum principle strain plot at peak load levels (uniform load): EMM.

(f) Maximum principle strain plot at peak load levels (uniform load): TSRC.

(g) Non-linear static analysis (Mode proportional loading)

(h) Maximum principle strain plot at peak load levels (mode-proportional load): EMM.

(i) Non-linear time history analysis: Four sides restrained wall.

(j) Maximum principle strain plot at peak load levels (NLTH): EMM.

(k) Maximum principle strain plot at peak load levels (NLTH): TSRC.

(l) Non-linear cyclic analysis: Four sides restrained wall.

(m) Maximum principle strain plot (Non-linear cyclic analysis:) EMM.

(n) Maximum principle strain plot (Non-linear cyclic analysis): TSRC.

Figure 6.1: Shear coefficient vs displacement curve for four sides restrained wall with overburden load for different loading.

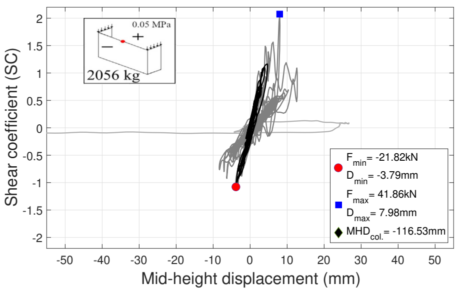

(a) Experiment: Four sides restrained wall.

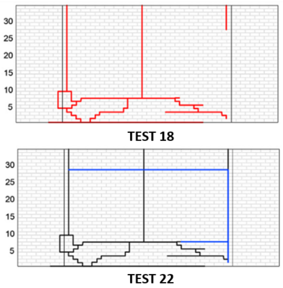

(b) Crack pattern: Experiment.

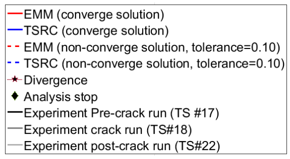

(c) Legends.

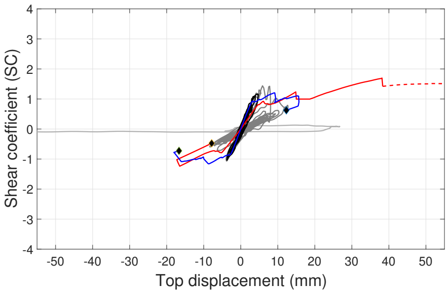

(d) Non-linear static analysis (Uniform loading): Three sides restrained wall.

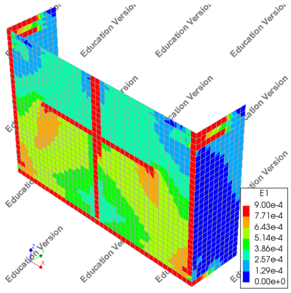

(e) Maximum principal strain plot: Non-linear static analysis (Uniform loading): EMM.

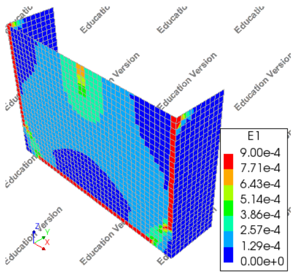

(f) Maximum principal strain plot: Non-linear static analysis (Uniform loading): TSRC.

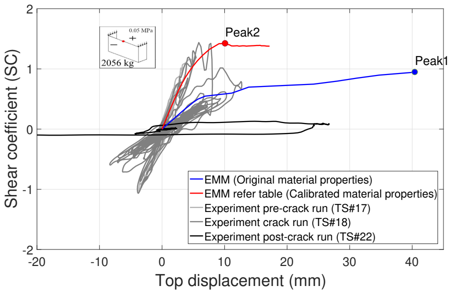

(g) Non-linear static analysis (mode proportional load).

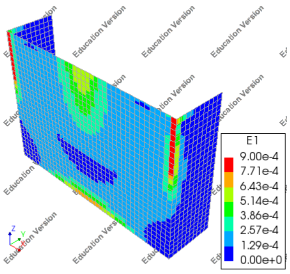

(h) Maximum principal strain plot: Non-linear static analysis (mode proportional load):EMM.

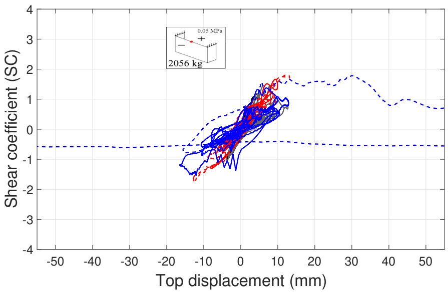

(i) Non-linear time history analysis: Three sides restrained wall.

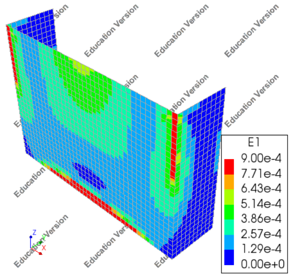

(j) Maximum principal strain plot: (NLTH): EMM.

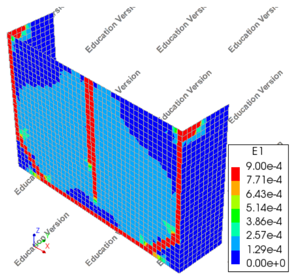

(k) Maximum principal strain plot: (NLTH): TSRC.

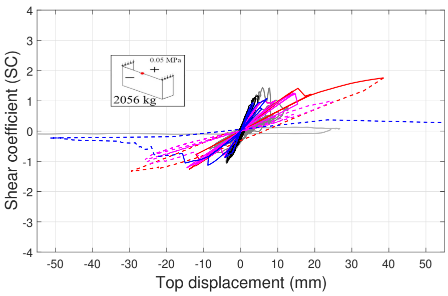

(l) Non-linear cyclic analysis: Three sides restrained wall.

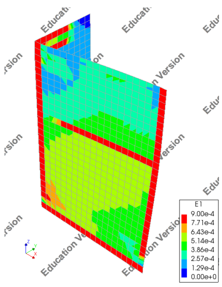

(m) Maximum principal strain plot: (Non-linear cyclic analysis): EMM.

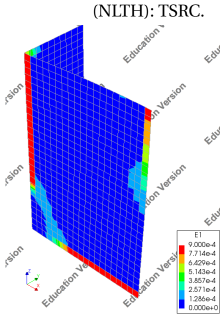

(n) Maximum principal strain plot: (Non-linear cyclic analysis): TSRC.

Figure 6.2: Shear coefficient vs displacement curve for three sides restrained wall without overburden load for different loading.

- In TSRC, the material is considered as isotropic and based on the coaxial stress-strain concept. According to which, stress and stress are evaluated in the principal directions of the strain vector. The shear behavior in out-of-plane is define using the retention factor, i.e., as the integration point cracked, the shear stiffness reduced for a user-defined factor (taken as 0.2 in the present study). Furthermore, the shear behavior is independent of the pre-compression as in masonry. Therefore, after reaching the peak load, the load capacity plummets by more than 50% of the peak load for wall restrained on four sides, and snapback is observed in three sides restrained wall.

- In EMM, the material is considered as an orthotropic material. The stress-strain is evaluated in the direction perpendicular and parallel to the bed-joint. The shear behavior is based on the Coulomb friction law, which depends on the pre-compression load. Therefore, both the wall specimen shows enough displacement capacity well beyond the peak load capacity is reached in uniform static loading. However, after peak load, the non-convergence in the force norm is obtained, and the solution stops manually after reaching displacement greater than wall thickness.

- Both EMM and TSRC represent the initial linear state, i.e., before crack and non-linearity in both the wall configurations. The substantial difference in both the material model is observed after the crack is initiated in the wall. For the wall restrained on four sides, the majority of the wall elements are cracked in the bed-joint direction and head-joint direction at the wall-pier connection, as seen from the principle strain plot in Figure 6.1e. Whereas in the three sides restrained wall, the majority of cracks are located at the wall bottom (bed-joint), wall-pier connection (head-joint), and vertical crack in the main wall (head-joint) as shown in Figure 6.2e.

- In the non-linear time history analysis (NLTH) for wall restrained on four sides, the difference in two material models can not be made as the cracks are initiated in the limited elements. Due to this limited crack initiation, the energy dissipation due to loading and unloading can not occur; as a result, the response observed is very stiff, and maximum displacement reached in both positive and negative displacement direction is less than the experiment.

- Using EMM for the wall restrained on three sides, the NLTH analysis is stable, like initiation, and progress of crack resembles that of an experimental crack pattern. While using TSRC, the solution becomes non-convergent in crack and post-crack run. Since none of the element exceeds in compression, the significant difference between both the material model lies in the evaluation of stress-strain in bed-joint and head-joint direction and out-of-plane shear. On the formation of a vertical crack in the wall-pier connection and the main wall, EMM possesses an additional residual material strength capacity in bed-joint tension and out-of-plane shear.

- The contribution of mode-II fracture energy in total energy dissipation in the cyclic analysis is significantly visible for three side restrained wall. It is because No pre-compression load is applied on the wall; therefore, the maximum shear strength capacity of the element is less than elements with the pre-compression load. Hence for the same out-of-plane shear strain level, three sides restrained wall reached in cohesion softening, while wall restrained on four sides remains in a linear zone (Figure 6.3).

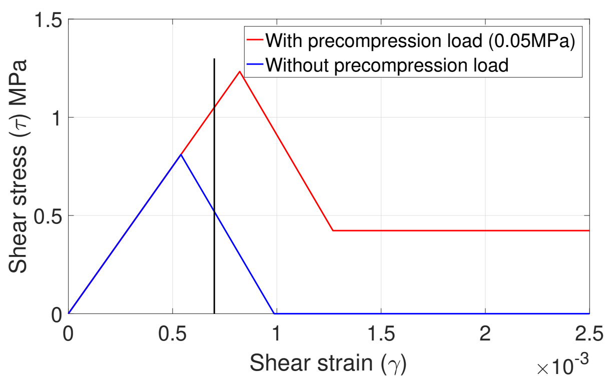

Figure 6.3: Shear behaviour in element of the wall with or without pre-compression load.

- During unloading and reloading, the cracks closed and open, which in turn dissipates energy and, therefore, require a less external force to reach the same level of displacement under cyclic loading. Cyclic analysis, keeping the same material properties, the energy dissipation found using EMM is higher as compared to the TSRC material model. Furthermore, the maximum displacement reached in each cyclic loading using EMM is higher (Figure 6.4b).
- Based on the discussion presented in the previous section, the engineering masonry model (EMM) is better in simulating the behavior of masonry walls. Therefore, in section onwards, the focus of the discussion will be on the results using EMM.

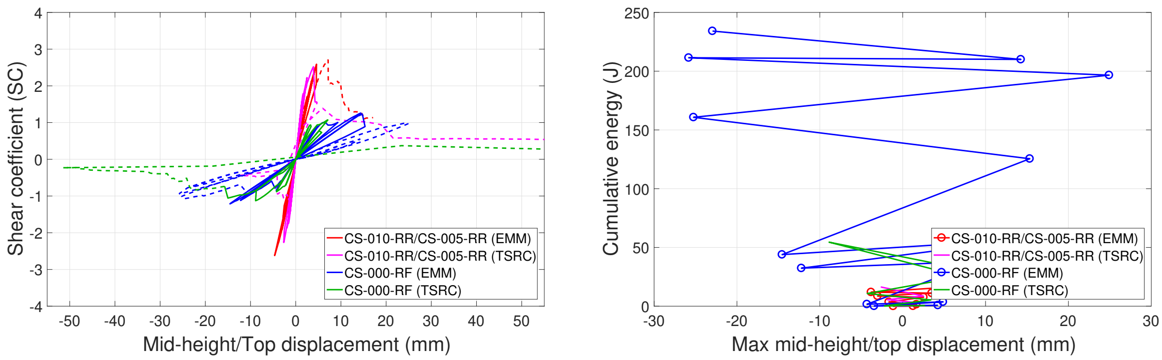

(a) Shear coefficient vs mid-height displacement.

(b) Energy vs max mid-height displacement.

Figure 6.4: Combine (Set-1 parameters): (a) Hysteretic response, and (b) Energy dissipation.

6.2. Influence of boundary conditions

In this section, the discussion of results based on the boundary condition is presented. The results of the wall restrained on four sides with overburden load and wall restrained on three sides without overburden are compared for different types of loading conditions. The results of all the analyses are presented in Figure 6.1 and Figure 6.2.

Material model	Parameter	Four sides restrained wall	Three sides restrained wall
EMM	F_{max} +/- (kN)	70.71 / -38.17	34.23 / -24.97
	MHD/TD +/- (mm)	17.83/ -1.32	38.14 / -16.48
	MHD_{max}/TD_{max} +/- (mm)	154.53 / -3.49	128.27 / -17.27
TSRC	F_{max} +/- (kN)	59.36 / -51.47	24.29/ -23.37
	MHD/TD +/- (mm)	3.43 / -2.67	9.01 / -8.58
	MHD_{max}/TD_{max} +/- (mm)	42.74/-3.67	15.72/-18.05

Table 6.1: Comparison of Peak base shear force, displacement at peak base shear force, and maximum displacement in the wall for different boundary conditions.

- The force capacity of the wall restrained on four sides is twice that of the wall restrained on three sides. However, the out-of-plane displacement at the peak load is double in three sides restrained wall using uniform loading (Table 6.1). The increased load capacity of the four sides restrained wall is explained by the presence of vertical pre-compression and top restraint. The pre-compression enhances the out-of-plane shear strength of the wall, while the top support provides the additional support condition.
- For the wall to sustain the earthquake, the wall should have sufficient displacement capacity to prevent failure. Based on the result obtained, the wall restrained on four sides has a displacement capacity of 25mm with a fully converged solution. Non-convergence is occurred due to the exceedance of the force norm, whereas allowing the tolerance for force norm to be 0.1, the displacement capacity will be

150mm. Similarly, in the wall restrained on three sides, for the fully converged solution, maximum displacement reached is 38mm, whereas, increasing the tolerance, maximum top displacement capacity could be 112mm. The two-way spanning wall can sustain the load in the out-of-plane direction for the displacement up to twice the wall thickness, as stated in **?**]. However, based on the FE analysis result, the maximum displacement capacity reached is more than the wall thickness in both the model, but the result could not be trustable to full confidence due to non-convergence in force norm.

- The wall restrained on four sides; the response in terms of force-displacement plot is stiff for NLTH and cyclic analysis. The cracks pattern is mainly initiated along the top and bottom support, representing a bed-joint crack in the wall. However, in the case of a wall restrained on three sides, show the brittle response as degradation in the stiffness and rapidly increase in the wall displacement is noted. The cracks are initiated at the wall bottom (bed-joint crack) along with the connection between main-wall and pier (representing the head-joint crack). In three sides restrained wall, after the formation of full three vertical cracks in the main-wall, the behavior is changed to a one-way spanning wall giving rise to bed joint crack in the horizontal direction (Figure 6.2e).
- The influence of top rotation condition on the wall restrained on the four sides shows the change in the crack pattern in the main wall. A wall without top rotation restriction (EMM $\phi_{top} \neq 0$), the crack is initiated at the wall bottom support, and in the diagonal pattern. This crack pattern initiation is similar to the experimental crack pattern observe after the first crack run. Figure 6.5 shows the maximum principle strain plot from the NLTH analysis with changing top boundary conditions and compared with the experiment.

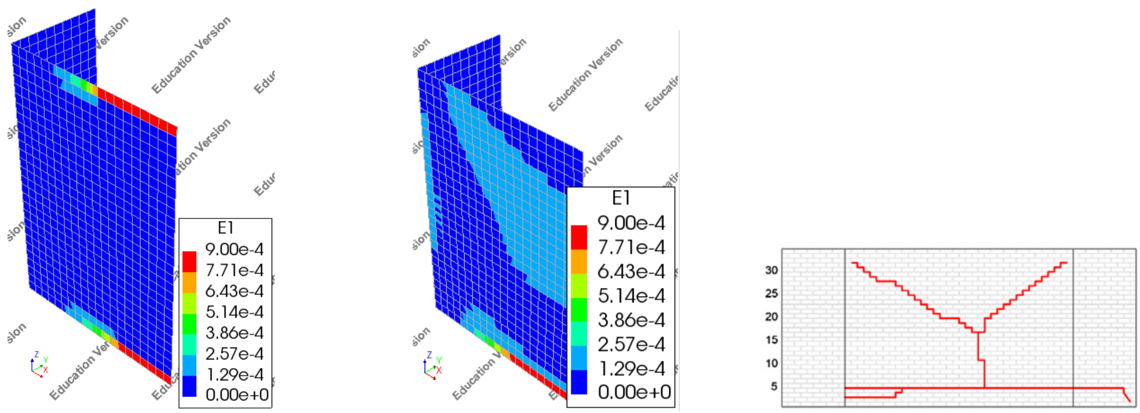

(a) $\phi_{top} = 0$. (b) $\phi_{top} \neq 0$ (c) Experiment

Figure 6.5: Maximum principal strain plot for wall restrained on four sides with changing top rotation (NLTH analysis).

6.3. Idealization of earthquake loading

In this section, the discussion of results based on the different loading conditions is compared for both the wall configurations. The first comparison based on uniform and mode-proportional loading (in non-linear static analysis) is carried out. Second, non-linear static and non-linear time history analysis are compared. Finally, the comparison based on non-linear static vs. non-linear cyclic analysis is discussed.

6.3.1. Non-linear static analysis: uniform vs mode proportional loading

The result of the non-linear static analysis with different load patterns on the main wall shows that the non-linearity in the analysis based on mode-proportional loading occurs for a lower displacement than for the analysis with the uniformly applied load. Because a load of higher magnitude is applied in the center for CS-005-RR and top of the main wall in CS-000-RF in mode proportional loading, this load pattern initiated the degradation of the material at lower displacement at the location where a load of higher magnitude is applied. The material sensitivity study is performed (section 5.2) to calibrate the force-displacement behavior as close to the experiment output for initial stiffness and peak SC. The response in terms of force-displacement is shown in Figure 6.6a and Figure 6.6b for wall restrained on four sides and wall restrained on three sides, respectively. Based on the response, it can be stated that the static analysis with mode proportional loading

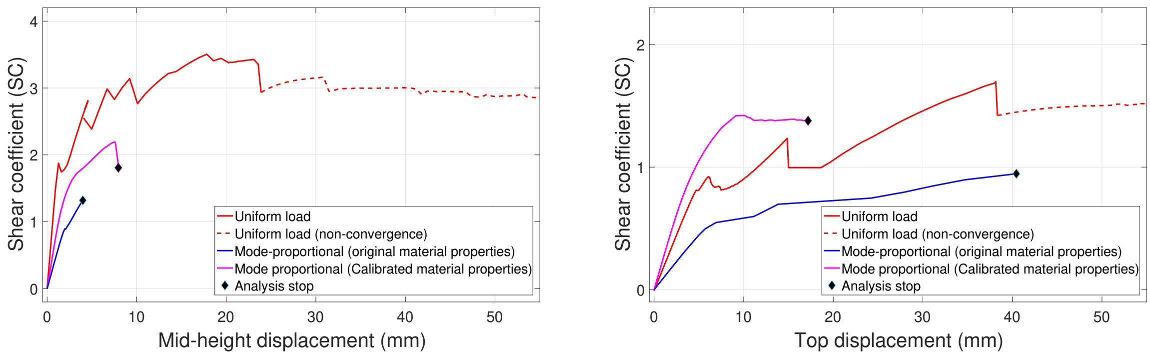

(a) Wall restrained on four sides

(b) Wall restrained on three sides

Figure 6.6: Shear coefficient vs mid height displacement curve: static uniform loading vs static mode proportional load analysis.

gives conservative results in terms of both force and displacement capacity. Therefore, analysis with uniformly applied load is more appropriate for evaluating seismic behavior.

6.3.2. Non-linear static analysis vs Non-linear time history analysis

On comparing the static vs. non-linear time history analysis, the maximum force capacity of the wall restrained on four sides is similar in both positive and negative displacement direction (Figure 6.7) whereas, maximum mid-displacement obtained from NLTH analysis is small. The positive displacement direction is when the wall's out-of-plane displacement is in the pier direction, whereas negative displacement direction when the wall moves away from the pier. Since in the few elements, cracks are opened, which are insufficient to dissipate the energy. However, the crack pattern is similar in the analysis, either using full or short-time signals and not resembling that of an experiment if the boundary condition kept similar to the experimentally specified. Moreover, the response shows wall response is stiff, and wall mid-height displacement is under $\pm$5mm (Figure 6.7). Allowing the top rotation in the four sides restrained wall in the horizontal direction gives much better results is the crack pattern for the short time signal (Figure 6.5).

In the case of wall restrained on three sides, the NLTH analysis shows a wall exhibit higher displacement capacity (Figure 6.8) compared to the wall restrained on four sides. The force capacity using either short or long-time signal is comparable in positive displacement direction and in the negative displacement direction. However, the displacement obtained using the short-time signal is underestimated. Using the long-time signal, the wall exhibit displacement capacity more than the wall thickness (Figure 6.8).

6.3.3. Non-linear static analysis vs non-linear cyclic analysis

The response of the non-linear static analysis and the cyclic analysis are shown in Figure 6.9 and Figure 6.10 for wall restrained on four and three sides respectively using the same material properties. Using the TSRC material model, the non-linear static analysis formed the backbone curve of the hysteresis curves of non-linear cyclic analysis nicely, which is not the case with EMM.

For the wall restrained on three sides, the crack obtained either of the analysis is similar in the formation stage as well as at the peak load. After the formation of vertical cracks, the horizontal crack in the main wall is initiated. Similarly, in the wall restrained on four sides, with similar top support conditions, the crack initiation is the same. Furthermore, under static analysis, the displacement capacity obtained is higher as compared to the cyclic analysis in both the wall configurations. This is primarily due to the application of monotonic increasing load in the static analysis while varying cyclic load in the other.

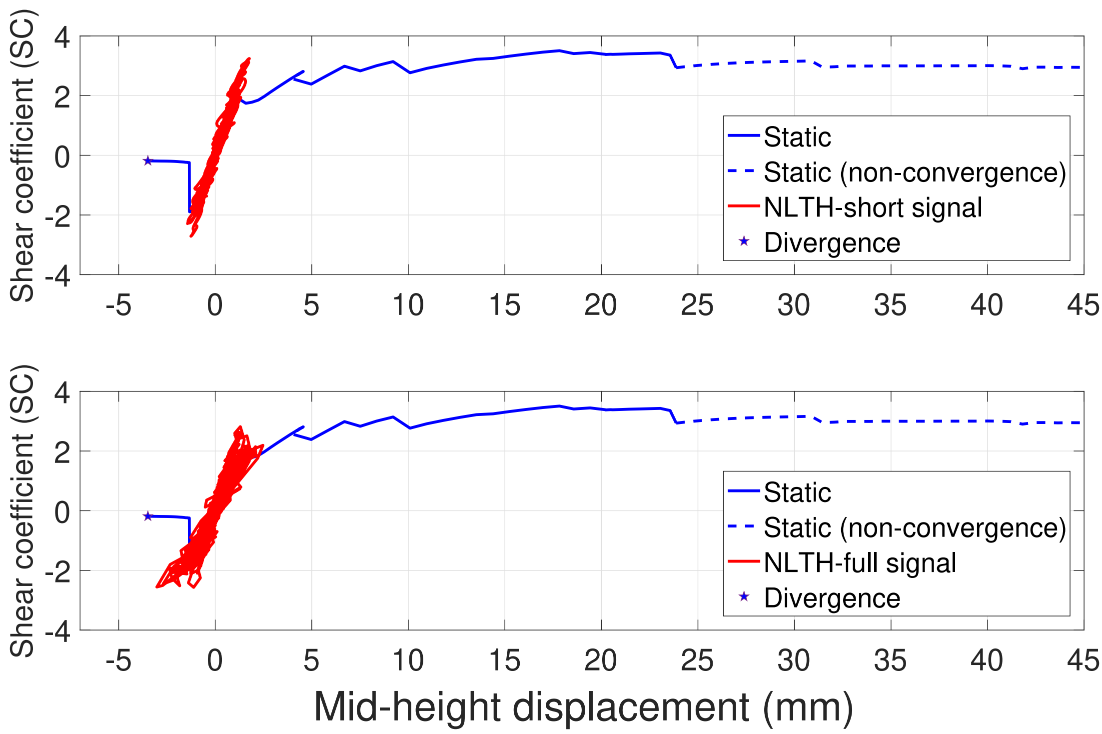

Figure 6.7: Shear coefficient vs mid height displacement curve wall restrained on four sides: comparision of Non-linear static vs NLTH.

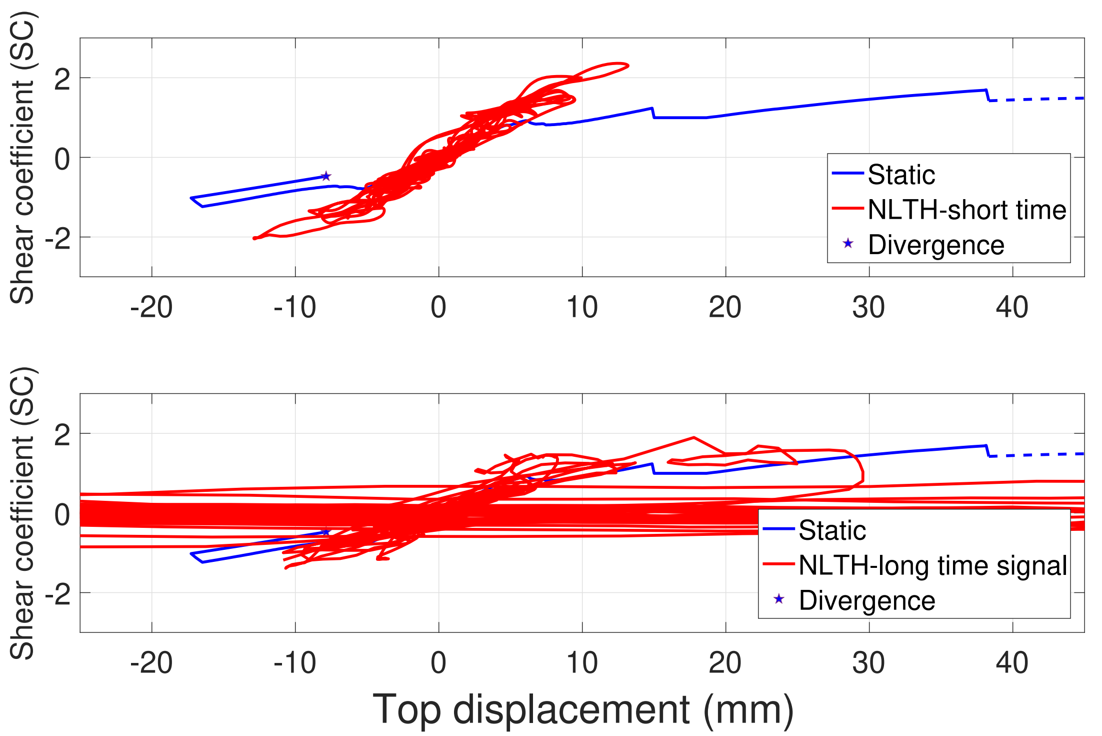

Figure 6.8: Shear coefficient vs mid height displacement curve for wall restrained on three sides: comparison of Non-linear static vs NLTH.

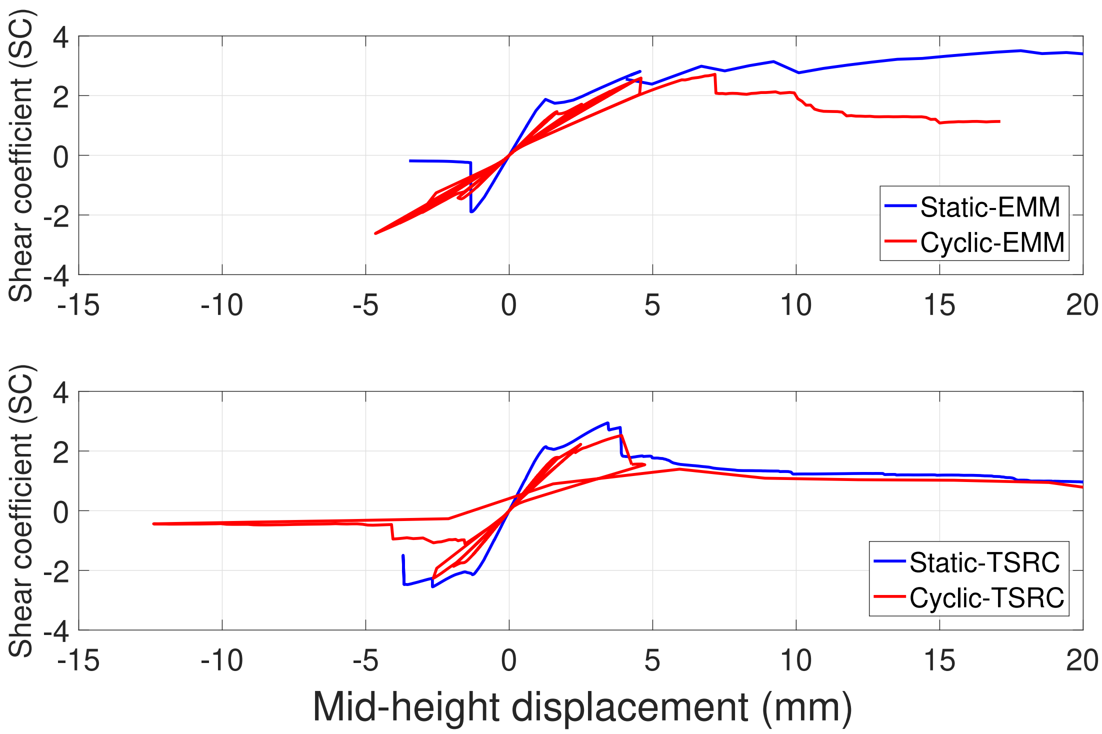

Figure 6.9: Shear coefficient vs mid height displacement curve for wall restrained on four sides: non-linear static vs cyclic analysis.

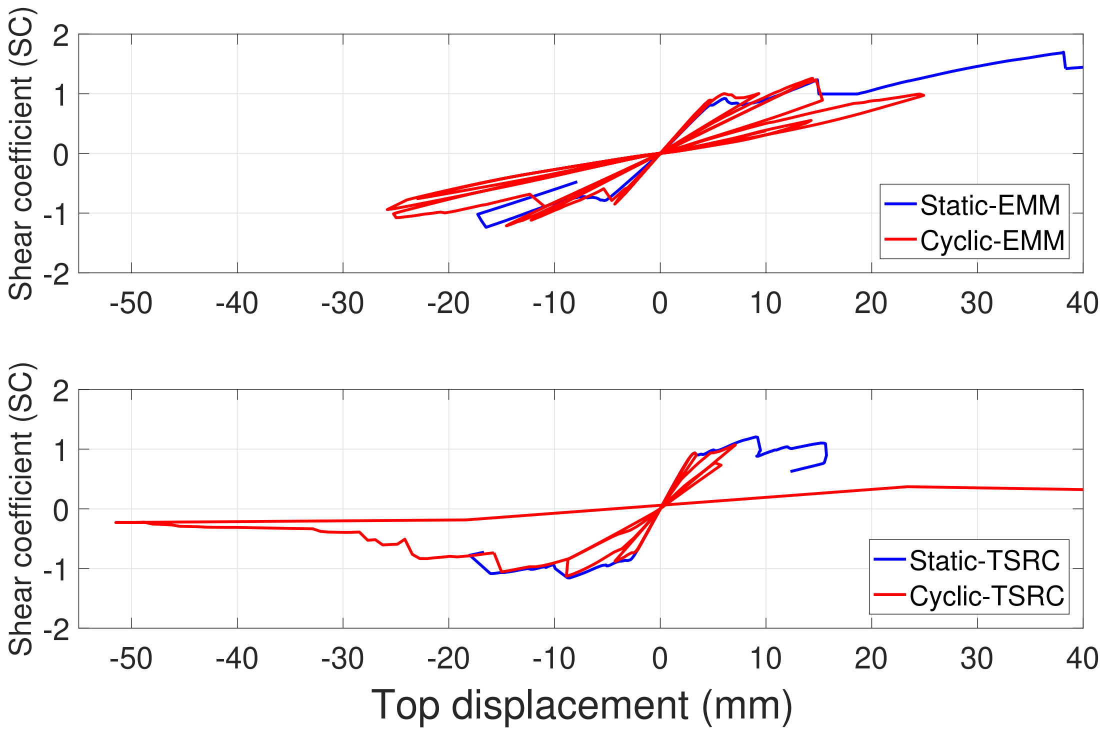

Figure 6.10: Shear coefficient vs mid height displacement curve for wall restrained on three sides: non-linear static vs cyclic analysis.

6.4. Conclusions

In this section, the conclusions are drawn to answer the research questions based on the discussion presented in the previous section. The main research question is how to predict the seismic behavior of two

-way spanning walls based on the application of different out-of-plane loadings? In this respect, the evaluation of orthotropic and isotropic material models to consider cracking/failure of masonry is studied for the wall of different top boundary conditions. This includes four sides restrained wall with top overburden load, and three sides restrained wall without overburden load. The response of both the walls is studied for four types of load applications. The outcome of the results is discussed in terms of force-displacement and crack pattern plots. Based on the results reported in the previous sections, the following conclusions are drawn:

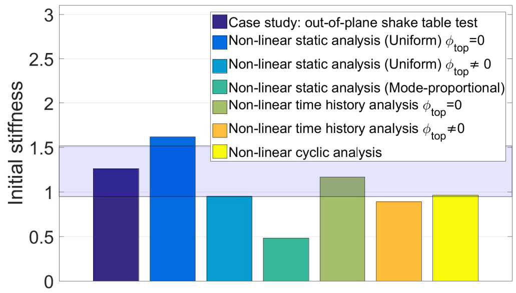

(a) Four sides restrained wall: Initial stiffness.

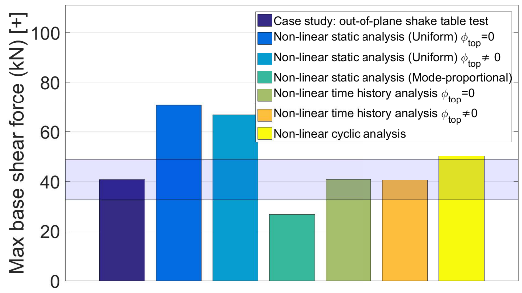

(b) Four sides restrained wall: Maximum base shear force.

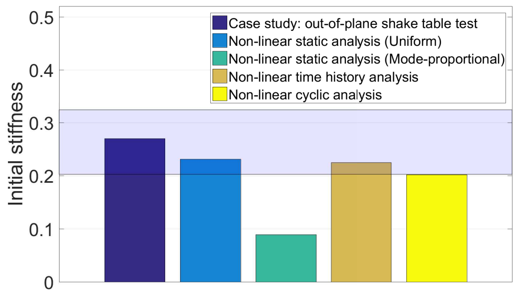

(c) Three sides restrained wall: Initial stiffness.

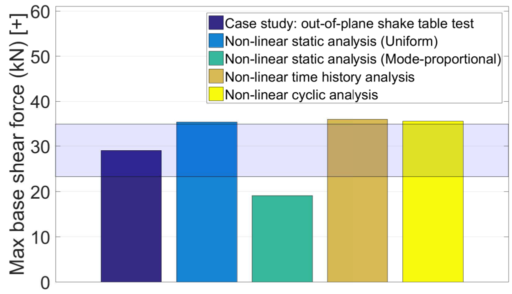

(d) Three sides restrained wall: Maximum base shear force.

Figure 6.11: Comparison of initial stiffness, and peak load from experiment with numerical analysis using different load application and top boundary conditions. The bandwidth of 20% difference is shown in the above figure.

- Irrespective of the type of loading, the orthotropic material model (engineering masonry model, EMM) gives a better response of a two-way spanning wall in out-of-plane loading. However, the boundary conditions have a significant influence on the crack initiation and propagation in the wall. The crack pattern observed using the isotropic material model (total strain rotating crack, TSRC) shows the wall replicating the behavior of a plate loaded perpendicular to the plane and restrained on four sides. Therefore, considering the masonry as an isotropic material is a limitation of the TSRC material model.
- The difference in the force-displacement response between both orthotropic (EMM) and isotropic (TSRC) material model is primarily visible at the onset of non-linearity (cracking). The response (in non-linear static analysis) using EMM shows a two-way spanning wall has sufficient displacement capacity (larger than wall thickness) while maintaining the relative constant load in the post-peak region. In a two-way spanning wall, the additional displacement capacity (beyond wall thickness) obtained from the out-of-plane shear resistance along the already formed vertical crack.
- In two-way spanning walls, both the peak load and initial stiffness of the walls is enhanced by higher pre-compression and top lateral support. It is found in both experimentally and numerically (Figure 6.11a, c) as pre-compression increases flexural and shear resistance capacity of the wall to resist the out-of-plane load. Furthermore, the walls demonstrate a considerable degree of ductility in the region of a peak load (observed in non-linear static analysis) and considered to be beneficial for the wall to sustain an earthquake. This ductility is due to the rotational restraint along the vertical edge to carry the out-of-plane load.
- Wall restrained on three sides; the cracks are initiated at the wall-pier junction due to the exceedance of head-joint tension. This crack propagation changes the behavior of two-way to one-way in the wall.

While the wall restrained on four sides (no top rotation fixity), the crack is initiated in the bed joint and a diagonal pattern and later formed at the wall-pier junction. As a result, four sides restrained wall can maintain the two-way bending behavior for the higher loads. However, in the wall restrained on four sides, the influence of top rotation fixity shows the failure pattern changes significantly. Therefore, it is important to know the proper boundary condition in the wall to help in identifying the weakest link and suggest the necessary strengthening location.

- The base shear capacity of a two-way spanning wall under the application of non-linear static analysis with uniform loading is higher compared to the outcomes of the other types of loading (Figure 6.11b, d). Although it was not possible to find full convergence in the analysis, the results with higher tolerance give a reasonable estimate of wall displacement capacity. NLTH analysis is not able to approximate the dynamic behavior of a two-way spanning wall, even incorporating the full-time signal. Therefore, restricting the NLTH analysis for the part of the signal where significant damage in the wall occurs gives a fair indication about the dynamic behavior of the wall and save computational time.

- Under the application of different loading, for the same material parameters, the initial stiffness mainly depends on the type of load application and top support. Referring to Figure 6.11a, b, the initial stiffness of the non-linear static analysis with mode proportional loading is significantly less due to large magnitude of the load is applied at the wall mid-height (in four sides restrained wall) and wall top (in three sides restrained wall) based on mode shape. However, for other loadings (such as non-linear static analysis with uniform loading, NLTH, and cyclic loading) application, the stiffness varies within the 20% difference as that of an experiment.

- The contribution of mode-II fracture energy is studied in cyclic analysis shows the wall without pre-compression load and restraint on three sides dissipates energy both in tension and due to cohesion softening. While the pre-compression in four sides restrained the wall increases the shear capacity; as a result, the contribution of shear in overall energy dissipation is negligible.

- In non-linear time history analysis, both the material models underestimate the degradation of material with time for the wall restrained on four sides. Moreover, incorporating the full length of time signal sequentially in the NLTH analysis could not capture the response as obtained experimentally. However, overestimation (force and displacement) in the response for the wall restrained on three sides, as significant degradations and complete failure is found using complete time history. Nonetheless, both the material model is useful in reasonably predicting the response up to pre-crack. Hence, performing NLTH analysis can not capture the dynamic response of the walls, either using EMM and TSRC material models. It is reasoned to be the limitation of the available material model to capture the non-linearity under dynamic loading and could need improvement. Therefore, as a substitute for NLTH analysis, the response of the wall using cyclic loading can be used to understanding the dynamic behavior.

- The two-way spanning wall shows an asymmetric response in positive and negative displacement direction. The wall is relatively weak in the negative displacement direction; as a consequence, the wall has a lower displacement capacity and base shear capacity.

6.5. Recommendations

Based on the thesis outcomes and the conclusions, further research on the two-way spanning wall based on modeling, material model, wall configurations are formulated:

- The use engineering masonry model for the 3-D continuum element. This could help in better understanding of out-of-plane behaviour.

- The use of micro-modeling (either using 3D solid elements and shell elements) can be considered for a better understanding of the crack evaluation in the different components such as brick and concrete (Figure 6.12a).

    - Modelling brick, mortar, and the interface between brick-mortar as a separate element as this could help in understanding the slipping and crack opening behavior at the corner i.e. main-wall and pier connection.

  - Simplified micro-modeling could be an alternative, where all non-linearity originate from mortar and brick-mortar interface are concentrated at the interface, and brick size is increased to accommodate the mortar thickness.

- Implementing different anisotropy models to investigate the out-of-plane response of masonry, such as the Rankine-Hill-Anisotropic model(Figure 6.12b) to model different strength and softening in the orthogonal direction. It is comprising of an anisotropic Rankine yield criterion combined with an anisotropic Hill criterion for compression.

- Combination of different vertical support condition such wall connected with a column on one-side and pier on the other vertical end, or wall intersecting with a transverse partition wall (Figure 6.12c).

- High strain rate loads characterize the dynamic load, therefore, strain rate dependence in the constitutive modeling of the material could be explored for NLTH analysis (Figure 6.12d). Although, this may be more relevant for the impact or blast loading rather than earthquake loading.

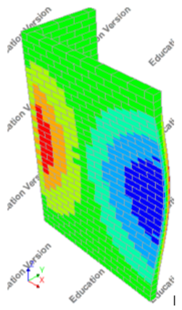

(a) Micro-modelling approach.

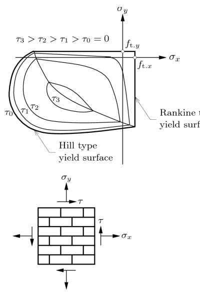

(b) Rankine based anisotropy model [?].

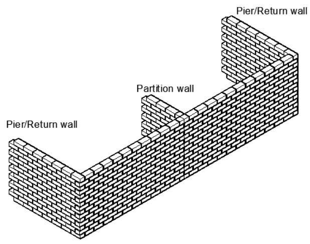

(c) Partition wall.

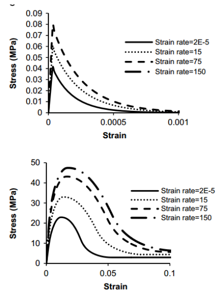

(d) Strain rate dependent material behaviour [?]. tension at top and compression at bottom

Figure 6.12: Recommendation for future work based on the research work carried out in this report.

A

Appendix-A

The following part is taken from the Lecture note of course CT 4140: Structural Dynamics (Part 1 - Structural vibrations) [?]. The equation of motion of block foundation (Figure A.1) with three degrees of freedom using displacement method.

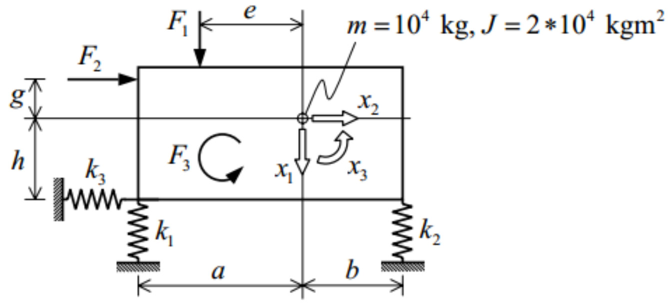

Figure A.1: In plane diagram of foundation block with three degrees of freedom.

For the equation of motion, the elements of the stiffness matrix can be found directly from the displacement method. In these method, the structure is displaced in 'n' different positions separately to identified the related load acting on it at each displacement. In the current case, the foundation block have three degrees of freedom, therefore the action of the three different displacement in three different direction and the corresponding force due to spring is shown in Figure A.2.

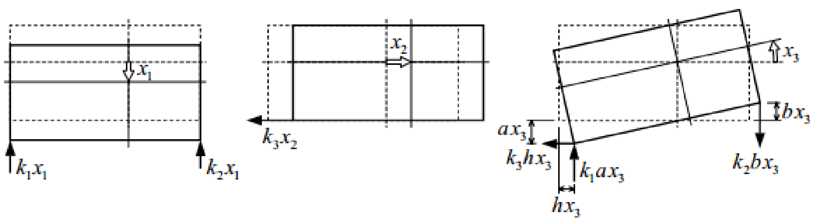

Figure A.2: Displacement of foundation block and the spring forces for three different degrees of freedom.

Applying the Newton's second law with respect to each degree of freedom as

$$m\ddot{x}_1 = -k_1x_1 - k_2x_2 - k_1ax_3 + k_2bx_3 + F_1, \tag{A.1}$$

$$m\ddot{x}_2 = -k_3x_2 - k_3hx_3 + F_2, \tag{A.2}$$

$$J\ddot{x}_3 = -k_1x_1a + k_2x_1b - k_3x_2h - k_3hx_3h - k_1ax_1a - k_2bx_3b + F_3 + eF_1 - gF_2. \tag{A.3}$$

The above three algebraic equation can be written in the matrix notation as :

$$\begin{bmatrix} m & 0 & 0 \\ 0 & m & 0 \\ 0 & 0 & J \end{bmatrix} \begin{bmatrix} \ddot{x}_1 \\ \ddot{x}_2 \\ \ddot{x}_3 \end{bmatrix} + \begin{bmatrix} k_1 + k_2 & 0 & ak_1 - bk_2 \\ 0 & k_3 & hk_3 \\ ak_1 - bk_2 & hk_3 & a^2 k_1 + b^2 k_2 + h^2 k_3 \end{bmatrix} \begin{bmatrix} x_1 \\ x_2 \\ x_3 \end{bmatrix} = \begin{bmatrix} F_1 \\ F_2 \\ F_3 + eF_1 - gF_1 \end{bmatrix} \tag{A.4}$$

The above matrix is written symbolically as given in Equation A.5.

$$\mathbf{M}\ddot{\mathbf{x}}(t) + \mathbf{K}\mathbf{x}(t) = F \tag{A.5}$$

B

Appendix-B

B.1. Non-linear static analysis

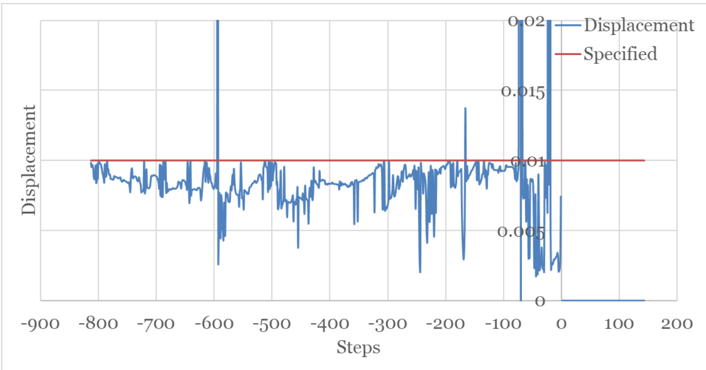

Figure B.1: Four sides restrained wall (EMM): Displacement norm.

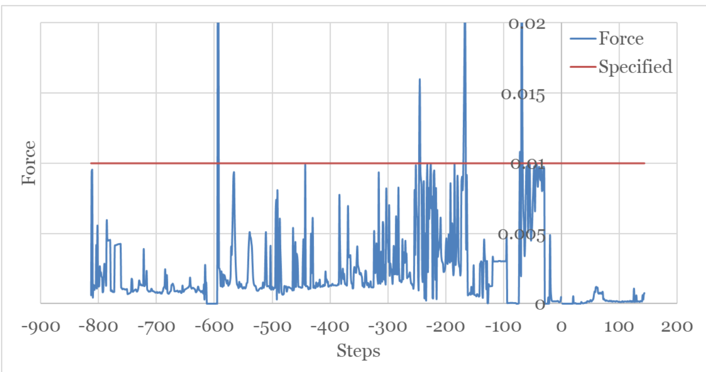

Figure B.2: Four sides restrained wall (EMM): Displacement norm.

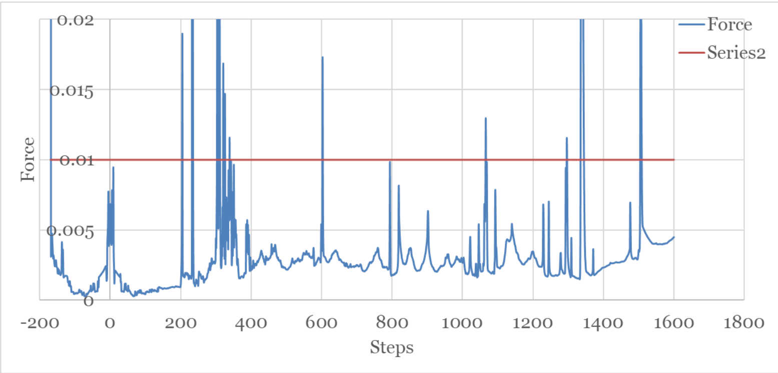

Figure B.3: Four sides restrained wall (TSRC): Displacement norm.

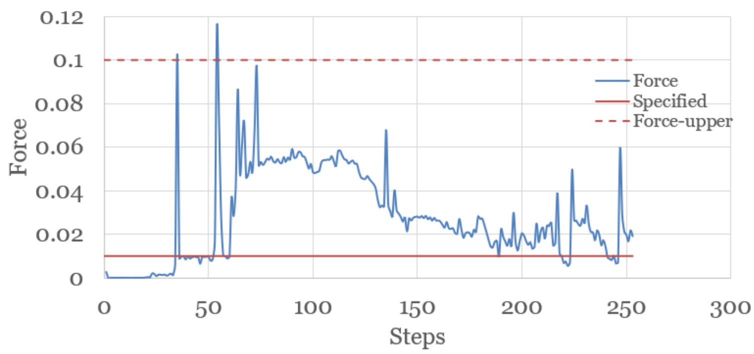

Figure B.4: Four sides restrained wall (localized element): Force norm.

B.2. Non-linear time history analysis

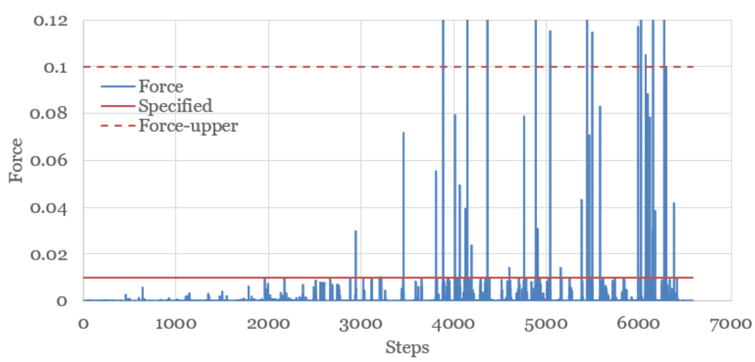

Figure B.5: Force sides restrained wall (EMM): Force norm.

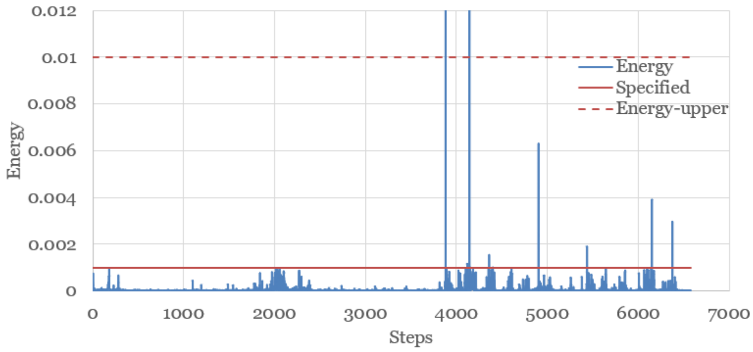

Figure B.6: Force sides restrained wall (EMM): Energy norm.

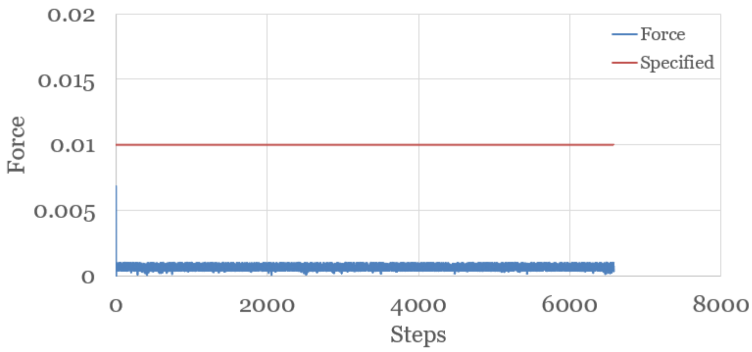

Figure B.7: Four sides restrained wall (TSRC): Energy norm.

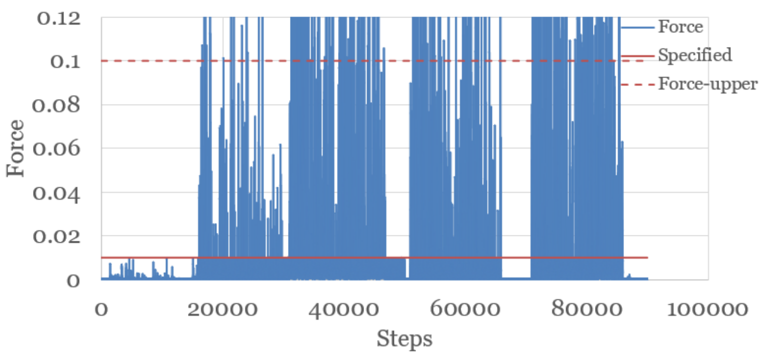

Figure B.8: Four sides restrained wall (EMM): Force norm for long time signal.

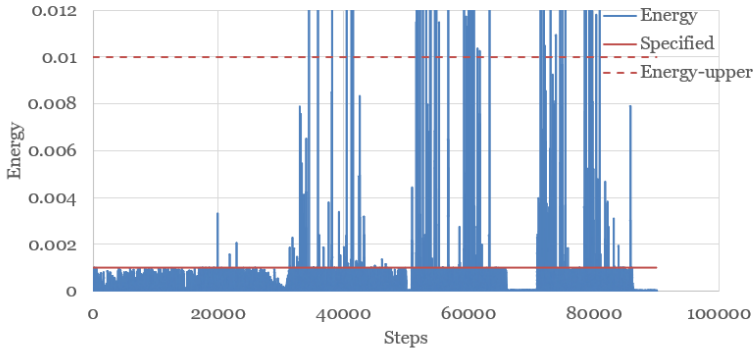

Figure B.9: Four sides restrained wall (EMM): Energy norm for long time signal.

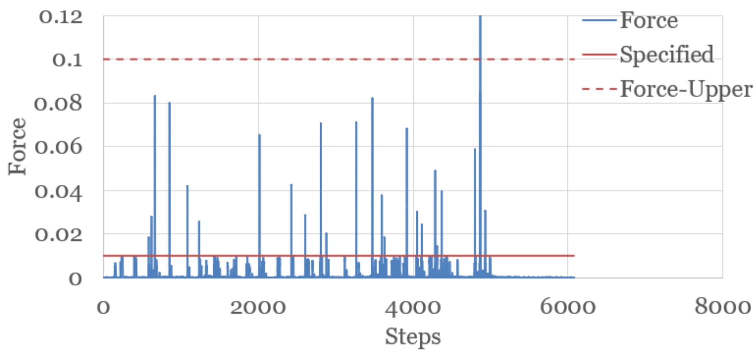

Figure B.10: Three sides restrained wall (EMM): Force norm.

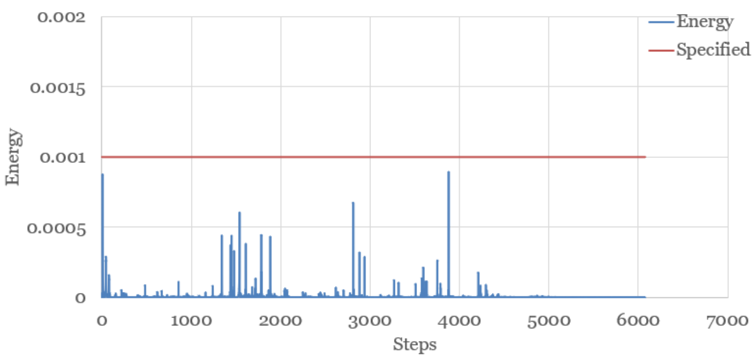

Figure B.11: Three sides restrained wall (EMM): Energy norm.

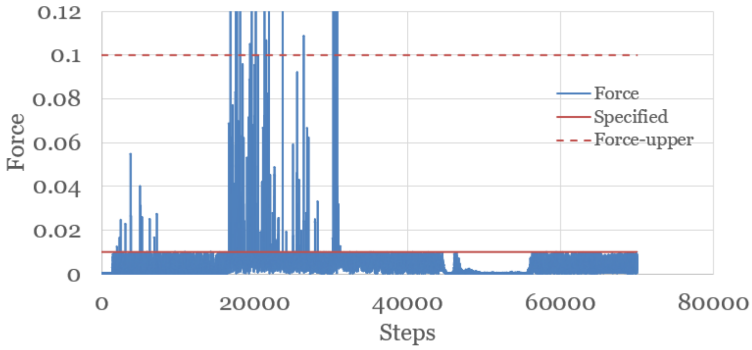

Figure B.12: Three sides restrained wall (EMM): Force norm for long time signal.

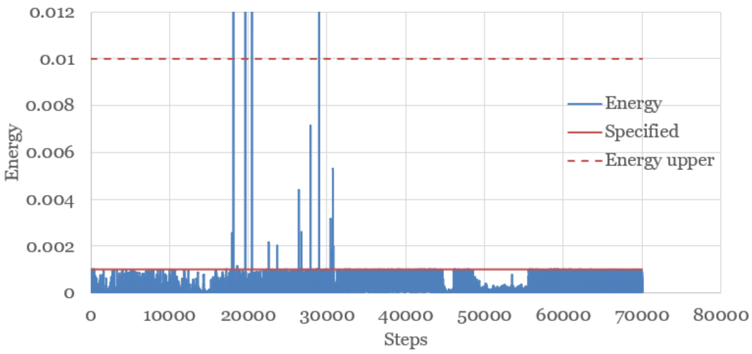

Figure B.13: Three sides restrained wall (EMM): Energy norm for long time signal.

B.3. Non-linear cyclic analysis

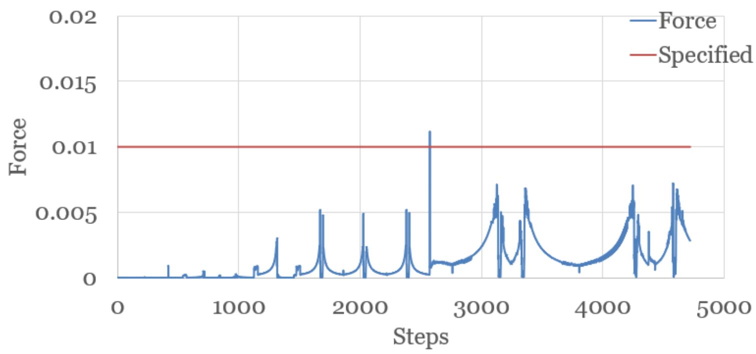

Figure B.14: Four sides restrained wall (localized): Force norm.

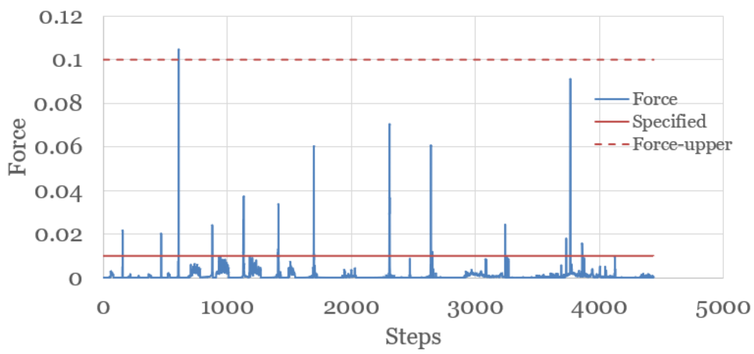

Figure B.15: Three sides restrained wall (EMM $G_f^I = 0.0295 N/mm$): Force norm.

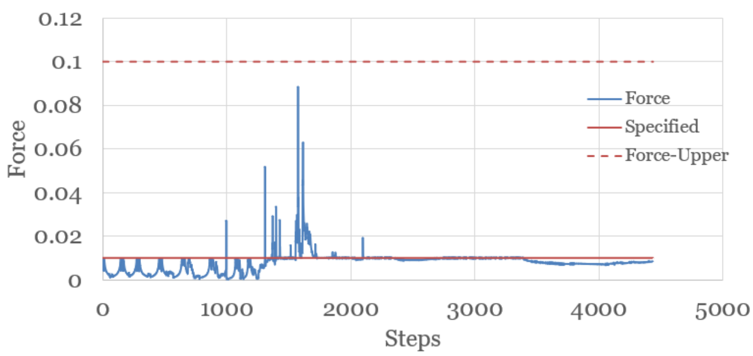

Figure B.16: Three sides restrained wall (TSRC $G_f^I = 0.0295 N/mm$): Force norm.

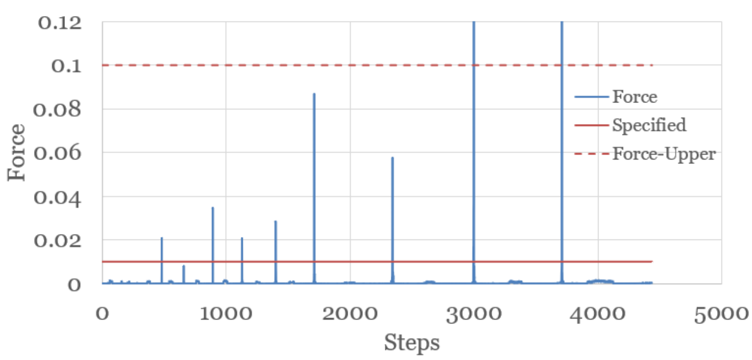

Figure B.17: Three sides restrained wall (EMM $G_f^I = 0.118 N/mm$): Force norm.

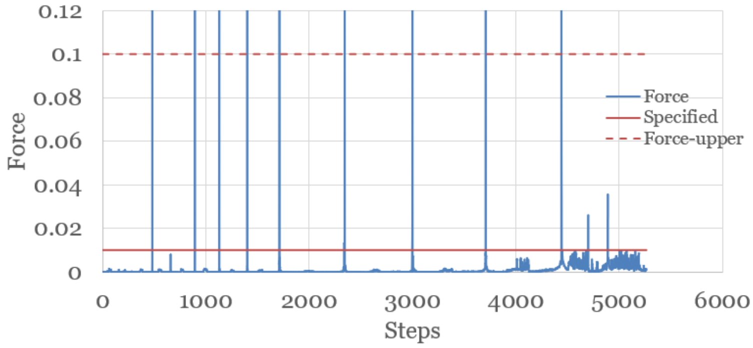

Figure B.18: Three sides restrained wall (EMM Set-2): Force norm.

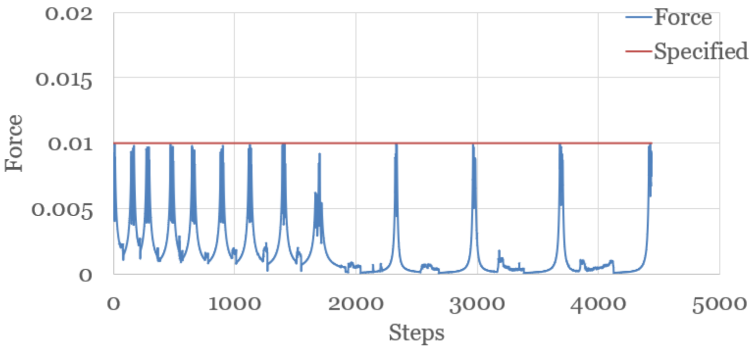

Figure B.19: Three sides restrained wall (TSRC $G_f^I = 0.118N/mm$): Force norm.